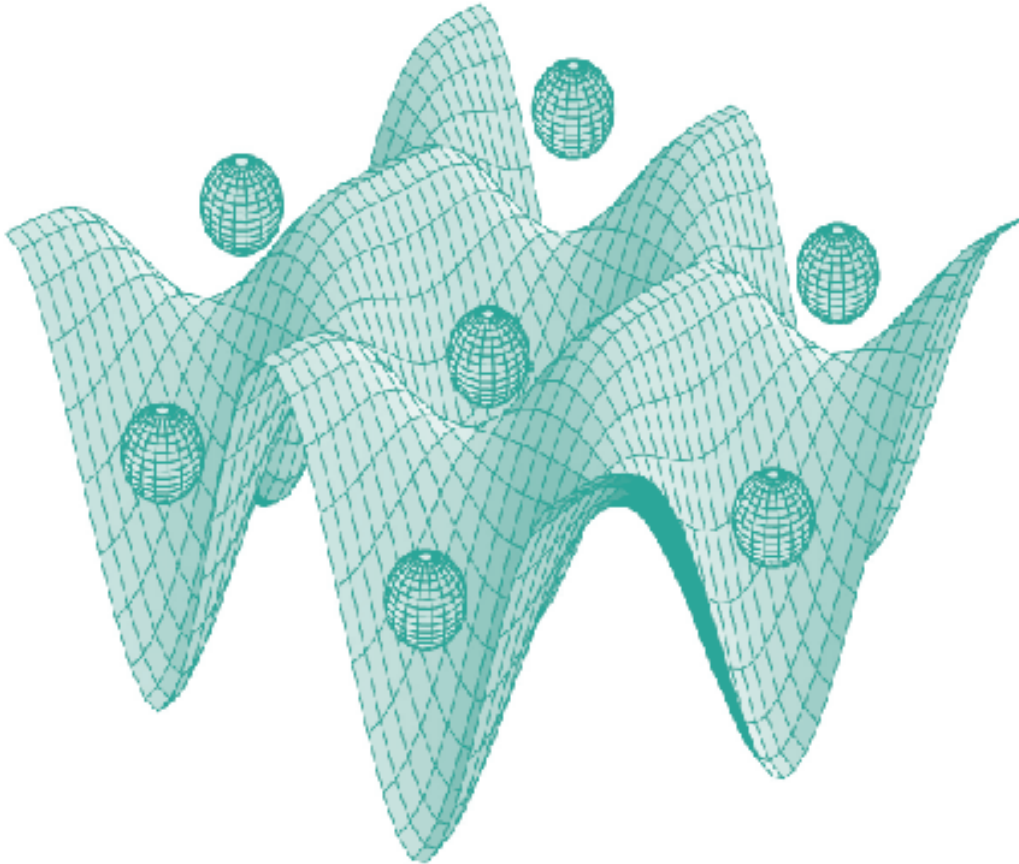




STUDIA UNIVERSITATIS
BABEȘ-BOLYAI



PHYSICA

2/2010

S T U D I A

UNIVERSITATIS BABEȘ-BOLYAI

PHYSICA

2

Desktop Editing Office: 51st B.P.Hasdeu Street, Cluj-Napoca, Romania, Phone +40 264 405352

SUMAR - SOMMAIRE - CONTENTS - INHALT

SZ. ZS. BENYEY, E. VANEA, C. GRUIAN, M. NEUMANN, V. SIMON, XPS Study of Protein Adsorption Onto Bioactive Glasses	3
C. CIPRIAN, L. DĂRĂBAN, Measurement of Thermal Neutron Cross-Section for $^{186}\text{W}(n,\gamma)^{187}\text{W}$ Nuclear Reaction by the Activation Method Using a Single Monitor ...	17
A. FALAMAS, C. DEHELEAN, N. LEOPOLD, C. LEHENE, V. CHIS, S. CINTA PINZARU, Anti-Tumoral Betulin Detection by Surface Enhanced Raman Scattering	25
A.M. GABUDEAN, D. BIRO, S. ASTILEAN, Synthesis and Characterization of Silica-Encapsulated Gold Nanorods	33
STEFAN PAUL GOSULY, LIVIU DĂRĂBAN, Resonance Integral and Thermal Cross-Section Measurements on Samarium Using AM-BE and PU-BE Isotopic Neutron Sources	41
C. GRUIAN, L. URBAN, H. BRUTLACH, L. V. PATMAVATHI, H.-J. STEINHOFF, S. SIMON, High-Field CW-EPR Study on Colicin-A Protein	55
ELENA HORJ, ANDREEA IORDACHE, MONICA CULEA, Method Validation for Free Amino Acids Determination in Biological Samples.....	61
V. IANCU, G. MELINTE, L. BAIA, L. BARBU-TUDORAN, C. COSMIN, V. DANCIU, V. COSOVEANU, M. BAIA, Synthesis and Morpho-Structural Analysis of TiO_2 -Au Composites	69
C. IONESCU, L. GHERGARI, V. SIMON, EPR Spectroscopy Applied to the Study of Ancient Ceramics: Preliminary Results for Bronze Age Pottery from Ilisua	79
JUNCAN ANCA MARIA, LUNG CLAUDIU, HORGA CRISTINA ELENA, Direct Determination of Natural and Synthetic Antioxidants in Cosmetic Creams by Gas Chromatography	85

ZSOLT I. LÁZÁR, Dynamics of Thermally Driven Spring-Block System on Inhomogeneous Surface	95
C. MOISESCU, D. PICIU, V. SIMON, Radiation Protection in Diagnosis and Treatment Procedures with ¹³¹ I.....	105
A.NEDELICU, V.CRISAN, Electronic Properties of Mnco System Alloys.....	111
R. STĂNESCU, N. VEDEANU, L. TIBRE, I. ARDELEAN, ESR and Raman Study of V ₂ O ₅ – P ₂ O ₅ – Bi ₂ O ₃ Glass System.....	115
LUCIANA UDRESCU, MIHAELA POP, VASILE BALC, M. TODICA, Observation of the Effects of UV Exposure of Some Samples Containing Tacrolimus	123
R. VERES, M. TĂMĂȘAN, C. CIUCE, V. SIMON, AFM Investigation of SiO ₂ -ZnO-P ₂ O ₅ thin Films	131

BOOK REVIEW

Roman Baican, Renewable energies, Grinta, Cluj-Napoca, 2010, ISBN 978-973-126-191-1 (MONICA BAIA)	139
---	-----

XPS STUDY OF PROTEIN ADSORPTION ONTO BIOACTIVE GLASSES

SZ. ZS. BENYEY¹, E. VANEA¹, C. GRUIAN¹, M. NEUMANN², V. SIMON¹

ABSTRACT. Adhesion of cells on the surface of scaffold biomaterials is the basic concept in tissue engineering that can be influenced by protein pre-adsorption. The serum albumin is one of the most concentrated proteins in the blood. This work reports X-ray photoelectron spectroscopy (XPS) results regarding the bovine serum albumin (BSA) attachment on three different sol-gel derived bioglass samples. The attachment degree of BSA depended on both bioglass composition and synthesis parameters.

Keywords: *bioglass; protein attachment; BSA; XPS.*

Introduction

Biomaterials have a great potential to mimic or replace living tissues, or even help create new tissues. Some biomaterials, including bioglasses can be used as scaffolds for tissue engineering. The use of scaffolds in tissue engineering is critical, because the majority of mammalian cells are anchorage dependent [1]. This means that these cells can't grow, migrate, proliferate without the supporting matrices and they die of. From these facts results the need for such scaffolds, which provide suitable surface for cell adhesion. Because the quality of scaffolds is determined by properties such as biocompatibility and biodegradability, they need to be highly porous with a large surface/volume ratio and to possess mechanical strength and dimensional stability. Bioglasses possess favourable properties for tissue engineering [2]. The biocompatibility is mainly determined by the surface interactions with blood and proteins [3], enhanced by the capacity of the material to adsorb proteins on its surface [4]. The large surface area and porous structure of the bioglasses synthesized by sol-gel method favours the adhesion and growth of large number of cells. This can be further improved by functionalizing the material with proteins from the extra cellular matrix [5]. One of the most concentrated proteins in the blood is the serum albumin, a transport and clearance protein that can bind to certain cell surfaces has a role in maintaining the osmotic balance [6], and is generally considered to "passivate" the surface of the materials thus reducing the acute inflammatory response [7]. To achieve cell adhesion and thus fulfilling the role of substrate for cell attachment growth and proliferation, the bioactive glass first needs to be functionalized, by attaching proteins to its surface.

¹ Babeş-Bolyai University, Faculty of Physics & Institute of Interdisciplinary Research in Bio-Nano-Sciences, Cluj-Napoca, Romania

² University of Osnabrück, Physics Department, Osnabrück, Germany

This functionalization improves cell adhesion, because usually cells don't attach directly to the culture substrate; rather they will bind to proteins that are absorbed to the scaffold's surface [8,9]. Surface analysis is needed to investigate the protein adsorption. In this study XPS was considered the most suitable method because chemical state analysis of the top 10 nm of the material is obtainable [10].

Experiment

For the preparation of the samples, tetraetoxisilan (TEOS), $\text{Ca}(\text{NO}_3)_2 \cdot 4\text{H}_2\text{O}$, $(\text{NH}_4)_2 \cdot \text{HPO}_4$ and Na_2CO_3 with high grade of purity were used as starting materials. NH_4OH and HCl were used for pH adjustment of the solution. First a solution of TEOS in ethanol with a few drops of HCl was mixed with water containing $\text{Ca}(\text{NO}_3)_2 \cdot 4\text{H}_2\text{O}$; $(\text{NH}_4)_2 \cdot \text{HPO}_4$ and Na_2CO_3 . To catalyze the reaction a few droplets of ammonia were added to the solutions. After continuous agitation for twenty minutes, in each case a gel is formed. Thus there were prepared three bioactive glasses with the calculated molar concentrations for the bioglass I and II being 0.55 SiO_2 0.41 CaO $0.04 \text{ P}_2\text{O}_5$ as for bioglass III 0.45 SiO_2 0.245 CaO $0.06 \text{ P}_2\text{O}_5$ $0.0245 \text{ Na}_2\text{O}$.

The bioglass I was aged for 70 days at room temperature after which a densification treatment was performed heating the glass to 310°C for one hour in air. The bioglass II was first dried at 80°C for 50 minutes after which the same aging and heat treatment were performed as on the previous one. The bioglass III was aged only for 30 days at room temperature, after which the same densification was performed as on the other two. For functionalizing purpose, the protein bovine serum albumin (BSA) was used. First a protein solution of 35 mg/ml concentration was created mimicking the concentration of albumin in the blood [11]. Following, small amount of the three bioglasses were put in small eppendorf containers and the protein solution was added so that it covered the glass completely. The containers were placed in incubator at a temperature of 37°C for up to four respectively eight hours, slowly shaken for a better mixing of the solution with the glass, and to avoid the deposition of the glass on the bottom of the containers. After the protein bath, the glasses were rinsed several times with deionised water, in order to retain only the irreversibly bound proteins on the glass surface. The unbound and the reversibly bound proteins were washed away by rinsing.

The samples were mounted on the sample holder using double sided carbon tape. Although the powders were pressed on the tape, which is conductive, because of the insulating properties of the glass further charge compensation was needed. This was achieved by using the low energy electron gun (neutralizer). The use of the neutralizer is not by far trivial, and due to some irregularities on the surface of the material it was not always possible to achieve full electron compensation. To further reduce the charging effect, the spectra were recorded using short scan times, so that the sample didn't have time to charge up. After the calibration of all peaks to the C1s at 284.6 eV, they were manually summed up to create a better resolution. The first requirement of the data fitting procedure (after shift-referencing has been performed) is removal of the background contribution. For this Shirley background was used [12].

The samples were analysed using XPS before and after protein adsorption. XPS measurements were performed using a PHI 5600ci Multi Technique system with monochromatized Al K_{α} radiation from a 250 W X-ray source ($h\nu = 1486.6$ eV) with pressure in the analysis chamber kept in the 10^{-9} Torr range.

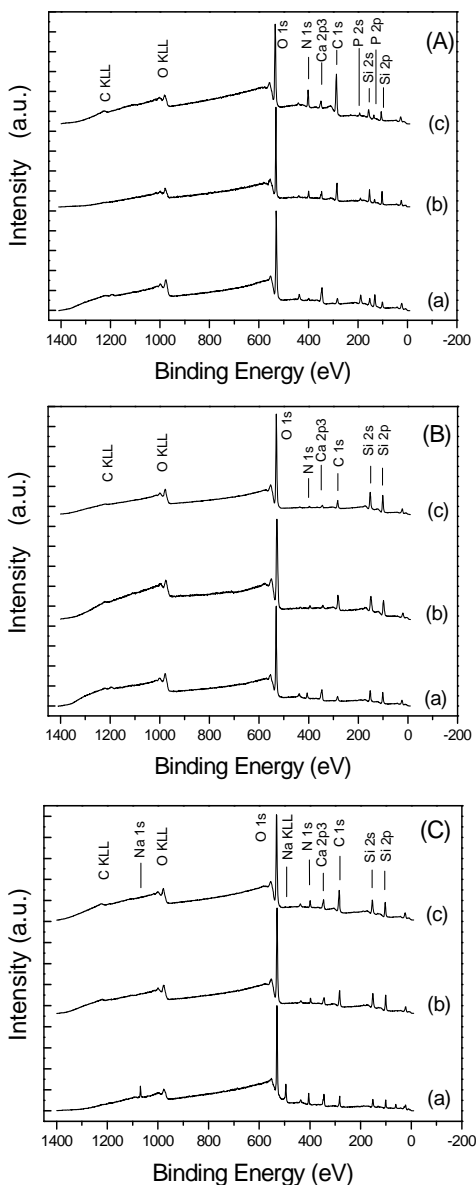


Figure 1. XPS survey spectra of the bioglasses before functionalization (a), after 4 hours (b) and respectively 8 hours (c) immersion in protein solutions, for bioglass I (A), bioglass II (B) and bioglass III (C).

The XPS survey spectra were recorded using a pass energy of $E_{\text{pass}} = 187.85$ eV, which allows registration of the XPS spectra in the whole energy range, from 1400 to -10 eV. Core level spectra of C 1s, N 1s, and O 1s were recorded using the value, $E_{\text{pass}} = 23.5$ eV.

Results and discussion

The chemical analysis by XPS evidences also that phosphorous is present on the surface of the bioglass I in a much higher content than expected according to system composition, and it is under the accuracy limit for the other two samples.

The XPS spectra show the presence of carbon in all samples before and after functionalization. The presence of carbon before functionalization is the result of carbon adsorption, which occurs on all surfaces exposed to the atmosphere [13]. The bioglasses presented here should have only traces of carbon from the Na_2CO_3 used as precursors, but no significant amount of carbon should be present in their composition. So, most of the carbon seen in the core level spectra of the untreated glass is due to contamination (Figure 2). Regardless of the carbon contamination, a change is still visible after the functionalization. Not only the intensity of the peaks increases, but their form changes as well, as a proof of protein attachment.

The relative atomic concentrations of the samples before and after the immersion are presented in Table 1. For all three bioglasses after the functionalization a significant increase in the intensity of the C 1s peak is observed, together with an increase of the N 1s peak. This is accompanied by the diminishing in strength of the other components specific to the glass, like silicon, calcium and oxygen. This is due to the irreversibly bound protein on the surface of the glass that covers its components.

As seen in the atomic concentration table (Table 1), the carbon concentration after the treatment with the protein solution increases significantly. But there are some differences in the behaviour of the three compounds. From the atomic concentrations it can be seen, that the bioglass I has the biggest adsorption rate from the three.

The carbon concentration in the bioglass I triple in four hours and will be increased almost six fold after eight hours. Together with this the increase of the nitrogen concentration with a significant amount is observable as well. The final proof for a very good protein fixation is the appearance of the sulphur peak after eight hours. The relative concentration of sulphur is just 0.7 %, while in the pure BSA sulphur must have values around 4%. Although it is in small concentration the sulphur peak can only come from the cysteine present in protein structure.

This affinity for the protein is most likely due to the fact that the first bioglass presents phosphor in a significant concentration, which makes it more biocompatible then the other two.

The adsorption of the proteins is also shown by the fact that the other peaks representing the elements of the bioglass become a bit smaller. This effect is small, because the BSA is not a large protein and so it can't hide the bioglass specific peaks completely, but also because the protein can't cover the whole surface of the

glass [14]. In Figure 1 the first spectral line (a) is representing the bioglass in its original state, so it contains all the elements composing the glass. The second and third spectral lines (b, c) are modified by the presence of the protein.

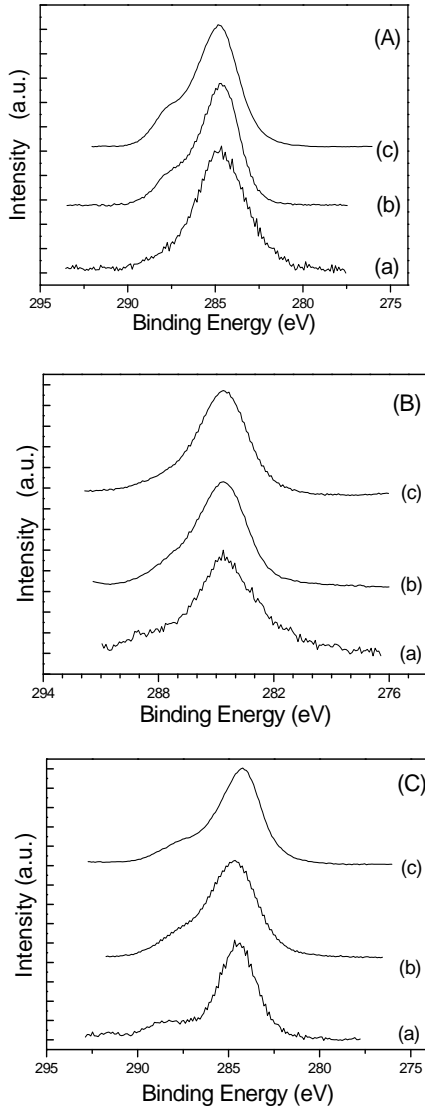


Figure 2. C 1s core level spectra before functionalization (a), after 4 hours (b) and respectively 8 hours (c) immersion in protein solutions for bioglass I (A), bioglass II (B), and bioglass III (C).

Table 1.

The relative atomic concentrations of the bioglasses before and after protein functionalization.

Material/time immersed	Elemental composition (at%)							
	C	O	N	Si	Ca	P	Na	S
Bioglass I								
0 min	7.8	55.2	1.2	11.4	6.2	18.2	-	-
4 h	26.3	45.0	4.7	19.0	2.3	2.7	-	-
8 h	42.7	31.9	9.2	10.0	1.8	3.8	-	0.6
Bioglass II								
0 min	9.7	58.5	3.8	23.0	5.0	-	-	-
4 h	21.2	48.8	2.0	27.4	0.6	-	-	-
8 h	13.6	52.6	1.4	31.6	0.9	-	-	-
Bioglass III								
0 min	16.3	52.8	8.4	14.1	4.5	-	3.8	-
4 h	24.0	45.8	4.1	23.6	2.6	-	-	-
8 h	28.6	43.3	4.7	20.6	2.9	-	-	-

Bioglass III has some interesting characteristics too. At first it contains a small amount of sodium, which disappears after the functionalization. This happens because the sodium ions are leaching from the glass surface in the water, when it is immersed. This shows that the glass is highly bioactive at first but loses this high bioactivity in a fairly short time, and becomes more inert. In fact, after 4 hours of immersion the sodium disappeared completely from the surface of the glass.

Both bioglass II and bioglass III show a lower adsorption rate than the first one. It can be observed that on bioglass II the adsorption rate is lower after 8 hours than after 4 hours. This can be associated with the reversibly bound proteins to the surface. If the bioglass has hydrophilic properties, it bounds the protein harder. This is because in water the protein tries to fold itself in such a manner that its hydrophilic part will face the water and the hydrophobic part will face away from it. If the bioglass is mainly hydrophilic then the protein will try to bind itself with its hydrophilic part to the glass, exposing the hydrophobic part to water. [14] This is energetically not a favourable position, so in time this bound can break. This is probably what caused the decrease in protein adsorption on the bioglass II. The carbon peaks will get broader after functionalization according to the bonds of carbon atoms in proteins. This can be pointed out by doing a deconvolution procedure on the core level lines.

To evidenciate the difference between the bioglass spectra before and after functionalization, deconvolutions were performed on the core level spectra recorded for bioglass I (Figure 3).

As seen from the deconvoluted spectra the C 1s main component is located around 284.6 eV. It was shown in literature [15,16] that it can be attributed to the C-C and C-H bounds. The components around 286 eV can be attributed to C-O bonds while the ones around 287.5 to the C=O. These two are carbon bounds present in proteins thus confirming the protein attachment. The photoemission of electrons will inevitably result in the formation of a positively charged surface on insulating materials

even with neutralization. This in turn reduces the kinetic energy of the photoelectron, leading to a shift of the observed spectrum to the lower binding energy scale, thus resulting in the components observed below 284.6 eV.

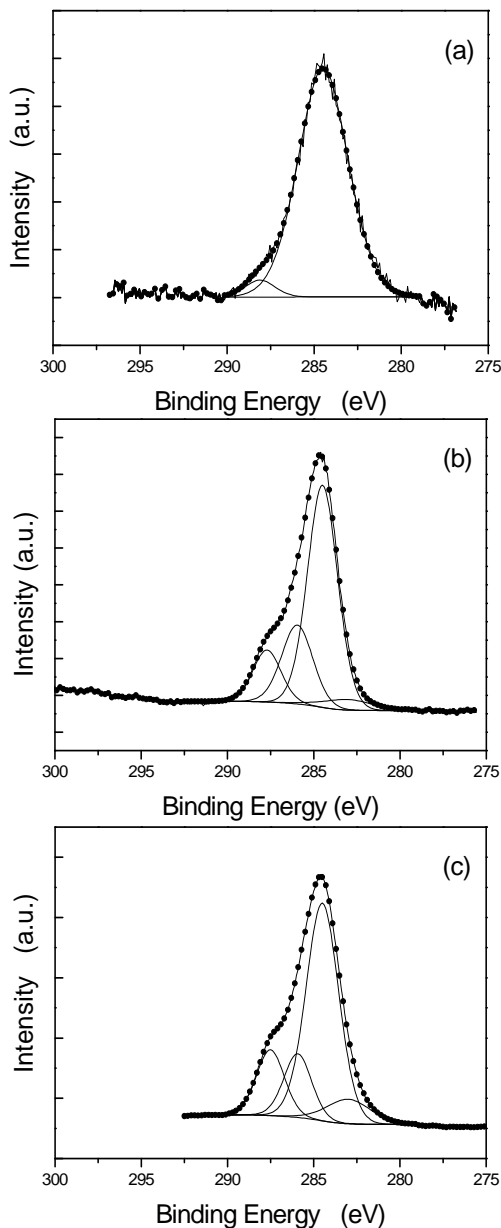


Figure 3. Deconvoluted C 1s core level spectra before functionalization (a), after 4 hours (b) and respectively 8 hours (c) immersion in the protein solutions for bioglass I.

If the samples do not contain nitrogen in their composition, the nitrogen can be used as the main marker for protein adsorption [8]. But in the investigated sol-gel derived glasses, nitrogen already exists in the due to the preparation procedures. As in the case of C 1s, a change is visible in the N 1s peaks too, but mostly in intensity. The N 1s core level spectra are presented in Figure 4.

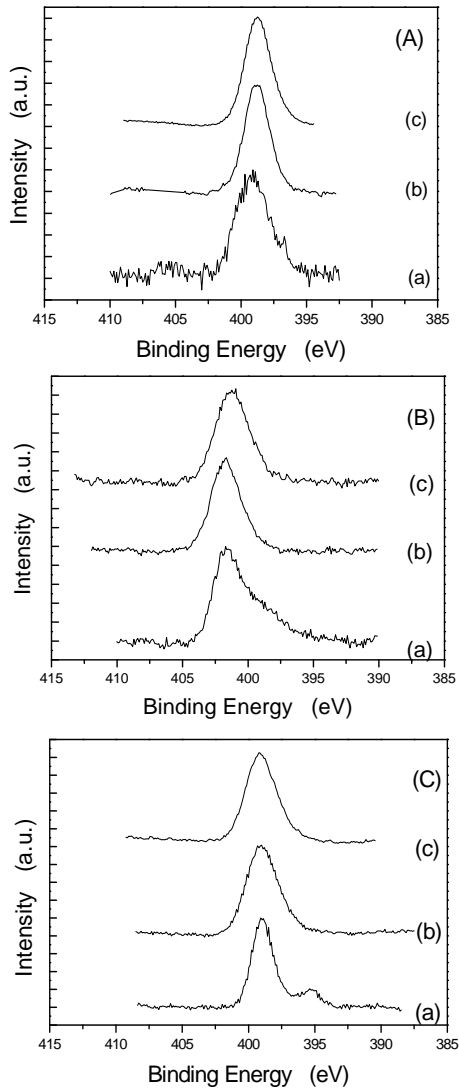


Figure 4. N 1s core level spectra before functionalization (a), after 4 hours (b) and respectively 8 hours (c) immersion in protein solutions for bioglass I (A), bioglass II (B), and bioglass III (C).

The deconvolution performed on the N 1s peaks were also made on the bioglass I (Figure 5). As stated in [15,16,17] references, the nitrogen peaks are symmetric, around 400 eV and are typical for the C – N bounds specific to peptide nitrogen found in proteins.

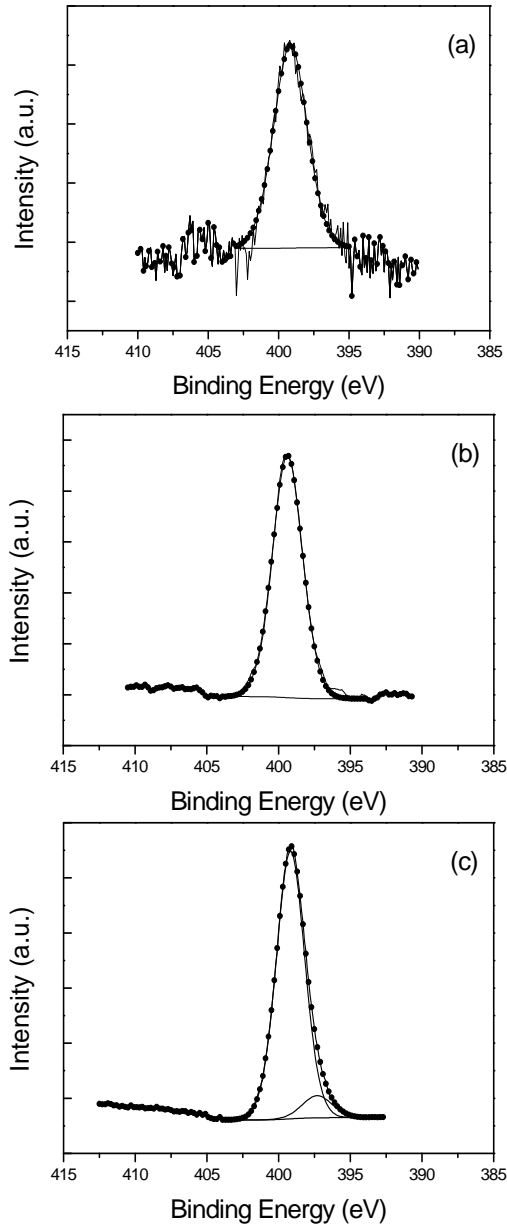


Figure 5. Deconvoluted N 1s core level spectra before functionalization (a), after 4 hours (b) and respectively 8 hours (c) immersion in protein solutions for bioglass I (A), bioglass II (B), and bioglass III (C).

Examining the core level spectra of the oxygen (Figure 6), it shows a decrease in intensity. This is because the glass is mainly composed from oxides, but the albumin only contains about 18% in molar concentration. So if the albumin covers the glass the concentration of the oxygen becomes smaller.

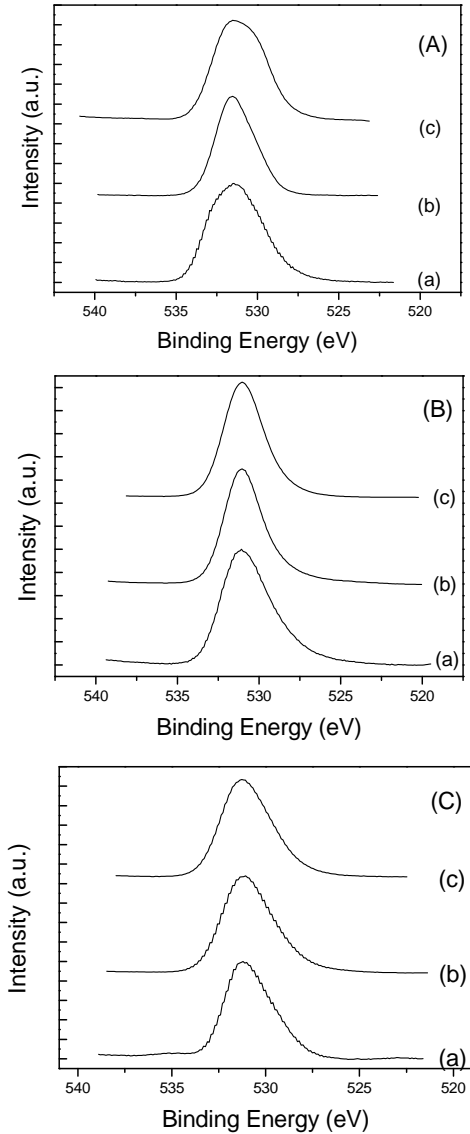


Figure 6. O 1s core level spectra before functionalization (a), after 4 hours (b) and respectively 8 hours immersion in protein solutions for bioglass I (A), bioglass II (B), and bioglass III (C).

If the deconvolutions made on the bioglass I core level spectra are examined, the O 1s peaks before and after the immersion show that the main peaks shift slightly to higher binding energies. This can be attributed to a slight deficiency in electron density around the oxygen atoms in the functionalized state [15].

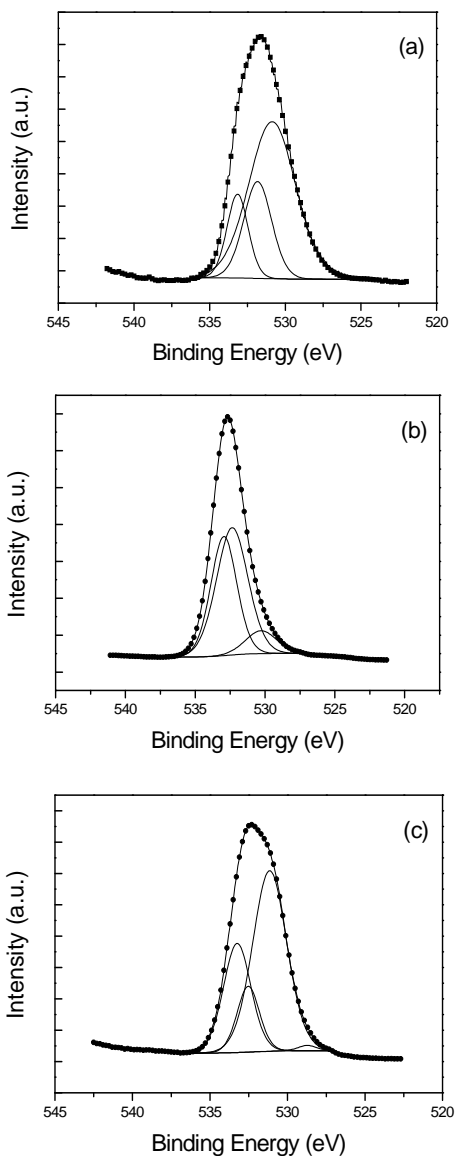


Figure 7. Deconvoluted O 1s core level spectra before functionalization (a), after 4 hours (b) and respectively 8 hours immersion in protein solutions (c) for bioglass I.

Conclusions

XPS investigations yield evidence of BSA adsorption on bioglasses surface after incubation in BSA solutions.

On the glass I, for which higher phosphorus content was recorded by XPS, the carbon concentration triples in 4 hours and will be almost six times bigger after 8 hours. It was also observed a significant increase of the nitrogen concentration as a result of peptide nitrogen. After 8 hours of immersion this glass shows traces of sulphur which is also present in small amounts in BSA.

This study shows that not only the composition of the sol-gel derived bioglasses, but also the aging conditions/parameters can influence the protein adhesion.

The phosphorus on the surface of the bioglass can positively influence the quick attachment of BSA protein. This affinity of the bioglass for the protein makes it an ideal candidate for further studies.

REFERENCES

1. K. Gilson, K. Moon Suk & L. Hai Bang. *A manual for biomaterials/Scaffold fabrication technology*. World Scientific, 2007.
2. L.L. Hench, J.R. Jones & P. Sepulveda. In *Future strategies for tissue and organ replacement*. Ed. J.M. Polak. World Scientific, 2002.
3. K. Vijayanand, D.K. Pattanayak, T.R. Rama Mohan & R. Banerjee. Interpreting blood-biomaterial interactions from surface free energy and work of adhesion. *Trends Biomater. Artif. Organs*, **18**, 73 (2005).
4. F. Rossi, A. Valsesia, M. Manso, G. Ceccone & P. Colpo. Micro- and nano-structured thin films for Biological Interfaces. *Nato Sci. Ser II Math. Phys. Chem.*, **155**, 285 (2004).
5. P.X. Ma, Biomimetic materials for tissue engineering. *Adv. Drug. Deliver Rev.*, **60**, 184 (2008).
6. P. Tengvall. In *Role of implant surface properties on the clinical outcome of osseointegrated oral implant therapy*. Eds. M. Esposito, H. V. Worthington, P. Coulthard, A. Wennerberg & P. Thomsen. CRC Press LLC, 2003.
7. L. Tang & J.W. Eaton. Inflammatory responses to biomaterials. *Am. J. Clin. Pathol.*, **103**, 466 (1995).
8. Q.-Z. Chen, K. Rezwan, V. Françon, D. Armitage, S.N. Nazhat, F.H. Jones & A.R. Boccaccini. Surface functionalization of Bioglass®-derived porous scaffolds. *Acta Biomater.*, **3**, 55 (2007).
9. Q.-Z. Chen, K. Rezwan, D. Armitage, S.N. Nazhat & A.R. Boccaccini. The surface functionalization of 45S5 Bioglass®-based glass-ceramic scaffolds and its impact on bioactivity. *J. Mater. Sci. Mater. Med.*, **17**, 979 (2006).
10. A. Rossi, B. Elsener & N.D. Spencer. XPS surface analysis: imaging and spectroscopy of metal and polymer surfaces. *Spectroscopy Europe*, **6**, 14 (2004).
11. L.F. Stee, M.G. Trotter, P.B. Nakajima, T.S. Mattu, G. Gonye & T. Block. Efficient and specific removal of albumin from human serum samples. *Mol. Cell Proteomics*, **2**, 262 (2003).
12. D. Holland & M.E. Smith. In *Handbook of Sol-Gel Science and Technology Processing, Characterization and Applications: Characterization and Properties of Sol-Gel Materials and Products*. Ed. A.M. Rui. Kluwer Academic Publishers, 2004.
13. V. Simon, S. Cavalu, S. Simon, H. Mocuta, E. Vanea, M. Prinz & M. Neumann. Surface functionalisation of sol-gel derived aluminosilicates in simulated body fluids. *Solid State Ionics*, **180**, 764 (2009).

XPS STUDY OF PROTEIN ADSORPTION ONTO BIOACTIVE GLASSES

14. R.A. Latour. In *Encyclopedia of biomaterials and biomedical engineering*. Eds. G.L. Bowlin & G. Wnek. Informa Healthcare, 2005.
15. V. Simon, S. Simon, E. Vanea, M. Prinz & M. Neumann. Synthesis and surface characterization of biomaterials functionalized in protein enriched simulated body fluids. *Studia Univ. Babeş-Bolyai, Physica*, **53**, 25 (2008).
16. I. Frateur, J. Lecoeur, S. Zanna, C. Olsson, D. Landolt & P. Marcus. Adsorption of BSA on passivated chromium studied by a flow-cell EQCM and XPS. *Electrochim. Acta*, **52**, 7660 (2007).
17. Y.F. Dufrêne, T.G. Marchal & P.G. Rouxhet. Probing the organization of adsorbed protein layers: complementarity of atomic force microscopy, X-ray photoelectron spectroscopy and radiolabeling. *Appl. Surf. Sci.*, **144-145**, 638 (1999).

MEASUREMENT OF THERMAL NEUTRON CROSS-SECTION FOR $^{186}\text{W}(n,\gamma)^{187}\text{W}$ NUCLEAR REACTION BY THE ACTIVATION METHOD USING A SINGLE MONITOR

C. CIPRIAN¹, L. DĂRĂBAN

ABSTRACT. We measured the thermal neutron cross-section for the nuclear reaction $^{186}\text{W}(n,\gamma)^{187}\text{W}$ by the activation method using a $^{197}\text{Au}(n,\gamma)^{198}\text{Au}$ monitor reaction as single comparator. The high-purity natural W and Au metallic foils with or without a cadmium shield case of 1 mm thickness were irradiated in a neutron field at the Faculty of Physics neutron facility in Cluj-Napoca, Romania. The induced activities in the samples were measured by high-resolution γ -ray spectrometer with a calibrated HPGe detector. The necessary correction factors for γ -ray attenuation (F_{γ}), thermal neutron self-shielding factor (G_{th}), were taken into account. The thermal neutron cross-section for the $^{186}\text{W}(n,\gamma)^{187}\text{W}$ nuclear reaction has been determined to be 38.69 barns, relative to the reference value of 98.65 ± 0.09 barns for the $^{197}\text{Au}(n,\gamma)^{198}\text{Au}$ nuclear reaction. The present result is, in general, in good agreement with most of the experimental data and the recently evaluated value of ENDF/B-VII.0 and JENDL-3.2, data basis.

Keywords: Thermal neutron cross-section; $^{186}\text{W}(n,\gamma)^{187}\text{W}$; $^{197}\text{Au}(n,\gamma)^{198}\text{Au}$; Neutron Activation Method; Cross section at resonance;

1. INTRODUCTION

Tungsten (W) is one of the structural materials for the fusion reactor because it can endure high temperatures. It is also often used as the target material of the electron accelerator for producing bremsstrahlung and neutrons. The knowledge of the thermal neutron cross-section for $^{186}\text{W}(n,\gamma)^{187}\text{W}$ nuclear reaction has become important in the calculations of decay heat and evaluating the radiation damage of the material.

We have found in literature a number of experimental and evaluated data on the thermal neutron capture cross-section for the $^{186}\text{W}(n,\gamma)^{187}\text{W}$ nuclear reaction. However, most of the reported experimental data have been measured during the time period from years 1990, and there is only three measurements carried out recently,[1-3]. The measured thermal neutron capture cross-section for the $^{186}\text{W}(n,\gamma)^{187}\text{W}$ reaction varied from 33 barn to 42.8 barn. This fact shows that, there are still large discrepancies among the experimental data for $^{186}\text{W}(n,\gamma)^{187}\text{W}$ reaction. Therefore, it is necessary to measure more data of the $^{186}\text{W}(n,\gamma)^{187}\text{W}$ reaction for better comparison. Usually, the

¹ Babes-Bolyai University, Faculty of Physics, Str. Kogalniceanu, Nr. 1, RO-400084 Cluj-Napoca, Romania, admiral_ciprian@yahoo.com

thermal neutron capture cross-section for the $^{186}\text{W}(n,\gamma)^{187}\text{W}$ reaction were measured by the well known activation method by using two monitor reactions: $^{55}\text{Mn}(n,\gamma)^{56}\text{Mn}$ and/or $^{197}\text{Au}(n,\gamma)^{198}\text{Au}$. The advantages and limitations of each monitor reaction were described by [4,5]. We measured the thermal neutron capture cross-section and the resonance integral of the $^{186}\text{W}(n,\gamma)^{187}\text{W}$ by the activation method at the Faculty of Physics in Cluj-Napoca neutron facility based on two isotopic neutron sources: having a 4.8 Ci $^{241}\text{Am}-^9\text{Be}$ and 33 Ci $^{239}\text{Pu}-^9\text{Be}$. The results were determined relative to the reference values of $\sigma_{0,\text{Au}} = 98.65 \pm 0.09$ barn for the $^{197}\text{Au}(n,\gamma)^{198}\text{Au}$ monitor reaction. In order to improve the accuracy of the experimental results, the correction factors for γ -ray attenuation (F_g), thermal neutron self-shielding (G_{th}), were taken into account. The present result were compared with the experimental data.

2. EXPERIMENTAL SETUP

2.1 Neutron source

The neutrons used in this experiment were generated using two neutron sources, immersed in the center of a cylindrical paraffin moderator 60x60 cm. The geometrical configuration of the neutron sources have 3 irradiation channels at 3.5 cm distance from the axis of the neutron irradiation unit facility. The thermal neutron flux at the sample irradiation position of the $^{241}\text{Am}-^9\text{Be}$ and $^{239}\text{Pu}-^9\text{Be}$ neutron irradiation block has been measured to be $\Phi = (1.64 \pm 0.30) \cdot 10^5 \text{ n/s}$.

2.2 Sample irradiation

A foil of tungsten (14x17 mm, 1mm thick; of natural composition) and thin gold foils (14x17 mm, 1mm thick; purity 99.99%) were irradiated with neutrons of 0.025 eV energy for 175.53 h without cadmium cover, and 190.41 h with cadmium cover. Gold foils were used to measure the effective neutron flux using the $^{197}\text{Au}(n,\gamma)^{198}\text{Au}$ monitor reaction. Two gold foils of the same size and weight were attached at the front and back of the tungsten foil, respectively to check the difference in neutron beam intensity between entrance and exit of the target. To follow the effect of epithermal neutrons and fast neutrons, the cadmium-covered gold foils were also irradiated.

2.3 Gamma-ray measurement and data analysis

The activities of the radioisotopes produced in the target and the monitor foils were measured nondestructively using high-purity germanium (HPGe) gamma-ray spectroscopy (Canberra, 15% relative efficiency, 1.8 keV resolution at 1332.5 keV of ^{60}Co) coupled with a digital gamma spectrometry system (MCA Canberra) and Genie 2000 data acquisition software. Measurements were started immediately after the end

of irradiation. The thickness of the material used in the present experiment was limited for the self-absorption of captured gamma rays in the sample. If the absorption becomes large, the fraction of the gamma rays “escaping” may become a function of the neutron capture cross section of the sample. This arises from the fact that a capture event occurring near the front face (which is more likely when the cross section is relatively high) can have an appreciably higher probability of being detected than one that originates in the interior due to the exponential nature of the gamma attenuation. The efficiency versus curve of the HPGe gamma-ray detector for the counting distance was determined using standard point sources, ^{241}Am , ^{22}Na , ^{60}Co , ^{137}Cs . The neutron beam intensity was determined from the activities induced in gold monitor foils using the $^{197}\text{Au}(n,\gamma)^{198}\text{Au}$ monitor reaction. The monitor foils were irradiated simultaneously and measured with the same detector and in a comparable geometry with the tungsten target.

3. RESULTS AND DISCUSSIONS

The natural W consists of ^{180}W (0.12%), ^{182}W (26.49%), ^{183}W (14.314%), ^{184}W (30.642%), ^{186}W (28.42%). It is evident that the $^{186}\text{W}(n,\gamma)^{187}\text{W}$ nuclear reaction is interference free when the purity of W foil is activated by thermalized neutron. From a typical gamma spectrum of the activated W foil in Fig.1, we can easily recognize that there is no interference in the gamma activity measurements for the $^{186}\text{W}(n,\gamma)^{187}\text{W}$ reaction. The ^{187}W activity was determined by using the 685 keV gamma peak.

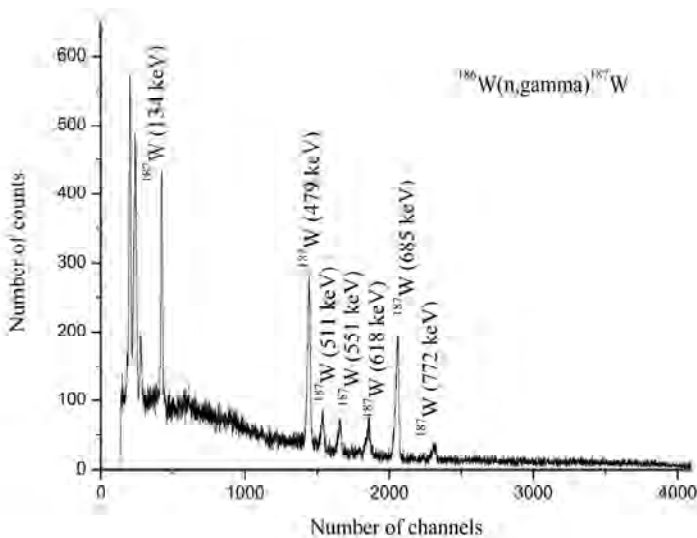


Fig. 1. The $^{186}\text{W}(n,\gamma)^{187}\text{W}$ gamma spectrum measured for 120 min

3.1 Data analysis

The thermal neutron cross-section was determined from the reaction rates in the analysis of measured spectral data from the induced activities. The thermal neutron cross-section for the reaction $^{186}\text{W}(n,\gamma)^{187}\text{W}$ has been determined relative to that for the $^{197}\text{Au}(n,\gamma)^{198}\text{Au}$ standard reaction. The thermal neutron cross-section, $\sigma_{0,W}$ for the $^{186}\text{W}(n,\gamma)^{187}\text{W}$ reaction, is calculated as follows [1,2,5-13]:

$$\sigma_{0,W} = \sigma_{0,Au} \times \frac{R_W - F_{W,Cd} \cdot R_{W,Cd}}{R_{Au} - F_{Au,Cd} \cdot R_{Au,Cd}} \times \frac{G_{th,Au}}{G_{th,W}} \times \frac{g_{Au}}{g_W} \quad (1)$$

where $\sigma_{0,Au}$ is the thermal neutron cross-section of the $^{197}\text{Au}(n,\gamma)^{198}\text{Au}$ reaction, $R_{W(Au)}$ and $R_{W(Au),Cd}$ are reaction rates per atom for bare and Cd-covered W and Au isotope irradiation, respectively. The $F_{W(Au),Cd}$ is the cadmium correction factor, and $G_{th,W(Au)}$ is the thermal neutron self-shielding factor for the W(or Au) samples, the thermal neutron self-shielding factor was calculated for both foils and it was close to 1 (negligible). The $g_{W(Au)}$, Wescott correction factor, correction for departure from $1/v$ cross-section behavior, for the $^{186}\text{W}(n,\gamma)^{187}\text{W}$ reaction and that for the $^{197}\text{Au}(n,\gamma)^{198}\text{Au}$ reaction is 1.000. After a bare and Cd-covered sample irradiations, the reaction rates $R_{W(Au)}$ for W and Au samples are determined by M.S. Uddin et. al. formula [3]:

$$R = \frac{\lambda \cdot C}{N \cdot \varepsilon \cdot I_\gamma \cdot e^{-\lambda t_c} \cdot (1 - e^{-\lambda t_m}) \times (1 - e^{-\lambda t_i})} \quad (2)$$

where λ is the decay constant, (s^{-1}); C is the total counts of gamma-ray peak area; N is the number of target nuclei; ε is the peak efficiency; I_γ is the branching ratio of gamma ray; t_c is the cooling time, (s); t_m is the counting time, (s); t_i is the irradiation time, (s).

3.2 Correction factors

In order to improve the accuracy of the experimental results, the following correction factors such as the neutron self-shielding and g-factors were considered. The thermal neutron self-shielding factor for thin slabs was calculated as follows [1,2]:

$$G_{th} = \frac{(1 - e^{-\xi})}{\xi}, \quad (3)$$

where $\xi = 2 / \sqrt{\pi} \Sigma_0 t$, Σ_0 is the macroscopic capture cross-section for thermal neutrons ($E_n=0.0025\text{eV}$), and t is the foil thickness.

3.3 The thermal neutron cross-section for $^{186}\text{W}(n,\gamma)^{187}\text{W}$ reaction

The present result for the thermal neutron cross-section of the $^{186}\text{W}(n,\gamma)^{187}\text{W}$ reaction is 38.6 ± 3.0 barns and is compared with the literature data in Table 1. As seen in the Table 1, done by [2], the experimental and the evaluated values for the thermal neutron cross-section of the $^{186}\text{W}(n,\gamma)^{187}\text{W}$ reaction are varied from 33 barns to 42.8 barns. The present result of 38.6 barns is in good agreement with the values obtained by De Corte [14-18], Karadag [1].

In addition the evaluated thermal neutron cross-section values for the $^{186}\text{W}(n,\gamma)^{187}\text{W}$ reaction, 37.5 barns of ENDF/B-VII.0 [18], 39.45 barns of JENDL-3.3 [19], 38.27 barns of BROND-2 [20] data basis are close to the result in this work.

Table 1.

Thermal neutron cross-section for $^{186}\text{W}(n,\gamma)^{187}\text{W}$ reaction

Year	Authors	$\sigma_{0,W}$ (barns)	Monitor Used
2010	In present paper	38.6	Au
2007	Nguyen Van Do	37.2 ± 2.1	Au
2006	ENDF/B-VII.0	37.5	-
2004	Karadag	39.5 ± 2.3	Mn
2003	De Corte	41.8 ± 2.9	Au
2002	JENDL-3.3	39.45	-
1998	Holden	37 ± 2	-
1997	Kafala	42.8 ± 0.8	Au
1994	BROND-2	38.27	
1989	De Corte	38.7 ± 1.9	Au
1987	Gryntakis	37 ± 1.5	-
1987	Knopf	38.5 ± 0.8	Au
1984	Mughabghab	37.9 ± 0.6	Au
1984	Simonits	37.0 ± 1.8	Au
1981	Anufriev	37 ± 3	Absolute measured
1978	Heft	36.6 ± 0.8	Au, Sc, Co, U
1977	Gleason	37.0 ± 1.5	Au
1976	Erdtmann	37.8 ± 1.5	Au
1972	De Soete	36	-

Year	Authors	$\sigma_{0,W}$ (barns)	Monitor Used
1970	Hogg	40.0 ± 1.5	Co
1967	Damle	35.4 ± 0.8	Au
1966	Gillette	33	-
1966	Friesenhahn	37.8 ± 1.2	W, Au
1960	Lyon	41.3	Co
1952	Pomerance	34.1 ± 2.7	Au
1947	Seren	34.2 ± 6.8	Au

4. CONCLUSIONS

The neutron capture cross section for the $^{186}\text{W}(n,\gamma)^{187}\text{W}$ reaction relative to the $^{197}\text{Au}(n,\gamma)^{198}\text{Au}$ monitor reaction was measured at 0.025 eV neutron energy by activation technique using two superposed isotopic neutron sources: ^{241}Am - ^9Be and ^{239}Pu - ^9Be , at Faculty of Physics, University Babeş-Bolyai, in Cluj-Napoca. We report new cross-section amounts to 38.6 barns, which is consistent with the data of De Corte [14-17], Brond-2 [20]. The obtained value will be useful for the proper estimation of radioactivity and radiation safety analysis in fusion reactors.

REFERENCES

1. Mustafa Karadag, Haluk Yücel, , Ann. Nucl. Energy, vol. 31, pp.1285-1297, 2004.
2. Nguyen Van Do, Pham Duc Khue, Kim Tien Thanh, Le Truong Son, Guinyun Kim, Young Seok Lee, Youngdo Oh, Hee-Seok Lee, Moo-Hyun Cho, In Soo Ko, Won Namkung, Nucl. Instr. and Meth B, vol. 266, pp.863-871, 2008.
3. M.S. Uddin, M.H. Chowdhury, S.M. Hossain, Sk. A. Latif, M.A. Hafiz, M.A. Islam, A.K.M. Zakaria, S.M. Azharul Islam, Appl. Radiat. Isot., vol. 66, pp. 1235-1239, 2008.
4. M. Karadag, H. Yücel, M. Tan, A. Özmen, Nucl. Instr. And Meth. A 501 (2003) pp. 524-535.
5. H. Yücel, M. Karadag, Ann. Nucl. Energy, 32, (2005), 1.
6. M.G. Budak, H. Yücel, M. Karadag, M. Tan, Ann. of Nucl. Energy, vol 35, issue 8, pp.1433-1439, 2008.
7. Haluk Yücel, M. Güray Budak and Mustafa Karadag, Physical Review C, vol.76, no.3, 034610, 2007.
8. A.I. Egorov, Yu. E. Loginov, S. Eh. Malyutenkova, Appl. Radiat. Isot., vol. 65, pp. 1290-1292, 2007.

9. Marie-Christine Lépy, Marie-Noëlle Amiot, Marie-Martine Bé, Philippe Cassette, *Appl. Radiat. Isot.*, vol. 64, pp. 1428–1434, 2006.
10. Hiroshi Miyahara, Yoshimune Ogata, Kazuo Fujiki, Keiji Katoh, Nada Marnada, *Appl. Radiat. Isot.*, vol. 60, pp. 295-299, 2004.
11. T. Hayakawa, T. Shizuma, T. Yamauchi, E. Minehara and T. Arisawa, *Nucl Physics A*, vol. 718, pp. 665c-667c, 2003.
12. T.F. Wang, A.K.M.M.H. Meaze, M.U. Khandaker, M.S. Rahman, G.N. Kim, L.P. Zhu, H.H. Xia, Z.Y. Zhou, Y.D. Oh, H. Kang, M.H. Cho, I.S. Ko, W. Namkung, *Nucl. Instr. and Meth B*, vol. 266, pp. 561-569, 2008.
13. N. Habib , *Ann. Nucl. Energy*, vol. 31, pp. 697–709, 2004.
14. F. De Decorte, K. Sordo-El Hammami, L. Moens, A. Simonits, A. De Wispelaere, J. Hoste, *J. Radioanal. Nucl. Chem*, vol. 62, No. 1-2, pp. 209-255, 1981.
15. L.Moens, F.De Corte, A. Simonits, A. De Wispelaere, J. Hoste, *J. Radioanal. Nucl. Chem*, vol.52, No. 2, pp. 379-387, 1979.
16. R. Van der Linden, F. De Corte, J.Hoste, *J. Radioanal. Nucl. Chem.*, vol. 20, pp. 695-706, 1974.
17. F. De Corte, A. Simonits, A. De Wispelaere, *J. Radioanal. Nucl. Chem.*, Articles, vol. 133, No. 1, pp. 131-151, 1989.
18. <http://www.nndc.bnl.gov/exfor/endl00.jsp>
19. <http://www.ndc.jaea.go.jp/jendl/j32/j32.html>
20. <http://www-nds.iaea.org/ndspub/download-endl/BROND-2-2/>

ANTI-TUMORAL BETULIN DETECTION BY SURFACE ENHANCED RAMAN SCATTERING

A. FALAMAS¹, C. DEHELEAN², N. LEOPOLD¹, C. LEHENE¹, V. CHIS¹, S. CINTA PINZARU^{1,*}

ABSTRACT. Betulin, a lupan skeleton compound isolated from the outer bark of the birch tree has been recently topical formulated as antitumor compound effective in melanoma treatment. Aiming to monitor the pharmaceutical damaged skin therapy using SERS, we report here new results on betulin adsorption availability using surface enhanced Raman scattering (SERS). The SERS spectra of betulin dissolved in DMSO aqueous solution have been recorded and discussed in order to further detect the active compound in several new semisolid pharmaceutical formulations. On the basis of our earlier spectroscopic results in conjunction with DFT calculation, SERS spectra have been completely assigned and compared to those of betulinic acid previously reported. A chemisorption process was concluded, based on the dramatic change in the bands position and relative intensity. The CH₂OH functional group was found to be involved in adsorption.

Key words: betulin, SERS, Raman, pentacyclic triterpene.

INTRODUCTION

Betulin (lup-20(29)-ene-3 β ,28-diol) is a triterpene compound obtained from the white outer bark of the birch tree by sublimation or extraction using organic solvents [1]. Betulin (also known as betulinol, betuline or betulinic alcohol), a pentacyclic triterpene alcohol with a lupane skeleton (Fig. 1), has recently attracted an enormous interest due to its antitumoral activity. Together with other compounds found in the bark, such as betulinic acid or lupeol, it presents important anti-inflammatory and anti-cancerous properties [2-6]. Betulin and betulinic acid were found to show cytotoxic activity towards a number of cancer cell lines as well [7].

One major problem of these types of triterpenes is their low solubility, being practically insoluble in aqueous media. This compound can be hardly dissolved in only a few solvents, such as ethanol or dimethyl sulphoxide. Our very recent results showed that cyclodextrin encapsulation leads to an increased solubility within a guest-host complex formulation [8]. For this experiment, DMSO was employed

¹ Babes Bolyai University, Dept. of Physics, Kogalniceanu 1, RO 400084, Cluj-Napoca, România

² Victor Babeş University of Medicine and Pharmacy, Faculty of Pharmacy, Eftimie Murgu Square 2, RO- 300041, Timișoara, România

* E-mail: simona.cinta@phys.ubbcluj.ro

since this solvent can be used in medical applications. DMSO has been previously used in medicine and it was found that it could penetrate the skin and other membranes without damaging them and could carry other compounds into a biological system. This fact is of particular importance for this study since this betulin-DMSO solution could be later used in biomedical applications such as skin treatments.

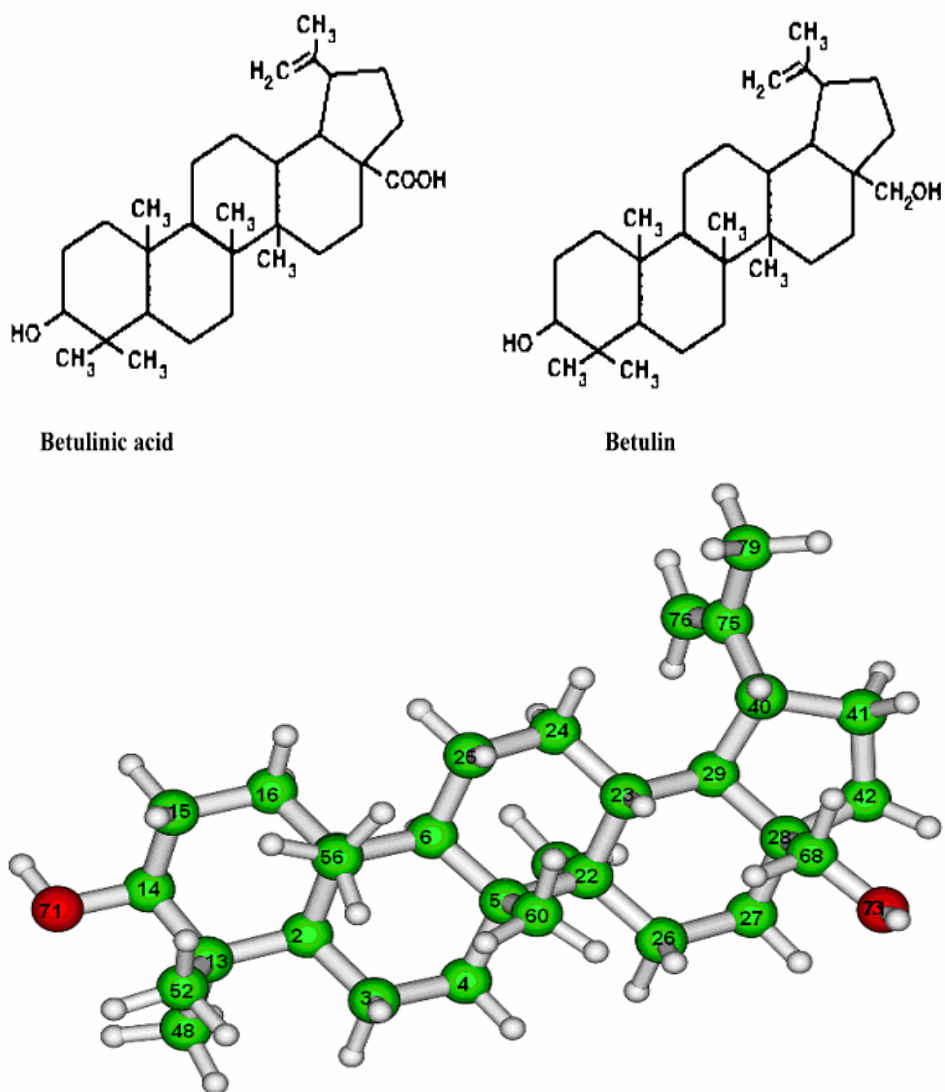


Fig. 1. Molecular structure of betulinic acid and betulin (up) and the optimized geometry of betulin resulted from the DFT calculations using the B3LYP/6-31 G(d) level of theory

MATERIALS AND METHODS

Sample Preparation

Betulin was purchased from Extrasynthese (France) as a white crystalline powder of analytical purity. The Ag sol used for the SERS experiments on betulin was prepared according to the method proposed by Leopold and Lendl [9].

Both betulin and betulinic acid are very difficult to be dissolved for spectroscopic experiments. For the SERS spectra of betulin, 50 ml of aqueous solution were prepared in the following manner: A small amount of 0.022136 g betulin was dissolved in 45 ml water mixed with 5 ml DMSO resulting a final concentration solution of 10^{-3} M. 1 ml of this betulin aqueous solution of 10^{-3} M was added over 1 ml Ag colloid. The final SERS sample concentration was 5×10^{-4} M.

Instrumentation

The 514.5 nm line from an Ar ion laser Spectra Physics was employed for excitation of the SERS spectra of BA. Back scattering configuration was performed with a micro-Raman set-up. The scattered light was focused on the entrance slit of a Dilor-Jobin Yvon Spex Groupe Horiba spectrometer equipped with 1800 grooves mm^{-1} holographic gratings. A CCD camera detection system and analyzing software package LabSpec-3.01C were employed for the acquisition of data. The spectral resolution was 4 cm^{-1} .

The FT-Raman spectra of the polycrystalline betulin and betulinic acid have been recorded using an Equinox 55 Bruker spectrometer with an integrated FRA 106 S Raman module. A Nd: YAG laser operating at 1064 nm was employed for the excitation of the samples. The laser power was set to 400 mW. For the SERS experiments on betulin the 532 nm laser line of a NuDelta mini-Raman spectrometer was employed with an output power of 50 mW.

RESULTS AND DISCUSSIONS

A complete vibrational assignment of the betulin modes has been recently reported by our group based on the DFT calculation [10]. As shown in the Fig. 1, betulin and BA have similar molecular structure, with the exception of the CH_2OH group of betulin in the C28 position which is replaced in the case of betulinic acid by the COOH group. This fact is clearly reflected by the Raman spectra of the both compounds (Fig. 2). Betulinic acid presents characteristic bands at 1685 and 1705 cm^{-1} that differentiate it from betulin.

The SERS spectra of betulin are shown in the Fig. 3. The resulted spectra are reproducible and present some similarities to the previously acquired SERS spectrum of betulinic acid, although the Ag colloidal nanoparticles used for recording the SERS spectrum of BA were prepared according to the classical procedure [11]. Betulinic acid was SERS measured in a final concentration of $2 \times 10^{-3} \text{ mol l}^{-1}$. The SERS signal

encompasses a strong auto fluorescence background and broad bands attributable to the adsorbed species. Their position and relative intensity is clearly different on comparing to the correspondent Raman bands of each molecule.

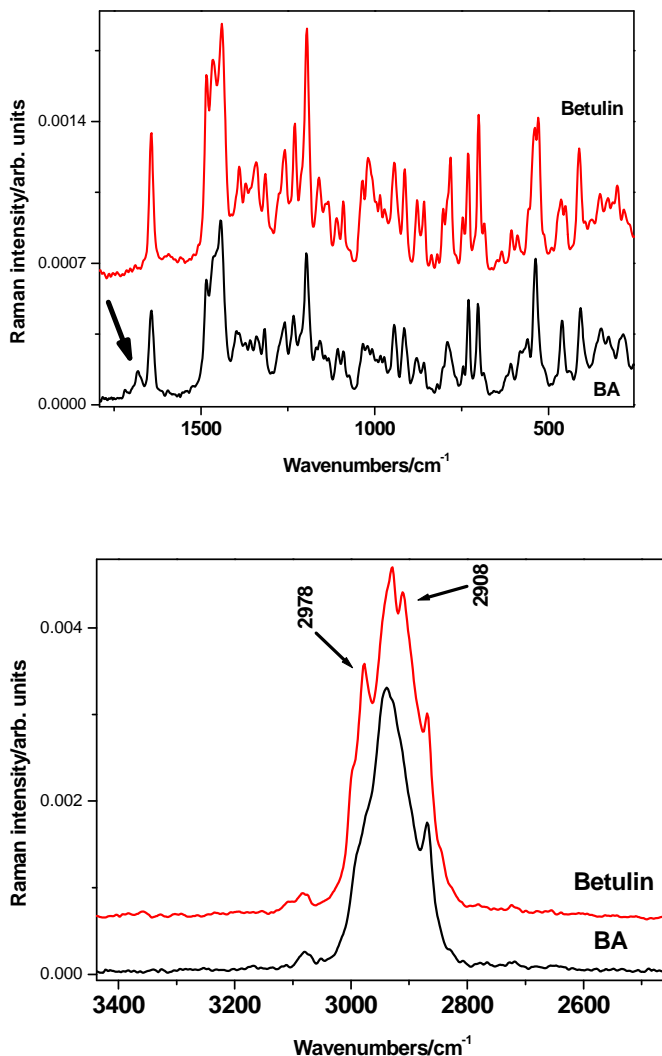


Fig. 2. High (bottom) and low wavenumbers range (top) of the FT-Raman spectra of reference compounds, betulinic acid and betulin. The arrow indicates the betulinic acid distinctive bands attributable to the $-\text{COOH}$ (top) and to CH_2OH additional group of betulin (bottom), respectively.

The major bands observed in the SERS spectrum of betulin are located at 1622 (very strong, with many additional shoulders components), 1367, 1174, 910, 800, 466 and 242 cm^{-1} . When comparing it to the SERS spectrum of betulinic acid some similarities can be observed especially in the high wavenumber region, but also in the low wavenumber region, such as the presence of the very intense band at 242 cm^{-1} .

In the fingerprint spectral range the betulin and betulinic acid SERS spectra present shared characteristics such as common bands in the 1636–1524 cm^{-1} and in the 1373–1171 cm^{-1} spectral region. The SERS spectrum of betulin shows a shoulder at 1646 cm^{-1} and a very intense band at 1622 cm^{-1} , which could be assigned to coupled C=C stretching and CH_2 bending vibrations in the alkene moiety terminal group of betulin. The corresponding band of these vibrational modes appears up-shifted in the Raman spectrum by 23 cm^{-1} .

The SERS spectrum of BA presents a very broaden band at 1606 cm^{-1} with a shoulder at 1636 cm^{-1} . The vibrational assignment of the observed Raman modes [10, 12] concluded that the 1636 cm^{-1} band is assigned to C=O stretching vibrations, while the 1606 cm^{-1} is attributed to C=C stretching mode. This SERS feature is characteristic to molecules containing $-\text{COOH}$ functional group adsorbed on the Ag surface. The shoulder at 1636 cm^{-1} in the SERS spectrum suggests the surface interaction of the carboxyl modes, red-shifted in the Raman spectrum by 10 cm^{-1} .

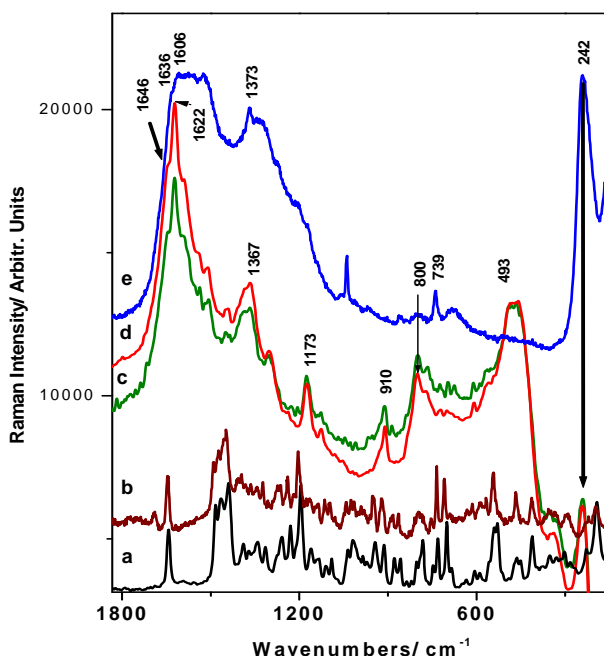


Fig. 3. FT-Raman spectra of betulin (a) and betulinic acid (b) in comparison with the SERS spectra of betulin (c and d) and betulinic acid (e);d-sonicated sample.

The presence of the enhanced $\nu_s(\text{COO})$ mode in the SERS spectrum of BA as a very strong band at 1373 cm^{-1} confirmed a chemisorption of the BA molecule on the surface through the carboxylate group [10]. The SERS spectrum of betulin presents a medium strong broad band located at 1367 cm^{-1} with a shoulder at 1387 cm^{-1} . The shoulder could be assigned to CH_2 bending vibrations in the alkene moiety terminal group and CH_2 wagging vibrations in the CH_2OH group located at the C28 position. The broad band centered at 1367 cm^{-1} combines contributions from the CH , CH_2 and CH_3 bending vibrational modes of the betulin molecule.

The medium-strong band located at 1173 cm^{-1} in the SERS spectrum of betulin can be assigned to the red-shifted band in the Raman spectrum by 21 cm^{-1} located at 1195 cm^{-1} . This is characteristic to ring stretching vibrations and CH_2 and CH_3 rocking vibrational modes of the betulin molecule. The SERS spectrum of betulinic acid also shows a broad band in this region located at 1171 cm^{-1} which also combined C-C, C-H and OH bending vibrations.

In the low wavenumber region a medium band is seen in the SERS spectrum of betulin located at 910 cm^{-1} which could be assigned to CH_2 and CH_3 rocking vibrations of betulin. The strong band at 800 cm^{-1} is assigned to C-C-C skeleton stretching vibrations and CH_2 and CH_3 rocking vibrations as well.

Another strong broad band can be seen in the SERS spectrum of betulin in the $440\text{-}493\text{ cm}^{-1}$ spectral region. According to the theoretical vibrational simulation of modes [10], this band could encompass more contributions from betulin like the CH_2CH_3 bending vibrations and the CH_2OH rocking vibrations among others, which can be seen in the Raman spectrum of betulin in this area.

In the low wavenumber region a strong band can be seen in both SERS spectra of betulin and BA at 242 cm^{-1} assigned to Ag-Cl stretching mode, when chloride ions were used to aggregate the nanoparticles. In the absence of chloride, this band still present in the SERS spectrum of betulin could be tentatively assigned to the Ag-O mode when the $\text{CH}_2\text{-OH}$ terminal is located in the close vicinity of the Ag surface, confirming the chemisorption on the Ag substrate.

Some of the major differences which can be seen between the SERS spectra of betulin and betulinic acid are based on the vibrational modes of the COO^- group that appear in SERS spectrum of betulinic acid. Besides the 1636 and the 1373 cm^{-1} bands discussed above, a sharp medium band can be seen in the SERS spectrum of BA at 739 cm^{-1} which was assigned to COO^- bending vibrations.

The SERS spectra of betulin show in this area more contribution bands that correspond to the medium-strong bands in the Raman spectrum located at 700 and 732 cm^{-1} . These are characteristic to CH_2 twisting vibrations in the alkene moiety group and other CH rocking and bending vibrations.

Considering the modes that are mostly enhanced in the SERS spectrum of betulin, like the band located at 1622 (C=C) or the broad band in the $440\text{-}493\text{ cm}^{-1}$ spectral range, it is tentatively assumed that the alkene moiety is located in the close vicinity of the surface within a standing up orientation of the C=C double

bond. Taking into account the surface selection rules [12], the modes with a perpendicular orientation of the polarizability component with respect the surface would be enhanced. Adsorption of aromatic rings within a parallel orientation with respect to the surface, generally leads to broaden and red-shifted SERS bands. Taking into account the above results, it can be tentatively assumed that betulin molecule interacts with the Ag nanoparticles through the O atom of the CH₂-OH group within a lying-tilted orientation of the skeleton plane, which is also favorable for perpendicular orientation of the C=C double bond of its alkene moiety terminal. This supposition is enhanced by our latest results concerning betulin-cyclodextrin guest-host complex obtained as kneading product [8]. Upon encapsulation, betulin revealed its alkene moiety terminal group free of interaction with the cyclodextrin cavity. These results provide significant information for further studies concerning pharmaceutical formulations of betulin nanoemulsion suitable for antitumoral activity.

CONCLUSIONS

Betulin, as well as other related lupane skeleton structures, exhibits poor solubility, making difficult any properties investigation. However, the SERS spectra of betulin have been obtained from a betulin aqueous solution mixed with DMSO. The idea behind using DMSO solvent for this experiment was especially due to its biomedical applications, since the purpose of further research is to use betulin in ointments or nanoemulsions for skin treatments.

The SERS spectra of betulin were compared with the previously reported SERS spectrum of betulinic acid. Both lupan skeleton structures exhibit broaden SERS bands, the difference in adsorption behavior being generated by the -COOH or -CH₂-OH functional groups, respectively. The large differences between Raman and SERS spectra of betulin among the presence of the enhanced C=C mode and the shifting of the alkene moiety terminal group bands, suggest the chemisorption of the betulin with respect to the Ag nanostructures through the -CH₂-OH group. The C=C double bond of the alkene moiety results in a perpendicular orientation with respect to the Ag surface.

ACKNOWLEDGMENTS

Financial support from the Grant PN-II-ID_ 2284, Nr. 537/2008, and 1257/2007, ANCS, Romania, is highly acknowledged. A. Falamas acknowledges support from the POSDRU/88/1.5/S/60185 project as well.

REFERENCES

1. C. A. Dehelean, S. C. Pinzaru, C. I. Peev, C. Soica, D. S. Antal, *J. Optoelecton. Adv. Mat.*, 9 (2007) 783.
2. C. Gauthier, J. Legault, S. Lavoie, S. Rondeau, S. Tremblay, et al., *J. Nat. Prod.* 72 (2009) 72-81.
3. J. S. Pyo, S. H. Roh, D. K. Kim, J. G. Lee, Y. Y. Lee YY, et al., *Planta Med* 75 (2009) 127-131.
4. Fulda S, Friesen C, Los M, et al. Betulinic acid triggers CD95 (APO-1/Fas) - and p53-independent apoptosis via activation of caspases in neuroectodermal tumors, *Cancer Res*, 57 (1997) 4956– 4964.
5. Fulda S, Scaffidi C, Susin SA, et al. Activation of mitochondria and release of mitochondrial apoptogenic factors by betulinic acid. *J Biol Chem*, 273 (1998) 33942–33948.
6. Fulda S, Jeremias I, Steiner HH, et al. a new cytotoxic agent against malignant brain-tumor cells. *Int J Cancer*, 82 (1999) 435– 441.
7. Malgorzata Drag-Zalesinska, Julita Kulbacka, Jolanta Saczko, Teresa Wysocka, Maciej Zabel, Pawel Surowiak, Marcin Drag, Esters of betulin and betulinic acid with amino acids have improved water solubility and are selectively cytotoxic toward cancer cells, *Bioorganic & Medicinal Chemistry Letters*, 19 (2009) 4814-4817.
8. Fălămaș, S. Cîntă Pînzaru, V. Chiș, C. A. Dehelean, Spectroscopic investigations of newly formed betulin-cyclodextrin guest-host type complexes as potential anti skin cancer candidates, *J. Mol. Struct.*, accepted manuscript, Nov. 2010.
9. N. Leopold and B. Lendl: *J. Phys. Chem. B*, 107 (2003) 5723-5727.
10. Fălămaș, S. Cîntă Pînzaru, C. A. Dehelean C. I. Peev and C. Soica, *J. Raman Spectrosc.* 2010, DOI 10.1002/jrs.2658.
11. J.A. Creighton, G.C. Blatchford, M.A. Albrecht, *J. Chem. Soc. Faraday Trans. 2* (75) (1979) 790.
12. S. Cîntă Pînzaru, N. Leopold, W. Kiefer, Vibrational spectroscopy of betulinic acid HIV inhibitor and of its birch bark natural source, *Talanta* 57 (2002) 625–631.

SYNTHESIS AND CHARACTERIZATION OF SILICA-ENCAPSULATED GOLD NANORODS

A.M. GABUDEAN^{1,*}, D. BIRO² AND S. ASTILEAN^{1,*}

ABSTRACT. Coating gold nanoparticles with well controlable silica layers is currently finding applications in many nanobiotechnology research fields. In this work, we report the mesoporous encapsulation of gold nanorods (GNRs) in a silica layer through a single-step coating method without using a primer ligand. The obtained hybrid nanostructures were optically and morphologically characterized using surface plasmon resonance (LSPR) spectroscopy, dynamic light scattering (DLS) measurements and transmission electronic microscopy (TEM). Theoretical simulations were also performed in order to validate the experimentally observed optical response.

Keywords: gold nanorods; silica coating; surface plasmon resonance; dynamic light scattering; transmission electronic microscopy; FDTD

INTRODUCTION

There is a growing need in designing new nanostructures with attractive properties suitable for biomedical applications. In the past decades, gold nanoparticles have gained considerable attention due to distinctive optical properties related to their unique surface plasmon resonances, originating from the collective oscillation of conduction electrons at metal surface as a response to optical excitation. In particular, thanks to their elongated morphology, gold nanorods (GNRs) possess two plasmon resonances: a transverse one and a longitudinal one, induced by light absorption and scattering along the short and long axis of the particle, respectively. The possibility of tuning the longitudinal plasmonic band from visible to near-IR region by adjusting GNRs aspect ratio, represents an important advantage allowing the use of GNRs in various applications in biosensing, bioimaging and therapy. Recently, a great amount of interest has been paid on encapsulating GNRs in a uniform silica shell able to provide a rich surface chemistry, high biocompatibility, good transparency and controllable porosity [1-4]. Silica is considered to be a suitable coating material as it is an intensively studied biomaterial which can endow the core-shell nanostructures with

¹ Nanobiophotonics Center, Faculty of Physics and Interdisciplinary Research Institute on Bio-Nano-Sciences, Babes-Bolyai University, 42 T. Laurian, 400271, Cluj-Napoca, Romania

* ana.gabudean@ubbcluj.ro; simion.astilean@phys.ubbcluj.ro

² Department of Mechanical Engineering, Faculty of Technical and Human Sciences, Sapientia University, Soseaua Sighisoarei 1C, 540485, Targu-Mures, Romania,

stability, biocompatibility and biofunctionality. By making use of these advantages, the silica coated nanostructures can be further surface-functionalized for diverse biomedical applications including calorimetric diagnostics, photothermal therapy, surface enhanced Raman scattering (SERS) detection and bioimaging. For example, Wang and co-workers developed mesoporous silica-coated gold nanorods for calorimetric sensing of Hg^{2+} and S^{2-} based on their chemical-redox-modulated surface chemistry [5]. Moreover, GNRs coated with porphyrin-doped mesoporous silica shell were proved to be attractive candidates for two-photon imaging and imaging guided therapy through the generation of singlet oxygen by porphyrin molecules [6], while GNRs with a fluorophore-embedded mesoporous silica shell were used to perform fluorescence imaging and spectroscopy measurements on single particles [7]. Also, the use of silica coating strategy for the encapsulation of Raman molecule-tagged gold colloids has been demonstrated to be an efficient procedure for achieving viable SERS tags [8, 9].

In the present work, we performed coating of gold nanorods with a mesoporous silica shell by the addition of tetraethylorthosilicate (TEOS) in a seeded growth process. The formation of a silica layer around GNRs was experimentally confirmed by localized surface plasmon resonance (LSPR) spectroscopy, transmission electron microscopy (TEM) and dynamic light scattering (DLS) measurements. The experimental results were correlated with theoretical simulations employing the Finite-Difference Time-Domain (FDTD) method.

EXPERIMENTAL SECTION

CHEMICALS

Tetrachloroauric acid ($\text{HAuCl}_4 \cdot 4\text{H}_2\text{O}$, 99.99%), cetyltrimethylammonium bromide (CTAB) and ascorbic acid were purchased from Aldrich. Sodium borohydride (NaBH_4 , 99%), silver nitrate (AgNO_3), tetraethylorthosilicate (TEOS) and NaOH were obtained from Merck. All chemicals were used without further purification. Ultrapure water (resistivity $\sim 18.2 \text{ M}\Omega$) was used as the solvent throughout the experiments.

SYNTHESIS OF CTAB-COATED GNRs

First, gold seeds were prepared by adding 1.25 ml of 5 mM HAuCl_4 to 1.25 ml of 0.2 M CTAB under continuous stirring. Next, 0.9 ml of freshly prepared 1 mM NaBH_4 solution was added, all at once, resulting in a brownish yellow seed solution [10].

The growth solution was obtained by mixing 5 ml of 1 mM HAuCl_4 with 50 ml of 0.2 M CTAB and 0.75 ml AgNO_3 (4mM). Thereafter, 0.7 ml of 0.788 M ascorbic acid was added while gently stirring. Ascorbic acid acts as a mild reducing agent changing the color of growth solution from dark yellow to colorless. The final step was the addition of 0.12 ml of seed solution. The color of the solution gradually changed in the first 15-20 min until finally stabilizing.

The obtained solution was centrifuged at 1500 rpm for 10 min to remove the excess CTAB surfactant. The obtained CTAB-coated GNRs were resuspended in ultrapure water for further use [11].

PREPARATION OF SiO₂-COATED GNRs

Firstly, the pH of 2 ml CTAB-coated GNRs in water was adjusted to 10-11 through the addition of 0.1 M NaOH solution. Subsequently, 20 ml of TEOS (20% in methanol) was added under stirring in order to start the silica coating. The reaction was allowed to react for 2 hours. The obtained SiO₂-coated GNRs were then centrifuged and redispersed in water.

EXPERIMENTAL MEASUREMENTS

The extinction spectra were recorded using a Jasco V-670 UV-Vis spectrophotometer with 1 nm spectral resolution. The GNRs in solution were morphologically characterized with conventional transmission electron microscopy (TEM) by using a JEOL 100 U type TEM microscope operated at 100 kV accelerating voltage. Amorphous carbon layer coated collodion substrates, prepared on 300 mesh electron-microscopic copper microgrids, served as substrates used for investigation of gold nanoparticles. The thickness of thermally evaporated carbon layer was in the range of about 4 nm. The nanoparticles size distribution and zeta potential were determined by dynamic light scattering measurements with a Zetasizer Nano-MPT2 (Malvern Instruments).

In order to evaluate the plasmonic resonances, we carried out theoretical calculations by employing the FDTD method using FDTD-SolutionsTM Software from Lumerical Inc [12]. GNRs were treated as cylinders capped with semispherical ends with a length of 42 nm and a width of 12 nm, in good agreement with to TEM measurements, placed in water ($n=1.33$). Gold metallic function was modeled using an empirically obtained dielectric function from literature [13]. Mesoporous silica shell was shaped as a 10 nm layer around the nanorod having a refractive index of 1.39 [14] in order to obtain a shift comparable with that obtained experimentally. We used a grid size of 1 nm and a total field scattered field (TFSF) source with a wave vector normal to the longitudinal axis of the nanorod. This type of source is used to divide the computation volume into two different regions, one including both incident and scattered fields (total field) while the other, scattered field regions only.

RESULTS AND DISCUSSION

As mentioned before, GNRs exhibit two localized surface plasmonic resonances (LSPR) corresponding to the light-induced electron oscillations perpendicular and parallel to the nanorod length direction. The effect of silica coating on the longitudinal and transverse resonances of GNRs is shown in Fig. 1. As we can see, the longitudinal

band undergoes a red shift from 766 nm to 785 nm upon silica deposition, whereas the position of the transverse band from 510 nm remains almost unchanged. Due to the sensitivity of surface plasmon resonance to the refractive index surrounding the metal surface, the red-shift of the longitudinal band can be explained by the increase of the local refractive index induced by the mesoporous silica shell.

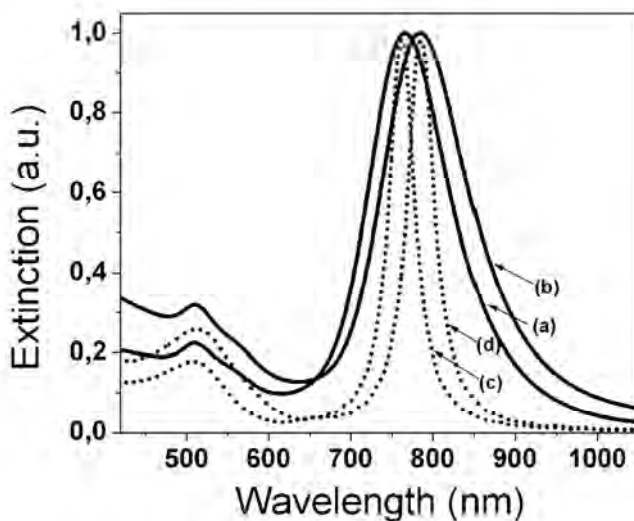


Figure 1. Normalized experimental extinction spectra of CTAB and SiO₂-coated GNRs in water ((a) and (b)) and corresponding simulated spectra obtained for a single nanorod in the absence and presence of a 10 nm silica shell ((c) and (d)).

Figure 1 also illustrates the peak positions of the simulated extinction spectra obtained for a single gold nanorod (length of 42 nm and width of 12 nm) before and after coating with a 10 nm silica shell, which are in good agreement with the experimentally determined positions. The broader feature of the experimental spectrum is typically due to the inhomogeneity of the nanorods aspect ratio and the sensitive dependence of LSPR position on the aspect ratio.

TEM measurements also confirmed the formation of a uniform silica shell around GNRs. Figure 2A shows a typical TEM image of CTAB-coated GNRs of monodisperse shape and size, with average length, width and aspect ratio of 42 ± 3 nm, 12 ± 1 nm and 3.5 ± 0.5 , respectively. In Figure 2B a silica shell of approximately 10 ± 1 nm can be clearly observed surrounding nanoparticles. However, the image also displays the formation of silica chains due to an excess of methanol solution of TEOS in the final mixture, indicating the necessity of supplementary work which needs to be done in order to optimize the procedure.

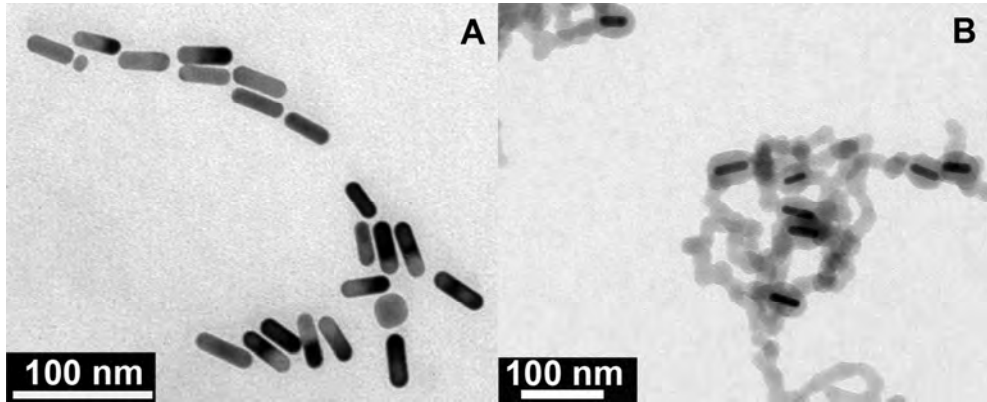


Figure 2. TEM images illustrating CTAB-coated GNRs (A) and SiO₂-coated GNRs (B).

Additionally, dynamic light scattering (DLS) measurements (Figure 3) performed in conjunction with TEM, revealed an increase in the effective hydrodynamic diameter as a consequence of the deposition of a silica layer around GNRs, confirming the results obtained from TEM. Moreover, zeta potential measurements (not shown here) revealed that SiO₂-coated GNRs have an almost neutral potential (+0.06 mV) proving the successful deposition of a silica shell around nanoparticles and desorption of CTAB layer positively charged [15].

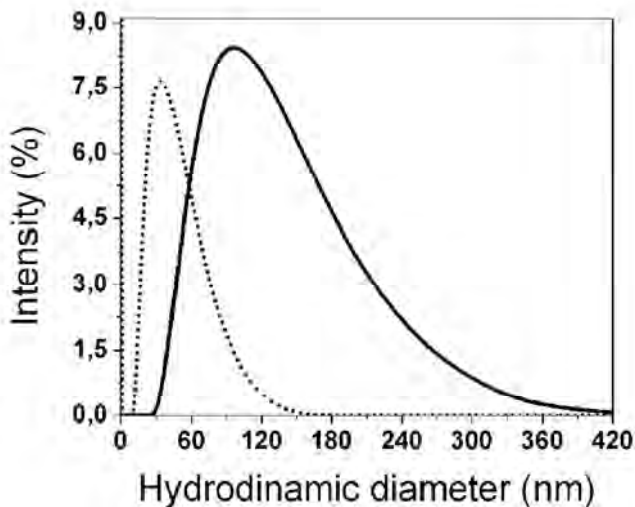


Figure 3. Size distribution of CTAB-coated GNRs (dotted line) and SiO₂-coated GNRs (solid line).

CONCLUSIONS

In summary, we have synthesized gold-silica core-shell nanorods by a direct Stöber synthetic route. The experimentally observed 11 nm red shift of the longitudinal resonance was a direct evidence of the dielectric constant modification around nanorods due to the silica shell deposition. The obtained nanostructures were also characterized using TEM measurements which showed the formation of a 10 ± 1 nm silica layer at the surface of GNRs, thickness also confirmed by the good agreement between experimental extinction spectra of SiO₂-coated GNRs and simulated extinction spectra obtained for a single gold nanorod coated with a 10 nm silica shell. Moreover, DLS and zeta potential measurements confirmed the encapsulation of GNRs in a mesoporous silica layer. The further improvement of the procedure will lead to stable SiO₂-coated GNRs with controllable silica layer thickness, suitable for further bio-functionalization for biomedical applications.

ACKNOWLEDGMENT

This work was supported by CNCISIS in the frame of the PN-II research programs under the project PCCE No 129/2008. A. M. Gabudean also acknowledges Investing in people! Ph.D. scholarship, Project co-financed by the SECTORAL OPERATIONAL PROGRAM FOR HUMAN RESOURCES DEVELOPMENT 2007 – 2013, Priority Axis 1. "Education and training in support for growth and development of a knowledge based society", Key area of intervention 1.5: Doctoral and post-doctoral programs in support of research. Contract no.: POSDRU/88/1.5/S/60185 – "INNOVATIVE DOCTORAL STUDIES IN A KNOWLEDGE BASED SOCIETY" Babeş-Bolyai University, Cluj-Napoca, Romania.

REFERENCES

1. Q. Zhan, J. Qian, X. Li, S. He, *Nanotechnology*, **2010**, 21, 055704.
2. W. L. Zhu, Y. Zhou, J. R. Zhang, *Talanta*, **2009**, 80, 224-230.
3. I. E. Sendroiu, M. E. Warner, R.M. Corn, *Langmuir*, **2009**, 25, 11282-11284.
4. W. Stöber, A. Fink, E. Bohn, *J. Colloid Interface Sci.*, **1968**, 26, 62-69.
5. G. Wang, Z. Chen, W. Wang, B. Yan, L. Chen, *Analyst*, **2010**, Doi: 10.1039/c0an00597e.
6. T. Zhao, H. Wu, S. Q. Yao, Q. H. Xu, G. Q. Xu, *Langmuir*, **2010**, 26, 14937-14942.
7. T. Ming, L. Zhao, Z. Yang, H.J. Chen, L.D. Sun, J.F. Wang, et al., *Nano Lett.*, **2009**, 9, 3896-3903.
8. W. E. Doering, S. M. Nie, *Anal. Chem.*, **2003**, 75, 6171-6176.
9. M. Roca, A. J. Haes, *J. Am. Chem. Soc.*, **2008**, 130, 14273-14279.
10. B. Nikoobakht, M. A. El-Sayed, *Chem.Mater.*, **2003**, 15, 1957-1962.

11. V. Sharma, K. Parka, M. Srinivasarao, PNAS, **2009**, 106, 4981-4985.
12. <http://www.lumerical.com/fdtd.php>
13. P.B. Johnson, R.W. Christy, Phys. Rev. B, **1972**, 6, 4370-4379.
14. Y. S. Chen, W. Frey, S. Kim, K. Homan, P. Kruizinga, K. Sokolov, S. Emelianov, Optics Express, **2010**, 9, 8867-8878.
15. I. Gorelikov, N. Matsuura, Nano Letters, **2008**, 8, 369-373.

RESONANCE INTEGRAL AND THERMAL CROSS-SECTION MEASUREMENTS ON SAMARIUM USING AM-BE AND PU-BE ISOTOPIC NEUTRON SOURCES

STEFAN PAUL GOSULY¹, LIVIU DĂRĂBAN^{1,*}

ABSTRACT. The nuclear reaction mechanism involving resonance neutrons has been studied and the resonance integral and interaction cross-section for the $^{152}\text{Sm}(n,\gamma)^{153}\text{Sm}$ reaction have been calculated after irradiation in the neutron field produced by the ^{241}Am - ^9Be and ^{239}Pu - ^9Be isotopic neutron sources. For the data and calculations to be accurate, corrections have been made all the way. These corrections include neutron self-absorption, gamma-ray attenuation geometry of the samples, geometry of the irradiation site and non-ideality of the epithermal neutron spectrum.

Keywords: resonance neutrons, resonance integral, cross section, isotopic neutron sources.

INTRODUCTION

Samarium (Sm) is a rare earth widely used in nuclear reactors as a neutron absorber because of high thermal and epithermal neutron cross-sections of some of the Sm isotopes (^{149}Sm , ^{152}Sm). It also has a great importance in nuclear medicine for therapeutic purpose because of suitable decay and dose parameters of some of its radioisotopes to be delivered to the patient. The isotope ^{153}Sm is used as one of the β^- emitting therapeutic radioisotopes in nuclear medicine for tumor therapy and bone pain palliation due to its high local beta dose per disintegration and suitable half-life (46.5 h). Also due to its suitable decay characteristics ^{153}Sm is used in *neutron activation analysis*.

Usually, *thermal cross-sections* and *resonance integrals* can be determined experimentally using the *activation method* [1] which consists of foil activation and comparison of the cadmium (Cd) ratios for foils of the interest materials to the cadmium ratios of a reference monitor material. ^{113}Cd is used because of its cut-off property that at 0.5 eV neutron energy, thin Cd foils act as thermal neutron filters.

In general ^{153}Sm can be produced in a nuclear reactor using the $^{152}\text{Sm}(n,\gamma)^{153}\text{Sm}$ reaction and the well known ^{197}Au ($\sigma_0 = 98.65 \pm 0.09 \text{ b}$, $I_0 = 1550 \pm 28 \text{ b}$) as a standard monitor reaction [2]. The accurate knowledge of the thermal neutron cross-section

¹ Faculty of Physics, Babeş-Bolyai University, 400084 Cluj-Napoca, Romania,

* liviu.daraban@phys.ubbcluj.ro

and resonance integral of this reaction become very important when producing ^{153}Sm . This isotope then decays by beta emission to excited states and by gamma emission $E_\gamma = 69.67 \text{ keV}$ (4.85%), $E_\gamma = 103.18 \text{ keV}$ (30%) to the ground state of ^{153}Eu .

It is known that characterizing a highly intense field of neutrons can be difficult mainly because of the burn-up effects that occur in the ^{197}Au monitor resulting in the fact that the activities induced by the neutrons will no longer be proportional to the neutron flux. It has been shown by Karadag et. al. [3] that a lower neutron flux (lower than that of a nuclear reactor) can be used when producing nuclear reactions and calculating cross-sections and resonance integrals. In our case the neutron field of two isotopic neutron sources, $^{241}\text{Am}-^9\text{Be}$ and $^{239}\text{Pu}-^9\text{Be}$, has been used. Also, instead of using the ^{197}Au monitor the ^{55}Mn monitor can be used, mainly because of its resonance parameters. ^{197}Au has its first main resonance at 4.9 eV [4] which is close to the $1/v$ region of the cross-section and thus the activity induced by the epithermal and thermal neutrons cannot be well separated. ^{55}Mn monitor has its first resonance at 337 eV which is quite far from the $1/v$ region, making manganese (Mn) a more suitable monitor than gold (Au). The Westcott correction factor, which accounts for the fact that the cross section does not follow exactly the $1/v$ - law, is very close to unity for Mn ($g_{Mn} = 1.0004$) and Sm ($g_{Sm} = 1.003$) [5].

In our measurements we used diluted oxide forms of the interest materials that were irradiated in the neutron field produced by the two isotopic neutron sources in the Nuclear Laboratory of the Faculty of Physics, UBB Cluj-Napoca (Figure 1). Cylindrical samples were used for the irradiation. In order for the results to be as accurate as possible several corrections have had to be made to our results. These corrections include the effects of neutron self-shielding in the samples, the attenuation of the gamma-rays in the samples, the non-ideality of the epithermal neutron spectrum, the nuclear data uncertainties and the geometry of the irradiation site.

EXPERIMENTAL PROCEDURE

Oxide forms of the materials of interest were prepared from finely grained MnO_2 and Sm_2O_3 powders. They were diluted in Al_2O_3 powder in a percentage of $\text{Al}_2\text{O}_3 - 5\% \text{MnO}_2$ and $\text{Al}_2\text{O}_3 - 3\% \text{Sm}_2\text{O}_3$ in order to minimize the errors due to self-shielding of the thermal and epithermal neutrons in the samples. Al_2O_3 was used because of the low activation cross-section of ^{27}Al and ^{16}O . The powder samples were then introduced in cylindrical polystyrene tubes (*height* = 11 mm, *internal diameter* = 8 mm). They were then exposed to the neutron field in one of the side irradiation holes as can be seen in Figure 1.

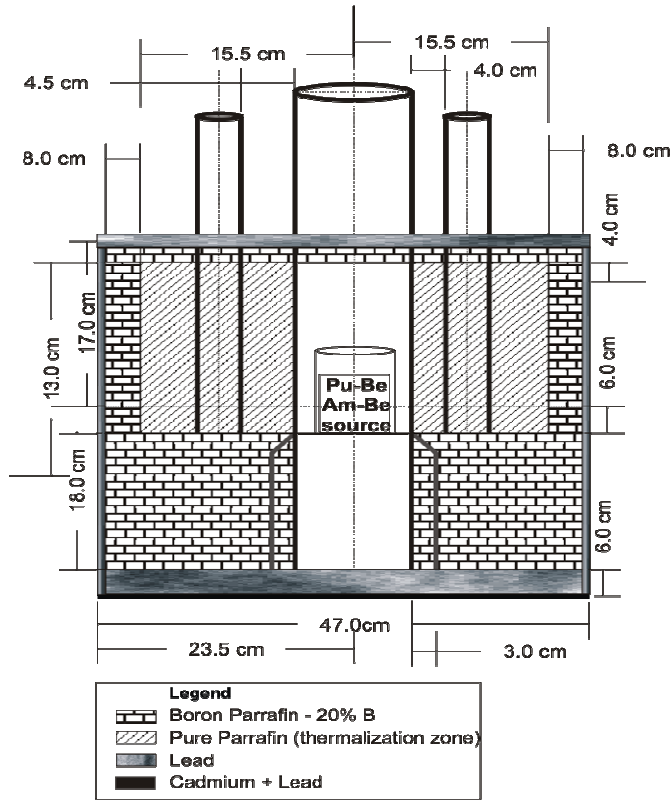


Fig. 1. Irradiation bloc scheme with the $^{241}\text{Am-}^9\text{Be}$ and $^{239}\text{Pu-}^9\text{Be}$ isotopic neutron sources

The characteristics of the irradiated samples are given in Table 1. After the bare samples were irradiated, another set of samples were covered in cylindrical Cd case shields with 1 mm thickness walls. This procedure is known as the *cadmium ratio method* and is described in [6].

The neutron field was obtained from two isotopic neutron sources, immersed in paraffin and covered with a cylindrical lead shield, $^{241}\text{Am-}^9\text{Be}$ with an activity of 5 Ci and $^{239}\text{Pu-}^9\text{Be}$ with an activity of 33 Ci thus having a total activity of 38 Ci.

Table 1.

Characteristics of the samples

Irradiated sample	Target isotope	Mass [g]	Element mass [g]	Sample surface [cm ²]	Sample volume [cm ³]	N [part/cm ³] * 10 ¹⁹
Al ₂ O ₃ -5%MnO ₂	⁵⁵ Mn	0.4646	0.0146	3.7699	0.5529	29.077
Al ₂ O ₃ -3%Sm ₂ O ₃	¹⁵² Sm	0.4459	0.0115	3.7699	0.5529	8.2686

The induced activities of the samples were then measured with the help of gamma spectrometry using a *GC1519 HPGe Detector* (germanium coaxial detector with measuring interval between 50 keV and 10 MeV, relative intrinsic efficiency 15%, resolution 0.9 keV at 122 keV and 1.9 keV at 1332 keV), in conjunction with a *Multiport II multi-channel analyzer (MCA)* and the *Genie2000* gamma spectroscopy software. The efficiency of the detector has been determined with the help of calibrated known activity point sources ^{226}Ra , ^{60}Co , ^{137}Cs , ^{241}Am , ^{133}Ba using various methods presented in literature [7,8]. The efficiency curve obtained is presented in Figure 2. Using the efficiency curve we determined that the photopeak efficiency for the 103.18 keV gamma-ray of Sm is $\varepsilon_p = 23.65\%$ and for the 846 keV gamma-ray of Mn $\varepsilon_p = 3.88\%$.

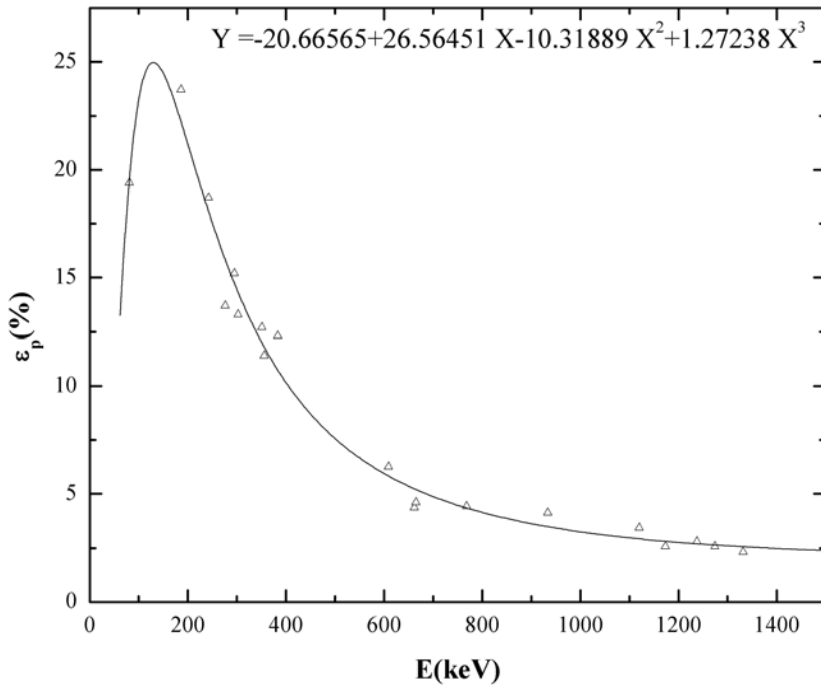


Fig. 2. Photopeak efficiency curve for the HPGe Coaxial Germanium Detector

RESULTS AND DISCUSSIONS

a) Thermal neutron cross section determination

The thermal neutron cross section of the $^{152}\text{Sm}(n,\gamma)^{153}\text{Sm}$ has been determined relative to the value of the $^{55}\text{Mn}(n,\gamma)^{56}\text{Mn}$ reaction which is well known to be $\sigma_{0,Mn} = 13.3 \pm 0.1 \text{ b}$ [1]. It has been calculated using Eq. 1:

$$\sigma_{0,Sm} = \frac{(R_s - F_{Cd} \cdot R_{s,Cd})_{Sm}}{(R_s - F_{Cd} \cdot R_{s,Cd})_{Mn}} \cdot \frac{g_{Mn}}{g_{Sm}} \cdot \frac{G_{th,Mn}}{G_{th,Sm}} \cdot \frac{F_{g,Sm}}{F_{g,Mn}} \cdot \sigma_{0,Mn} \quad (1)$$

where R_s and $R_{s,Cd}$ are the reaction rates per target atom of bare and cadmium covered isotope respectively, F_{Cd} is the cadmium transmission factor that accounts for the fact that the specific epithermal reaction rate of a bare isotope is different from the specific epithermal reaction rate of a cadmium covered isotope, g_{Mn} and g_{Sm} are the Westcott factors that describe the deviation of the cross-section from the $1/v$ - law. For Mn $g_{Mn} = 1.0004$ (20°C) [5] and for Sm $g_{Sm} = 1.003$ (20°C) [5]. The neutron self-shielding effects, which have to be accounted for, are described by the $G_{th,Mn}$ and $G_{th,Sm}$ correction factors. $F_{g,Mn}$ and $F_{g,Sm}$ are the gamma-ray attenuation factors and describe the attenuation of the gamma rays in the volume of the samples, and $\sigma_{0,Mn}$ represents the thermal neutron cross-section of the $^{55}\text{Mn}(n,\gamma)^{56}\text{Mn}$ reaction.

After the determination of the factors in subsections $a_1)$ and $a_2)$ have been made the thermal neutron cross section for the $^{152}\text{Sm}(n,\gamma)^{153}\text{Sm}$ nuclear reaction has been determined relative to the value of the thermal neutron cross-section of the monitor reaction of manganese ($\sigma_{0,Mn} = 13.3 \pm 0.1$ b). A value of $\sigma_{0,Sm} = 202 \pm 0.8$ b has been obtained.

a₁) Specific activities and reaction rates determination

After the irradiation of the bare samples and the cadmium covered samples has taken place, the reaction rates per atom of bare isotope and cadmium covered isotope can be determined with the help of Eq. 2.

$$\begin{cases} R_s = \frac{A_{sp} \cdot F_g \cdot M}{\theta \cdot N_A \cdot \gamma \cdot \epsilon_p} \\ R_{s,Cd} = \frac{A_{sp,Cd} \cdot F_g \cdot M}{\theta \cdot N_A \cdot \gamma \cdot \epsilon_p} \end{cases} \quad (2)$$

with

$$\begin{cases} A_{sp} = \frac{N_p / t_m}{m \cdot (1 - e^{-\lambda_{irr}}) \cdot e^{-\lambda_d} \cdot (1 - e^{-\lambda_m}) / \lambda_m} \\ A_{sp,Cd} = \frac{N_p / t_m}{m \cdot (1 - e^{-\lambda_{irr}}) \cdot e^{-\lambda_d} \cdot (1 - e^{-\lambda_m}) / \lambda_m} \end{cases} \quad (3)$$

where

A_{sp} and $A_{sp,Cd}$ - are the specific activities of the samples after irradiation
 N_p - is the net number of counts under the full-energy peak
 t_m - is the measuring time
 m - is the mass of the irradiated element

λ - is the decay constant

$1 - e^{-\lambda t_{irr}} = S$ - is the saturation factor

t_{irr} - is the irradiation time of the sample

$e^{-\lambda t_d} = D$ - is the decay factor

t_d - the decay time

$(1 - e^{-\lambda t_m}) / \lambda t_m = C$ - represents the correction factor for the decay of the isotope during the measuring time

M - is the atomic weight

θ - is the isotopic abundance

N_A - is Avogadro's number

γ - is the absolute probability of the gamma-ray emission

ε_p - is the full energy photopeak detector efficiency

F_g - is the correction factor describing the attenuation of the gamma-rays in the sample volume for a given gamma-ray energy and can be calculated for a cylindrical sample from Eq. 4:

$$F_g = \frac{\mu x}{1 - e^{-\mu x}} \quad (4)$$

where μ [cm^{-1}] is the linear attenuation coefficient, ρ/μ [cm^2/g] is the total mass attenuation coefficient taken from the XCOM Database [10], ρ [g/cm^3] is the density of the cylindrical sample and x [cm] is the sample height.

Experimental data collected after the irradiation of the samples can be found in Table 2 and the reaction rates per atom calculated with the help of Eq. 2 are given in Table 3.

a₂) Thermal neutron self-shielding correction factor G_{th}

The thermal neutron self-shielding factor G_{th} accounts for the effect of the thermal neutron self-shielding in the studied samples. In other words if the reaction has a large thermal cross-section then the first few outer layers of nuclei in the sample will absorb almost all of the incident thermal neutrons and thus the activation will not be homogenous anymore. For this reason a correction factor which corrects the thermal neutron cross section is defined and determined for cylindrical samples using the method described by Karadag et. al. [3]. Using this method we have obtained a value of $G_{th,Mn} = 0.997$ for Mn and $G_{th,Sm} = 0.991$ for Sm. As can be seen from the values we have obtained, they are close to unity which means that the self-shielding effects have been diminished by diluting our powder of interest in Al_2O_3 .

Table 2.

Experimental data for the samples

target sample	Counts ^a	t _m [s]	t _{irr} [s]	t _d [s]	S	D	C	Sample mass [g]	Element mass [g]	(A _{sp} , A _{sp,Cd}) [Bq/g]
Al ₂ O ₃ +5%MnO ₂	33589	21600	505800	65	1	0.9951	0.4955	0.4647	0.0147	214.7996
(Al ₂ O ₃ +5%MnO ₂) _{Cd}	1087	21600	86400	43	0.9985	0.9968	0.4955	0.4763	0.0150	6.7809
Al ₂ O ₃ +3%Sm ₂ O ₃	3845123	18000	1112400	6689	0.9902	0.9726	0.9635	0.4460	0.0115	516.2168
(Al ₂ O ₃ +3%Sm ₂ O ₃) _{Cd}	242390	18000	853200	6690	0.9712	0.9726	0.9635	0.4446	0.0115	33.2802

^a the net number of counts under the full-energy peak**Table 3.**

Reaction rates per atom of bare and calcium covered isotope

Target sample	Atomic Mass ^a [g]	F _g ^b	θ ^c	γ ^c	ε _p	F _{Cd} ^d	(R _{sp} , R _{s,Cd})*10 ⁻²⁰
Al ₂ O ₃ +5%MnO ₂	54.938	1.03	1	0.989	0.039	1 ^e	52.32
(Al ₂ O ₃ +5%MnO ₂) _{Cd}	54.938	1.03	1	0.989	0.039	1 ^e	1.65
Al ₂ O ₃ +3%Sm ₂ O ₃	151.919	1.103	0.267	0.298	0.236	0.982 ^f	764.83
(Al ₂ O ₃ +3%Sm ₂ O ₃) _{Cd}	151.919	1.103	0.267	0.298	0.236	0.982 ^f	49.31

^a taken from [9].^b calculated with the help of [10].^c taken from [11].^d for E_{Cd} = 0.55 eV.^e taken from [12].^f taken from [13].

b) Resonance integral determination

The resonance integral describes the contribution of the epithermal and resonance neutrons (with energies up to 2 MeV) to the capture cross-section.

An ideal epithermal neutron spectrum obeys the well-known $1/E$ -law. In the case of an ideal spectrum the resonance integral (including the $1/v$ region of the thermal neutron spectrum) is defined by:

$$I_0 = \int_{E_{Cd}}^{\infty} \sigma(E) \cdot \frac{1}{E} dE \quad (5)$$

where $\sigma(E)$ describes the energy dependence of the cross section and E_{Cd} represents the cadmium cut-off energy. De Corte et. al [14] have shown that this definition of the resonance integral (Eq. 5) is not useful when dealing with non-ideal epithermal neutron spectrums. In a real epithermal neutron spectrum which can be well described by a $1/E^{1+\alpha}$ dependence the neutron spectrum is defined by:

$$I_0(\alpha) = \int_{E_{Cd}}^{\infty} \sigma(E) \cdot \frac{(1eV)^\alpha}{E^{1+\alpha}} dE \quad (6)$$

where $\Phi_e \sim 1/E^{1+\alpha}$ is the real epithermal fluence rate per unit $(E^{-\alpha}/\alpha)1 eV^\alpha$ of neutron energy interval and I_0 is the resonance integral which has to be used when calculating the epithermal neutron activation in a real epithermal spectrum. The deviation from the ideal spectrum is described by the dimensionless α parameter which can be experimentally determined.

De Corte et. al [15] have also shown that there is a tight connection between I_0 , as tabulated in literature, and $I_0(\alpha)$ which is valid only in an epithermal neutron spectrum characterized by the α parameter. The equation which describes this is:

$$I_0(\alpha) = (1eV)^\alpha \left[\frac{I_0 - 0.426 \sigma_0}{(\bar{E}_r)^\alpha} + \frac{0.426 \sigma_0}{(2\alpha + 1)(E_{Cd})^\alpha} \right] \quad (7)$$

where the term $I_0 - 0.426\sigma_0$ represents the reduced resonance integral with the $1/v$ region subtracted and σ_0 is the 2200 m/s (n,γ) cross-section, \bar{E}_r represents the *effective resonance energy* as described by Ryves et. al. [16]. Eq. 7 is only valid for $E_{Cd} = 0.55 eV$, since $0.426 = 2(E_0/E_{Cd})^{0.5}$, with $E_0 = 0.025 eV$ and $E_{Cd} = 0.55 eV$.

The value of the resonance cross section integral has been determined relative to that of the $^{55}\text{Mn}(n,\gamma)^{56}\text{Mn}$ reaction ($I_0 = 14 \pm 0.3 b$) [1] by using the following relation:

$$I_0(\alpha)_x = I_0(\alpha)_{Mn} \cdot \frac{(R-1)_{Mn}}{(R-1)_x} \cdot \left(\frac{G_e}{G_{th}} \right)_{Mn} \cdot \left(\frac{G_{th}}{G_e} \right)_x \cdot \frac{\sigma_{0,x}}{\sigma_{0,Mn}} \quad (8)$$

where $I_0(\alpha)$ is the resonance integral corresponding to an α characterized epithermal neutron spectrum, $R = A_{sp}/A_{sp,Cd}$ represents the cadmium ratio, G_{th} and G_e are the thermal neutron self-shielding factor and epithermal neutron self-shielding factor respectively, α is the parameter which characterizes a real epithermal spectrum, and σ_0 are the thermal neutron cross-sections.

In the determination of the resonance integral for the Sm reaction Eq. 8 has been used. The $I_0(\alpha)_{Sm}$ value obtained was then converted into $I_{0,Sm}$ using Eq. 7. The result was $I_{0,Sm} = 2601 \pm 213$ b. The values for the epithermal neutron self-shielding factor G_e and the α parameter have been calculated in sections b₁) and b₂).

b₁) Epithermal neutron self-shielding correction factor G_e

The epithermal neutron self-shielding factor G_e accounts for the effects of self-shielding which can occur in the sample volume during irradiation and measurement. For this reason a correction factor has been defined. In our work we have determined the G_e factor by using a method described by Gonçalves et. al. [17]. We have obtained a value of $G_{e,Mn} = 0.963$ for Mn and $G_{e,Sm} = 0.446$ for Sm.

b₂) Epithermal neutron shape spectrum α -parameter determination

The epithermal neutron shape spectrum α -parameter is an energy independent correction factor, positive or negative, depending on the irradiation conditions (moderator, irradiation geometry).

The deviation from the ideal $1/E$ epithermal spectrum (see Figure 3) has been calculated using the *double monitor method* [14,15] and cadmium ratios for two nuclear reactions: $^{197}\text{Au}(n,\gamma)^{198}\text{Au}$ and $^{115}\text{In}(n,\gamma)^{116}\text{In}$. Thin foils have been used in order to minimize the neutron self-shielding effects. The characteristics of the foils can be observed in Table 4.

Table 4.

Characteristics of the irradiated monitor foils

Reaction	Foil mass [g]	Foil thickness [mm]	σ_0 ^a [b]	I_0 ^a [b]	\bar{E}_r ^b [eV]	G_e	E_{Cd} [eV]	R
$^{197}\text{Au}(n,\gamma)^{198}\text{Au}$	1.285	0.32	9.87E+01	1.57E+03	5.47	0.263	0.55	10.376
$^{115}\text{In}(n,\gamma)^{116}\text{In}$	1.435	0.32	2.02E+02	3.22E+03	1.51	0.265	0.55	15.001

^a taken from [4]

^b taken from [15]

The dual monitor method consists of irradiating two thin foils of known cross-sections. Au and In reactions are suitable because their cross-sections have a $1/v$ dependence up to 1-2 eV.

After the two foils have been irradiated in the same position, they have been covered in 1 mm thick Cd-covers in order to separate the thermal neutron activation from the epithermal neutron activation. After calculating the reaction rates for each of the bare and Cd-covered foils, the cadmium ratios have been built and using Eq. 9, using a graphical solution (see Figure 4), the α parameter has been determined to be $\alpha = -0.33$.

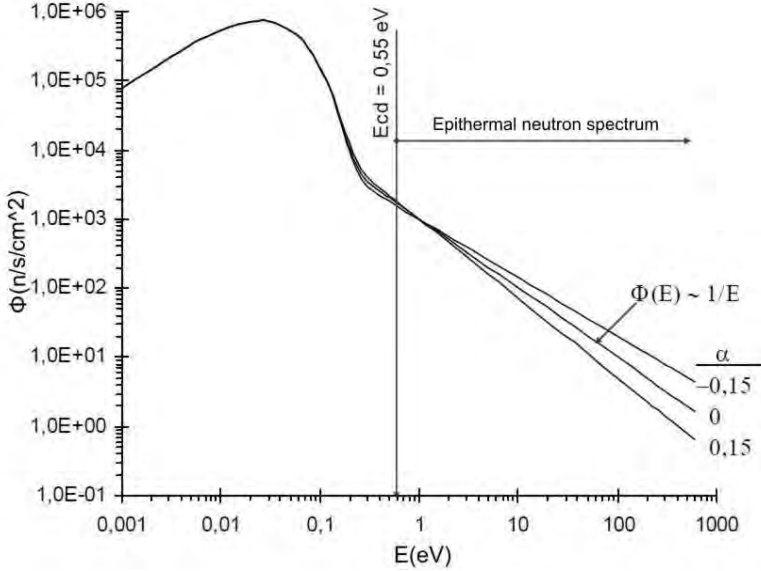


Fig. 3. Deviation from the ideal $1/E$ epithermal neutron spectrum

$$\Omega(In / Au) = \frac{(R - 1)_{Au}}{(R - 1)_{In}} = \frac{[(Q_0 - 0.426)FG_e]_{Au} \cdot (\bar{E}_{r, Au})^{-\alpha} + C}{[(Q_0 - 0.426)FG_e]_{In} \cdot (\bar{E}_{r, In})^{-\alpha} + C} \quad (9)$$

with

$$C_\alpha = \frac{0.426}{(2\alpha + 1)E_{Cd}^\alpha} \quad (10)$$

where $\Omega(In/Au)$ represents the ratio of the epithermal reaction rate per nucleus of the two monitors, $Q_0 = (I_0/\sigma_0)$ for the ideal case of an ideal $1/E$ epithermal neutron spectrum, \bar{E}_r is the effective resonance energy as defined by Ryves [16], E_{Cd} is the cut-off energy of cadmium.

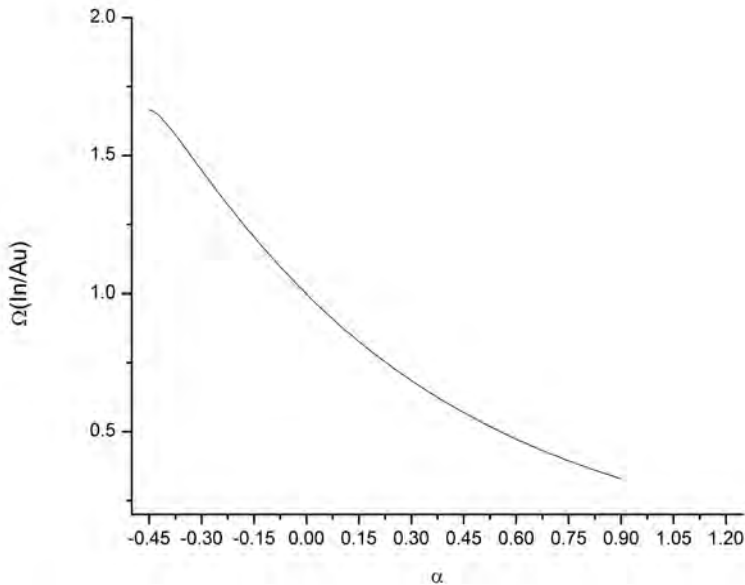


Fig. 4. α parameter characteristic curve

c) Error analysis

When we deal with experimental data the presence of errors is natural. One's goal should always be to minimize any kind of errors, systematic and random ones, in order for the final results to be as accurate as possible. When talking about experimental accuracy, the dual monitor method that we used has an important advantage that large uncertainties due to gamma-ray attenuation and detector efficiency are canceled by using cadmium ratios. For this matter we used in our determination the *error propagation theory* [14]. The individual uncertainties and overall uncertainty can be seen in Tables 5 and 6.

Table 5.

Error analysis in the determination of the thermal cross-section of the Sm reaction

Error analysis (thermal cross-section)		
Uncertainties:	Uncertainties (%)	
	Mn	Sm
Statistical errors	0.39	0.18
Detection efficiency	2.75	2.55

Sample mass		0.01	0.01
Half-life		0.04	0.45
Isotopic abundance		0	0.6
Branching factor		0.3	1.34
G_{th}		0.01	0.01
Monitor thermal cross-section		0.75	0
F_{CD}		0	0.8
Westcott factor (g_w)		0.05	0.05
TOTAL ERROR	4.23	2.89	3.09

Table 6.

Error analysis in the determination of the resonance integral of the Sm reaction

Error analysis (resonance integral)			
Uncertainties:	Uncertainties (%)		
	Mn	Sm	
Cadmium ratio	1.71	3.24	
G_{th}	0.01	0.01	
G_{epi}	0.2	2.5	
σ_0	1.1	4.23	
Westcott factor (g_w)	0.05	0.05	
Monitor resonance integral	3.13	0	
α	3.61	2.41	
Effective resonance energy	0.45	0.09	
TOTAL ERROR	8.22	5.21	6.36

CONCLUSIONS

We have studied nuclear resonance reactions involving neutrons and produced the ^{153}Sm , ^{56}Mn , ^{198}Au , ^{116}In isotopes in the laboratory. We have also studied the activation method, the cut-off cadmium method and the cadmium ratio method in order to measure the thermal neutron cross-section and resonance integral for a particular (n, γ) reaction. We have experimentally measured and determined the thermal neutron

cross-section and the resonance integral for the $^{152}\text{Sm}(n,\gamma)^{153}\text{Sm}$ nuclear reaction by preparing cylindrical bare and cadmium covered samples which were irradiated in the neutron field produced by two isotopic neutron sources $^{241}\text{Am}-^9\text{Be}$ and $^{239}\text{Pu}-^9\text{Be}$. All the correction factors were calculated for the case of cylindrical samples. We have obtained a value of $\sigma_{0,Sm} = 202 \pm 0.8 b$ for the thermal neutron cross-section and a value of $I_{0,Sm} = 2601 \pm 213 b$ for the resonance integral. These values are in good agreement with other data published in literature as can be seen from Table 7.

Table 7.

 Literature values σ_0 and I_0 for the $^{152}\text{Sm}(n,\gamma)^{153}\text{Sm}$ reaction

Year	Reference	Thermal cross-section (σ_0) [b]	Resonance integral (I_0) [b]	Cd cut-off energy (E_{Cd}) [eV]
2010	This work	202±8	2601±213	0.55
2007	[18]	204.8±7.9	3038±214	0.55
2005	[19]	205.88	2968.41	0.5
2005	[20]	205.952	2990.92	-
2003	[21]	202±7.27	2909±122	0.55
1998	[22]	206	2982.9	0.5
1984	[23]	206±6	2970±100	0.5
1978	[24]	204±9	3050±360	0.5
1973	[25]	-	2700	0.5
1972	[26]	210±10	2530±150	0.5
1962	[27]	209±9	3162±104	0.5
1960	[28]	215±10	2740±150	0.5
1956	[29]	250±50	-	-

REFERENCES

1. J. Moteff, et al., Neutron fluence measurements, Technical Report Series No. 107, IAEA, Vienna, 1970.
2. S.F. Mughabghab, et al., Neutron Cross Section from Neutron Resonance Parameters and Thermal Cross Sections, Academic Press, New York, 1981.
3. M. Karadag, H. Yucl, M. Tan, A. Ozmen, Nucl. Instr. Meth A 501 524-535, 2003.
4. National Nuclear Data Center, BNL, <http://www.nndc.bnl.gov/>
5. J. Chang, Table of the nuclides, Korea Atomic Energy.
6. H. K. Beckurts, K. Wirtz: Neutron Physics, p 277-282, Springer-Verlag, Berlin, 1964.
7. Z. B. Alfassi, F. Groppi, Nucl. Instr. Meth. A, 574, 280-284, 2007.
8. S. Harb, K. Salahel Din, A. Abbady: Proceedings of the 3rd Environmental Physics Conference, 19-23 Feb. 2008, Aswan, Egypt.

9. M. Wieser, M. Berglund, *Pure Appl. Chem.*, 81, 2131-2156, 2009.
10. M. J. Berger, J. H. Hubbel: XCOM Photon Cross Sections Database, NBSIR 87-3597, 1987.
11. Sonzogni, A. (Ed.), 2005. Nuclear Data (NuDat) Retrieval Program (<http://www.nndc.bnl.gov/nudat2/>, Nuclear Wallet Cards database version of 10/11/2005, Decay Radiation database version of 11/28/ 2005, Levels and Gammas database version of 11/29/2005), National Nuclear Data Center, Brookhaven National Laboratory, Upton, NY, USA.
12. El Nimr, T., De Corte, F., Moens, L., Simonits, A., Hoste, J., Epicadmium neutron activation analysis (ENAA) based on the k₀- comparator method. *J. Radioanal. Chem.* 67 (2), 421–435 1981.
13. El Nimr, T., Ela-Assaly, F.M., Determination of the attenuation of epicadmium neutrons using the method of varying Cd-thickness. *J. Radioanal. Chem.* 109 (1), 3–9 1987.
14. De Corte, F., Simonits, A., De Wispelaere, A., The accuracy and precision of the experimental α -determination in the $1/E^{1+\alpha}$ epithermal reactor neutron spectrum, *J. Radioanal. Chem.* 62, (1-2), 209-255, 1981.
15. F. De Corte, L. Moens, K. Sordo-El Hammami, A. Simonits, J. Hoste: Modification and generalization of some methods to improve the accuracy of α -determination in the $1/E^{1+\alpha}$ epithermal neutron spectrum, *J. Radioanal. Chem.* 52, (2), 305-316, 1979.
16. T. B. Ryves, *Metrologia*, 5, 119, 1969.
17. F. Gonçalves, E. Martinho, J. Salgado, Extention to cylindrical samples of the universal curve of resonance neutron self-shielding factors, *Nucl. Instr. Meth. B*, 213, 186-188, 2004.
18. Yucel, H. et al.: Measurement of the thermal neutron cross section and resonance integral for (n, γ) reaction in ¹⁵²Sm, *Annals of Nucl. Energy* 34, 188-193, 2007.
19. ENDF/B-VI, 2005.: Evaluated Nuclear (reaction) Data File (Release 8). NNDC, BNL.
20. JEFF-3.1, 2005.: Evaluated Data Library OECD Nuclear Energy Agency.
21. Kolotov, V.P., De Corte, F.: An electronic database with a compilation of k₀ and related data for NAA. *Journ. Radioanal. Nucl. Chem.* 257 (3), 501-508, 2003.
22. BROND-2.0, 1998.: Russian Evaluated Neutron Reaction Data Library. Institute for Physics and Power Engineering, Obninsk, Russia.
23. Mughabghab, S.F.: Neutron Cross Sections, Neutron Resonance Parameters and Thermal Cross-Sections. Part B, Z=61 – 100, vol. 1, Academic Press Inc., New York, 1984.
24. Heft, R.E.: A consistent set of nuclear parameter values for absolute instrumental neutron activation analysis. In: *Proceedings of the International Conference on Computer in Active Analysis*, Mayaguez, p. 495, 1978.
25. Sakata, H.H., Nagayama, S., Japan Atomic Energy Research, Tokai, 1973.
26. Steinnes, E.: Resonance activation integrals of some nuclides of interest in neutron activation analysis. *J. Inorg. Nucl. Chem.* 34, 2699-2703, 1972.
27. Cabell, M.J.: Neutron capture cross-section data for Sm-152. *J. Inorg. Nucl. Chem.* 24, 749, 1962.
28. Fehr, E., Hansen, E.: Fission-product cross-section measurements. KAPL-2000-12, I, 33, 1960.
29. Walker, W.H.: The relative abundances and pile neutron capture cross sections of the isotopes of samarium, gadolinium, dysprosium and ytterbium (Thesis), McMaster University, Hamilton, Ontario, 1956.

HIGH-FIELD CW-EPR STUDY ON COLICIN-A PROTEIN

C. GRUIAN^{1,2}, L. URBAN², H. BRUTLACH², L. V. PATMAVATHI²,
H.-J. STEINHOFF², S. SIMON¹

ABSTRACT. In this work were analyzed cw W-band EPR spectra recorded in the temperature range from 115K to 300K on colicine A by fitting the different spectral components in the g_{xx} region addressing the possible origin of those components. The study aims to investigate the g_{xx} heterogeneity in W-band spectra of colicine A in two different spin labeled positions, col A 105 and col A 169, in terms of fractions of molecule populations characterized by different polarity and numbers of H-bonds to the nitroxide group. The obtained g_{xx} values as well as the fractions of different populations are correlated to the temperature.

Keywords: bacteriocin, colicin A, EPR.

1. Introduction

Colicins are toxins that kill their targets either by nuclease activity or by forming pores in the cytoplasmic membrane of the target cell [1]. Colicin A is a water-soluble toxin consisting in a pore forming protein that selectively kills microorganisms causing no harm to the host by forming a voltage-gated channel in the cytoplasmic membrane of target bacteria [2]. It can be used as a model protein for evidencing folding and conformational changes of proteins. Its investigation could provide a better understanding of the biological principles underlying microbial defense mechanisms and providing useful information for designing antibiotics [3]. Smarda et al. and Lancaster et al. reported that colicins can selectively kill tumor cells [4, 5].

The functional mechanism of many membrane proteins involves a transient change in structure that occurs on the millisecond time scale. To explore such molecular mechanisms requires techniques that can provide structural information about proteins under native conditions with a high time resolution. The recently introduced method of site-directed spin labeling (SDSL) meets these requirements [6]. In this technique, a spin label side chain is introduced at a selected site via cysteine substitution mutagenesis followed by modification of the unique sulfhydryl group with a specific paramagnetic nitroxide reagent [7]. The spin labeling might cause perturbation in the protein structure and might affect the function of a protein. Therefore, the function of the spin-labeled proteins should be checked prior to study by EPR. The most commonly used spin label is the methanethiosulphonate (MTS) spin label.

¹ Faculty of Physics, Babes-Bolyai University, 400084, Cluj-Napoca, Romania

² Department of Physics, University of Osnabrück, 49069 Osnabrück, Germany

Colicin A bearing a unique cysteine was spin-labeled with the methanethiosulphonate (MTS) spin label.

The continuous wave (cw) EPR spectrum yields information about the nitroxide side chain mobility, the solvent accessibility, the polarity for its immediate environment, and the distance between the nitroxide and another paramagnetic center in the protein [7].

The polarity analysis based on the determination of the hyperfine coupling between the unpaired nitroxide electron and the nitrogen nucleus could inform on electric field effects [8], due to shifts in the spin-density from oxygen towards the nitrogen atom depending on the electric field along the NO bond. Polarity also influences the g -tensor elements, with g_{xx} being the most sensitive component.

But the EPR parameters are not only affected by the solvent polarity but also by hydrogen bonding to the oxygen atom of the nitroxide, which contributes significantly to g_{xx} . It has been shown that especially g_{xx} is additionally sensitive to the existence of H-bonds to the nitroxide oxygen [8-10]. Determination of g_{xx} is used to characterize the proticity profiles of membranes and interpreted as penetration depth of water molecules. To resolve the anisotropy of the g -tensor (i.e. the g_{xx} splitting) is required a higher spectral resolution in the g_{xx} area, so we used W-band EPR spectroscopy.

The present study is focused on colicin A, a pore-forming protein. The cw-EPR spectra are analysed by fitting the different spectral components in the g_{xx} region addressing the possible origin of those components.

2. Experimental procedures

The high-field cw-EPR measurements were performed on a home-built W-band EPR spectrometer (3.4 T, 95 GHz, cw) at University of Osnabruck [11]. Experiments were performed in a range of temperature from 115K to 300K, and the sample suspensions were filled into quartz capillaries with an inner diameter of 0.6 mm (VitroCom Inc., N.J., USA) for the temperatures lower than 265K and 0.2 mm (VitroCom Inc., N.J., USA) for higher temperatures. The cw measurements at low temperature were performed with the microwave power attenuated to $3 \cdot 10^{-6}$ W, the B-field modulation was set to 100 kHz and the amplitude adjusted to 0,15 mT. For each sample were accumulated 16 spectra, for temperatures from 10 to 10, between 115K and 265K. The presented spectra are averages of two to four spectra and each was detected with a 0.02 mT resolution. Microwave phase was adjusted to an accuracy estimated to be $\pm 1^\circ$ and calibration of the magnetic field setting was performed using a Mn^{2+}/MgO standard. Repeated test calibration showed that the B-field value can be determined with a mean deviation of less than $2 \cdot 10^{-5}$ T. Additional systematic errors of $9 \cdot 10^{-6}$ T at maximum may result from inaccuracies in the g and hyperfine splitting values of Mn^{2+} ($g=2.00101 \pm 0.00005$; $a=-87.10 \pm 0.03$ G). Other systematic inaccuracies in order of 10^{-5} T may result from errors of the frequency measurements, but cancel out almost completely in the determination of g_{xx} and A_{zz} of the spin labels samples.

Simulated powder spectra were fitted to experimental spectra using a modified version of the program DIPFIT [12], where up to three different g_{xx} values and the corresponding fractions of these spectral contributions can be fitted simultaneously to the experimental spectra. The components A_{xx} and A_{yy} of the hyperfine tensor, which are less sensitive to polarity changes are approximated as constant with values of 0.52 G and 0.45 G.

The spin label used was MTS spin label (1-Oxyl-2,2,5,5,-tetramethyl-3-pyrroline-3-methyl) methanethiosulfonate ($C_{10}H_{18}NO_3S_2$) and it has been purchased by Toronto Research Chemicals Inc., Canada, and used without further purification. The solvent used is bidistilled water ($\epsilon_{293K} = 80.4$), and it was purchased by Sigma-Aldrich.

3. Results and discussion

For several temperatures one could observe the presence of two, three, and in particularly for col 169 at 265K even four distinct shoulders in the spectral region assigned to g_{xx} value (Fig. 1), the g -tensor component directed along the NO bond. One can see the heterogeneity of the g_{xx} region, where four peaks become visible. Another explanation seem to be cogitable besides the assumed influence of H-bonds, namely the hyperfine splitting in the g_{xx} region. But it was also shown by others that in the case of nitroxide radicals in aqueous solution, the NO moiety is strongly hydrated by two water molecules [13, 14]. So, the explanation of this splitting in the g_{xx} region is the formation H-bonds between two water molecule and the nitroxide oxygen.

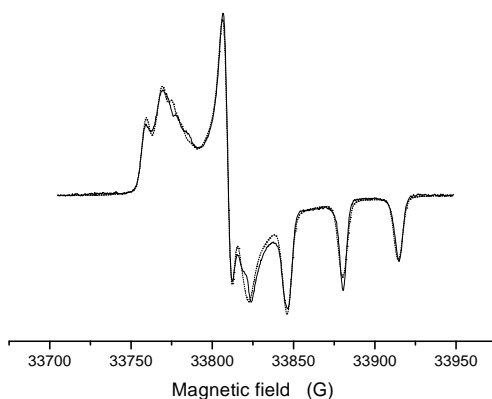


Fig. 1. Experimental (straight line) and simulated powder (dotted line) high-field EPR spectra recorded at 265K for col169.

One can see also from the plotting of the g_{xx} values and the g_{xx} fractions against temperature that these are not very much temperature dependent and the fg_{xx3} fraction is higher in colA 169 than in colA 105 (Figs. 2 and 3). A fraction of 24% was observed for the population without any H-bond (fg_{xx1}), 66% for the population with

one formed H-bond (fg_{xx2}) and 10% for the population with 3 H-bonds (fg_{xx3}) for colA 105, and in case of colA 169 a fraction of 42% was observed for the population without any H-bond (fg_{xx1}), 35% for the population with one formed H-bond (fg_{xx2}) and 23% for the population with 3 H-bonds (fg_{xx3}). Although, in both cases, the fraction for two H-bonds is clearly smaller than for one.

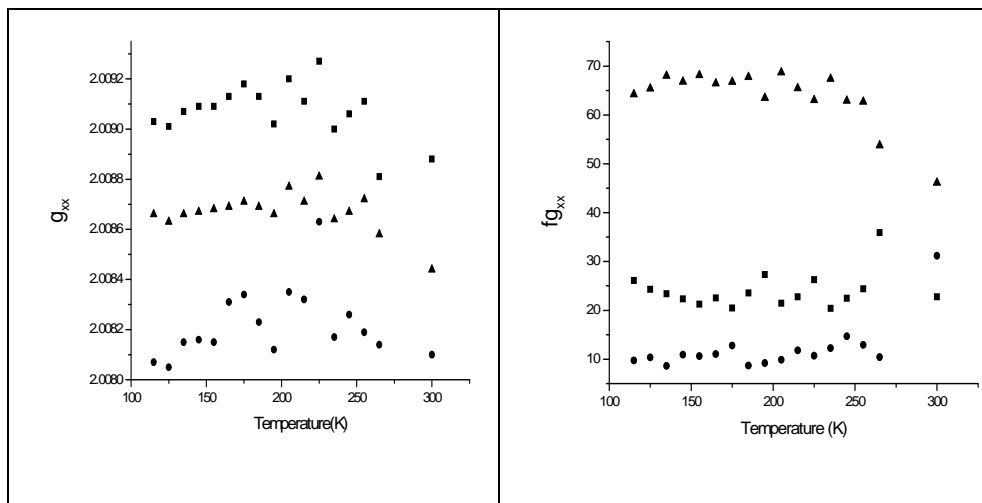


Fig. 2. The g_{xx} and fg_{xx} values plotted against temperature for colA 105; the fitting was made with 3 components (\blacksquare g_{xx1} , \blacktriangle g_{xx2} , \bullet g_{xx3}).

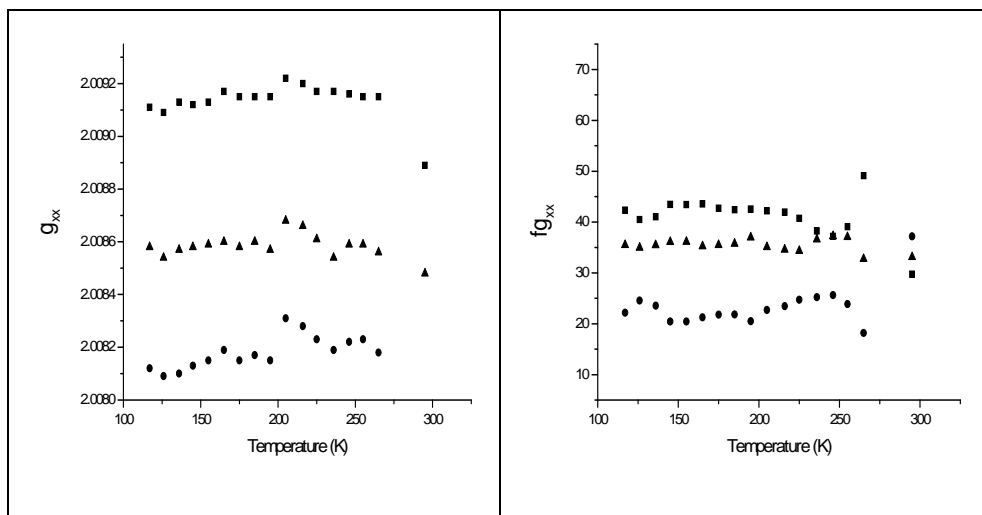


Fig. 3. The g_{xx} and fg_{xx} values plotted against temperature for colA 169; the fitting was made with 3 components (\blacksquare g_{xx1} , \blacktriangle g_{xx2} , \bullet g_{xx3}).

4. Conclusions

The results presented in this work indicated that the hydrogen bonding to the NO group of nitroxide spin labels appear already at low temperatures, and the fractions of populations with different numbers of H-bonds remain constant during the increase of temperature. The g -tensor is the most sensitive to hydrogen interactions, hydrogen bonding causing a decrease in g_{xx} in both cases presented here: colA 105 and colA 169.

ACKNOWLEDGEMENTS

C.G. author wishes to thank for the financial support provided from programs co-financed by The SECTORAL OPERATIONAL PROGRAMME HUMAN RESOURCES DEVELOPMENT, Contract **POS DRU 6/1.5/S/3** – „Doctoral studies: through science towards society”.

REFERENCES

1. J.H. Lakey, F.G. van der Goot, F. Pattus, *Toxicology*, 87 (1994) 85.
2. P.V.L. Padmavathy, H.-J. Steinhoff, *J. Mol. Biol.* 378 (2008) 204.
3. R.G. Panchal, M.L. Smart, D.N. Bowser, D.A. Williams, S. Petrou, *Curr. Pharm. Biotechnol.* 3 (2002) 99.
4. J. Smarda, M. Fialova, J. Smarda Jr, *Folia Biol-Prague*, 47 (2001) 11.
5. D. Walker, L. Lancaster, R. James, C. Kleanthous, *Protein Sci*, 13 (2004) 1606.
6. W.L. Hubbel, C. Altenbach, *Curr. Opin. Struc. Biol.* 4 (1994) 566.
7. H.-J. Steinhoff H-J, *Front. Biosci.* 7 (2002) 97.
8. O.H. Griffith, P.J. Dehlinger, S.P. Van, *J. Membrane Biol.* 15 (1974) 159.
9. M. Plato, H.-J. Steinhoff, C. Wegener, J.T. Topping, A. Savitsky, K. Mobius, *Mol. Phys.* 100 (2002) 3711.
10. H.-J. Steinhoff, A. Savitsky, M. Pfeiffer, M. Plato, K. Mobius, *Biochim. Biophys. Acta.* 1457 (2000) 253.
11. H. Brütlich, E. Bordignon, L. Urban, J.P. Klare, H.J. Reyher, M. Engelhard, H.-J. Steinhoff, *Appl. Magn. Reson.* 30 (2006) 359.
12. N. Radzwill, K. Gerwert, H.-J. Steinhoff, *Biophys. J.* 80 (2001) 2856.
13. V. Barone, A. Bencini, M Cossi, A. Di Matteo, M Mattesini, F. Totti, *J. Am. Chem. Soc.* 120 (1998) 7069.
14. M.C.R. Symons, A.S. Pena-Nunez, *J. Chem. Soc., Faraday Trans.* 81 (1985) 2421.

METHOD VALIDATION FOR FREE AMINO ACIDS DETERMINATION IN BIOLOGICAL SAMPLES

ELENA HORJ, ANDREEA IORDACHE, MONICA CULEA¹

ABSTRACT. A sensitive analytical method for free amino acids determination in biological samples was developed by isotopic dilution mass spectrometry. The method was validated. Deconvolution of the ion abundance ratios to yield tracer-to-tracee ratios for the isotopomers was done using Brauman's least squares approach. Significant differences were observed between the amino acid levels measured in biological samples.

Keywords: *amino acids, isotope dilution, gas chromatography-mass spectrometry.*

Introduction

The measurements of isotopic abundances need careful preparation of standard mixtures and careful attention to the analytical parameters of the system to be studied. The mass spectrometric methods for amino acid determination in biological samples need to use some steps as extraction procedures, addition of an internal standard, derivatization methods, separation by gas chromatography and calculation methods [1-5].

Quantitative determination was performed by addition to the sample, before extraction, of known amounts of internal standard, the isotopic labelled analogue of one of the amino acids of interest. The method will compensate the sample losses in the clean-up stage, assuming that the losses of the standard are identical with those of the analyte. The use of isotopic tracers demands accurate measurements of the isotopic abundances of each tracer in order to construct a design matrix of simultaneous linear equations. The system of equation may be solved by standard matrix algebraic techniques [6, 7].

The aim of this study was to validate the method for amino acid determination in biological samples. The method could be applied in biotechnological, medical or food control studies.

Materials and method

A gas chromatography-mass spectrometry method is presented to measure the amino acids standards by using ¹⁵N-methionine as internal standard. The method

¹ Babes-Bolyai University, Biomedical Physics Dept., 1 Kogalniceanu str, 3400 Cluj-Napoca, Romania
e-mail: mculea@phys.ubbcluj.ro

had good analytical linearity between 0 and 150 $\mu\text{g}\cdot\text{mL}^{-1}$ and both precision and accuracy were lower than 11% for determination of amino acids in meat samples. Sensitivity permitted analysis of 100 pg amino acid on column. The concentrations of the amino acids were determined after addition of 20 μg (^{15}N)methionine as internal standards per gram of meat. The resultant tracer spectrum for methionine requires deconvolution of the enrichment of the isotopomer of the amino acid. Deconvolution of the ion abundance ratios to yield tracer-to-tracee ratios for each isotopomer was done using Brauman's least squares approach.

Experimental

^{15}N -methionine, 99 atom % ^{15}N was used as internal standard. A Trace DSQ ThermoFinnigan quadrupole mass spectrometer coupled with a Trace GC were used in the conditions: electron energy 70 eV; electron emission 100 μA and ion source temperature 250°C. Amino acids were separated on a Rtx-5MS capillary column, 30 m x 0.25 mm, 0.25 μm film thickness, using a temperature program from 50°C, 1 min, 6°C/min at 100°C, 4°C/min at 200°C, 20°C/min at 300°C, (3min). The transfer line temperature was 250°C, the injector temperature 200°C, splitter: 10:1. Helium was the carrier gas with a flow rate 1ml min^{-1} . The fragment ion m/z 171 for methionine and the ion m/z 172 for the internal standard were monitored for quantitative analyses.

Extraction procedure:

One gram of the defrosted meat with 1 g of fine quartz sand were thoroughly ground in a thick ceramic dish and homogenized with 5 ml distilled water. After centrifugation for 5 min, 0.5 ml of the supernatant was passed through a Dowex 50W-W8 exchange resin, on a 2 x 40 mm column and eluted with 4M NH_4OH . A two-step derivatization procedure was applied: esterification with 200 μl butanol-acetyl chloride (4:1 v/v) for 1h at 100°C and trifluoroacetylation with 100 μl trifluoroacetic anhydride at 60°C for 30 min [4].

Results and Discussion

Method validation:

Regression curve obtained by using the mass spectrometric method and the least squares with matrix calculation were compared to correlate the levels of the amino acid in different sorts of meat. Regression curve obtained by using standards with known concentration of methionine in the range 0-100 $\mu\text{g}\cdot\text{mL}^{-1}$ adding the same quantity of the internal standard, 20 $\mu\text{g}\cdot\text{mL}^{-1}$, was $y=0.0355x + 0.1319$. The correlation coefficient was 0.9995.

The use of the isotopic labeled analogue of the analyte (the amino acid of interest) as internal standard and the presence of the analyte (tracer) with their natural isotopic abundance in meat necessitate careful correction of the mass spectrum, to

deconvolute the information of interest. Fractional isotopic abundances for natural methionine and isotopomer were calculated from experimentally measured isotopic ratios and synthetic isotopic ratios in the case when the isotopomer needed was missing. The set of simultaneous linear equations, each describing the isotopic contributors had to be solved having the general form:

$$I_x = \sum_{x=i,j} A_i X_j \quad (1)$$

where I_x represents the relative ion abundance for the x^{th} ion; X_j represents the unknown fractional abundance. The relative abundance of the contributors (A_i) was calculated for the two ions expressing the simultaneous equations in matrix notation:s

$$I = AX \quad (2)$$

The least squares solution of X can be obtained by using the inverse of A transpose:

$$X = (A^T A)^{-1} A^T I \quad (3)$$

Table 1 is an example of a matrix construction in our experimental study.

Table 1.

The matrix design (left) and the pseudoinverse matrix (right) used for methionine calculation

methionine [M]			methionine [M]		
	[M]	[M+1]		[M]	[M+1]
n.a.	0.95	0.05	n.a.	1.05	-0.05
^{15}N	0.01	0.99	^{15}N	-0.01	1.01

In the design matrix, in the position [M+1] for methionine (m/z 171), especially the natural contribution of the isotope ^{13}C is presented. In the case of ^{15}N -methionine (m/z 172), in the position [M+1], especially the contribution of ^{15}N -methionine (99 atom % ^{15}N), is presented but also the contribution of the isotope ^{13}C .

Methionine was calculated by matrix and regression curve calculation. The correlation between the two methods was very good, obtaining a correlation coefficient of 0.998.

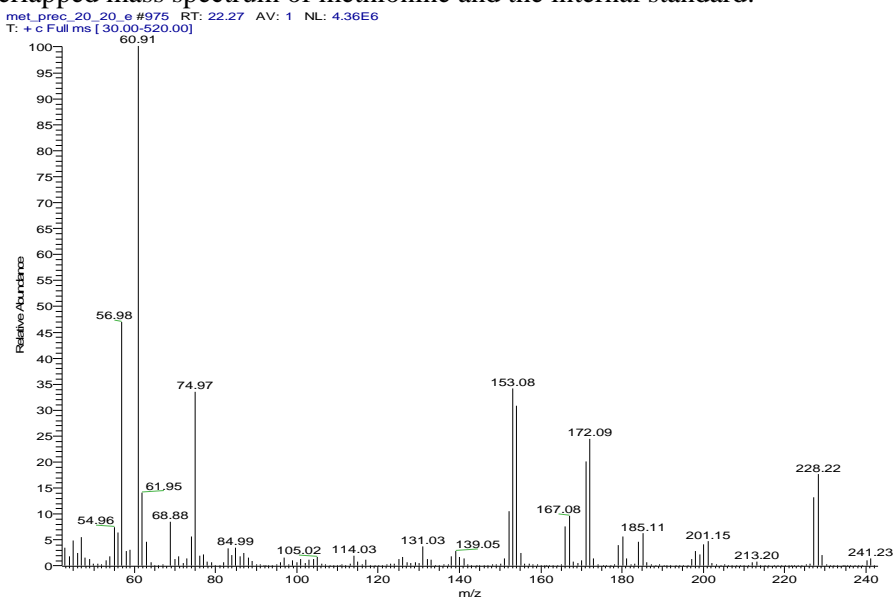
Precision and accuracy for methionine was measured for two standards of 20 and respectively 30 $\mu\text{g mL}^{-1}$. The calculated values for precision and accuracy were lower than 6% and respectively 11% (Table2).

Table 2.

The precision and accuracy for methionine determination

Standard	Precision,RSD(%)	Accuracy, RSD(%)
20µg, n=7	5.48	10.94
30µg, n=5	3.85	6.76

The method was validated by using amino acid standards. The elution order of the amino acids was: alanine (Ala), glycine (Gly), threonine (Thr), serine (Ser), valine (Val), leucine (Leu), isoleucine (Ile), proline (Pro), methionine (Met), aspartic acid (Asp), phenylalanine (Phe), lysine (Lys), glutamic acid (Glu), tyrosine(Tyr), histidine (His). The standards have followed the described extraction and derivatization procedure (n=3). Precision gave lower value than 20% for R.S.D., except Tyr and a sensitivity value lower than 10 ng of amino acid injected. All the samples followed the same extraction and derivatization steps. Figure 2 presents the mass spectrum of methionine mixed with ¹⁵N-methionine.. The ion m/z 171 was selected for quantitative measurements of methionine together with the corresponding ion of the labeled methionine, m/z 172. Figure 1 presents the overlapped mass spectrum of methionine and the internal standard.

**Fig. 1.** The mass spectrum of methionine and ¹⁵N-methionine

The results obtained for the amino acid standards gave good correlation coefficients, higher than 0.99 for Ala, Gly, Thr, Ser, Leu, Ile, Pro, Hy-Pro, Orn. The precision and accuracy was lower then 20%, excepted the amino acids:Cys, His and Arg. The L.O.D. was lower than 0.1µg/mL⁻¹.

METHOD VALIDATION FOR FREE AMINO ACIDS DETERMINATION IN BIOLOGICAL SAMPLES

The regression curves were used to calculate the amino acids in meat samples. A comparison between different sorts of meat is presented. Calculation was also made by using the value of methionine obtained by matrix calculation and respons factors. A good correlation was obtained between the two calculation methods ($y = 1.0624x + 1.195$, $r=0.998$).

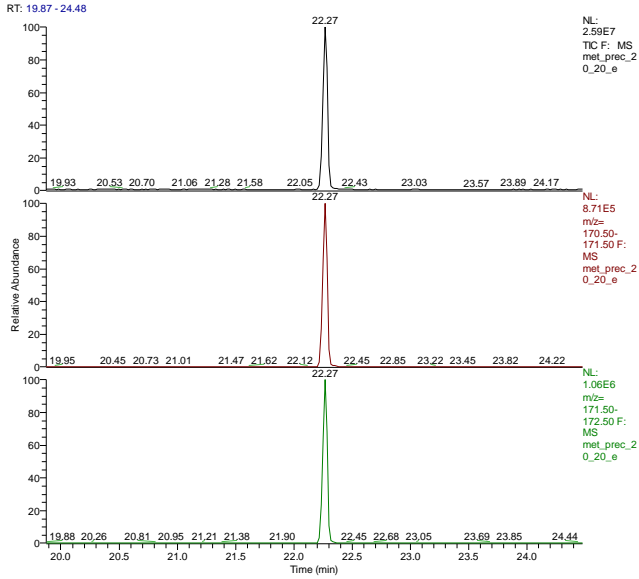


Fig. 2. The total ion current (TIC) chromatogram of methionine (up) and methionine and internal standard peaks for m/z 171 and m/z 172

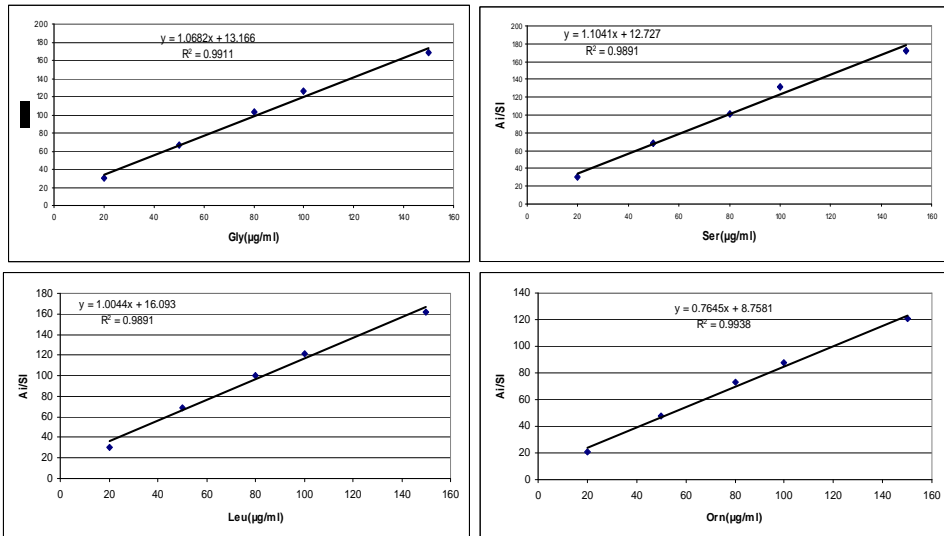


Fig. 3. Regression curves of some of the determined amino acids: Gly, Ser, Leu, Orn

The linearity results for some of the studied amino acids are presented in Figure 3.

Table 3 presents the regression curves and the coefficients of correlation for the standards amino acids studied. The chromatograms of separation of the amino acids from different meat samples are presented in Figure 4.

The method was applied for free amino acid determination in beef, pork (Figure 4) and a salami mixture meat as presented in Table 4. Essential amino acids are higher in beef and pork meat while flavor amino acids are higher in mixture meat.

Table 3.

The regression curve and the coefficient of correlation (r) obtained for the studied amino acids

Amino acid	Regression curve	r
Alanine (Ala)	$y = 1.017x + 12.567$	0.991
Glycine (Gly)	$y = 1.0682x + 13.166$	0.996
Threonine (Thr)	$y = 1.1285x + 15.058$	0.992
Serine (Ser)	$y = 1.1041x + 12.72$	0.995
Leucine (Leu)	$y = 1.0044x + 16.09$	0.995
Isoleucine (Ile)	$y = 0.8507x + 12.37$	0.994
Valine (Val)	$y = 1.5124x - 13.434$	0.980
Cysteine (Cys)	$y = 0.1667x - 6.512$	0.940
Gama-aminobutiric acid(GABA)	$y = 2.207x - 8.8747$	0.980
Proline (Pro)	$y = 1.0331x + 20.49$	0.991
Hydroxyproline (Hy-Pro)	$y = 1.3504x - 4.257$	0.993
Ornithine (Orn)	$y = 0.7645x + 8.7581$	0.997
Phenylalanine (Phe)	$y = 0.6542x + 26.844$	0.978
Tyrosine (Tyr)	$y = 0.3209x - 5.2564$	0.973
Lysine(Lys)	$y = 1.2868x - 10.384$	0.978
Histidine (Hys)	$y = 0.6916x - 10.196$	0.957

Table 4.

Comparative values of amino acids levels in a mixture, beef and pork meat

	mg/g	mixture	pork	beef
1	Ala ³	1.18	1.29	2.43
2	Gly ³	0.33	0.42	0.67
3	Thr ^{1,3}	0.24	0.29	0.55
4	Ser ³	0.13	0.10	0.18
5	Val ¹	4.89	7.60	6.39
6	Leu ¹	0.5	0.56	1.38
7	Ile ¹	0.44	0.43	1.08

METHOD VALIDATION FOR FREE AMINO ACIDS DETERMINATION IN BIOLOGICAL SAMPLES

8	Pro	0.57	0.59	1.06
9	Met ¹	0.06	0.01	0.01
10	Asp ¹	0.51	0.48	1.18
11	Phe ^{1,4}	0.32	0.36	0.85
12	Orn ¹	0.11	0.00	0.15
13	Glu ²	15.83	4.95	13.77
14	Lys ¹	1.23	1.09	2.21
15	Tyr ⁴	0.1	0.33	0.20
16	His ¹	4.86	10.01	12.29
total(mg/g)		31.29	28.51	44.40
EAA		12.84	20.46	25.23
FAA		15.83	4.95	13.77
SAA		1.64	1.81	3.29
FRAA		0.42	0.70	1.05

Note: ¹-essential amino acids (EAA); ²-flavor-related amino acids (FAA); ³-sacharinity-related AA(SAA); ⁴-fragrant-related amino acids(FRAA)

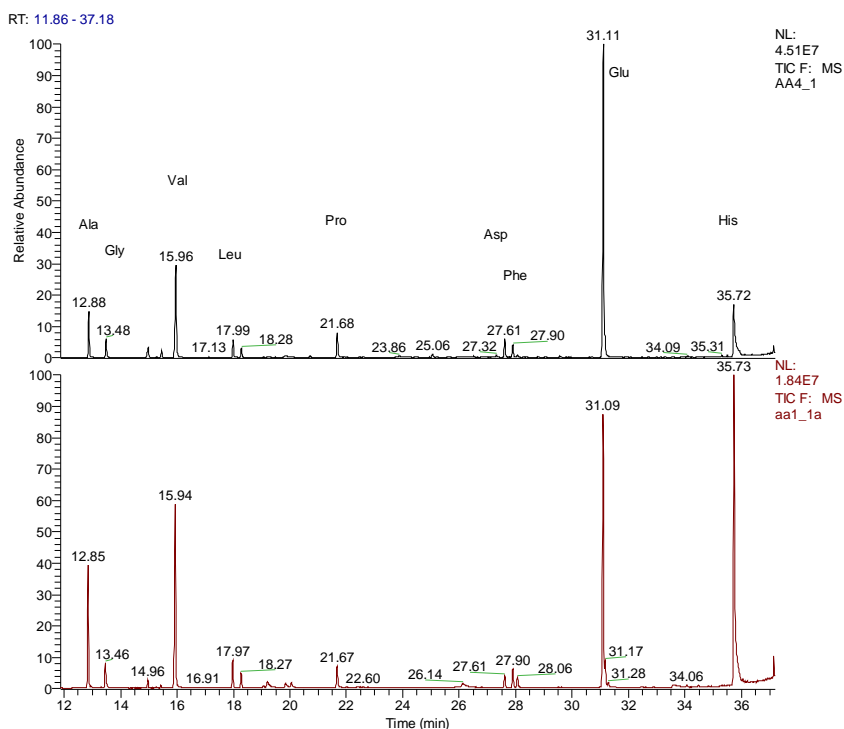


Fig. 4. Comparison of free amino acids separation chromatograms in a mixture of beef, pork meat, grease and a beef meat

Conclusions

GC-MS and the isotope dilution mass spectrometric method used are precise and accurate. The regression curve method of calculation gave similar results as the matrix calculation method ($r=0.999$) for methionine. Significant differences were observed between the amino acid levels measured in different sorts of meat.

REFERENCES

1. M. Culea, O. Cozar, D. Ristoiu *JMS* **41**, 1594-1597 (2006).
2. T. Hodisan, M. Culea, C. Cimpoiu, A. Cot, *J Pharm. Biomed. Anal.* **18**, 319 – 32 (1998).
3. A. Iordache, M. Culea, M. Jimborean, A. Pintea, M. Chiriac, *Journal of Environmental Protection and Ecology- JEPE*, 2009, **10**, 149 – 155.
4. M. Culea, A. Iordache, C. Mesaros, "*Chemické listy*" *J.*, **102**, s636 – 638 (2008).
5. Jin S. K., I. S. Kim, H. J. Jung, D. H. Kim, Y. J. Choi, S. J. Hur, *Poultry Science*, **86**, 2676–2684(2007).
6. J. I. Brauman, *Spectral Analysis: Methods and Techniques*, Ed. by J. A. Blackburn, Marcel Dekker, New York (1970).
7. K.Nakamura, D.L. Hachey, C.S. Kreek, C.S. Irving, P.D. Klein, *J Pharm Sci.* **71**, 40 (1982).

SYNTHESIS AND MORPHO-STRUCTURAL ANALYSIS OF TiO₂- AU COMPOSITES

V. IANCU¹, G. MELINTE¹, L. BAIA¹, L. BARBU-TUDORAN², C. COSMIN³,
V. DANCIU³, V. COSOVEANU³, M. BAIA^{1,*}

ABSTRACT. Several nanocomposites based on TiO₂ aerogel and Au colloidal nanoparticles have been successfully obtained through different synthesis methods. For the purpose of obtaining the desired TiO₂ anatase phase, the samples underwent a certain heat treatment. The porous-like structure of all the nanocomposites has been observed by scanning electron microscopy (SEM). Quantitative values of the specific surface areas of the pores have been determined by using N₂ adsorption method. The sample with the highest specific surface area was synthesized by impregnating the TiO₂ gel with gold colloid. This result is very promising for photocatalytic testing knowing that the anatase crystalline phase, which builds up the structure of this sample, enhances the photocatalytic activity. The existence of Au nanoparticles inside the porous network was found to influence the dimensions of the TiO₂ crystallites. The mean size of the anatase nanocrystals has been determined from the Raman-XRD data correlation for all of the investigated samples and the values were confirmed by transmission electron microscopy (TEM) results.

Keywords: *TiO₂ aerogel, Au colloidal particles, nanocomposites, morphological and structural analysis;*

1. Introduction

One of the most pressing problems of today's society is pollution. The means and techniques applied in controlling this problem are numerous and very diverse. The domain of physical chemistry has sought out different materials with suitable properties for this task. Photocatalysis is a promising method used in degradation of different water or air organic pollutants.

Aerogels are unique among solid materials. They have extremely low densities, large open pores and a high inner surface area. This results in interesting physical properties, for example extremely low thermal conductivity and low sound velocity combined with high optical transparency and high homogeneity.

¹ Faculty of Physics, Babes-Bolyai University, M. Kogalniceanu 1, 400084, Cluj-Napoca, Romania

² Faculty of Biology & Geology, Babes-Bolyai University, Clinicilor 5-7, 400006, Cluj-Napoca, Romania

³ Faculty of Chemistry and Chemical Engineering, Babes-Bolyai University, Arany Janos 11, 400028, Cluj-Napoca, Romania

* Corresponding author. E-mail: monica.baia@phys.ubbcluj.ro

They are prepared from molecular precursors by sol-gel processing in which the liquid component of the gel has been replaced by a gas [1].

TiO₂ it is a nontoxic material, with chemical stability, high photosensitivity, large band-gap and low cost. Because of the high photocatalytic response TiO₂ aerogels are widely used in manufacturing materials used for decontaminating water, air and soil [1-4]. Highly porous composites based on TiO₂ nanopowders and Au nanoparticles have proven to have improved photocatalytic properties due to the capacity of the Au nanoparticles to store and, subsequently, release electrons [5], thus influencing the energy transfer processes [6-8].

Control on the morphology of the composites is very important in order to obtain the desired photochemical properties [9]. In the present work our first interest was to prepare the nanocomposites based on TiO₂ aerogels and Au nanoparticles through different methods of synthesis, and then to characterize them morphologically and structurally. In order to determine the composite with the highest surface area, N₂ adsorption measurements have been performed. We further analyzed the samples structurally by using Raman spectroscopy and X-ray Diffraction (XRD) techniques, and morphologically by performing scanning electron microscopy (SEM) and transmission electron microscopy (TEM) measurements.

2. Experimental section

2.1. Sample preparation

Gold colloid preparation

The gold colloidal suspension was prepared by the following procedure: 100 ml of 10⁻³ M chloroauric acid (HAuCl₄) was brought to a boil with vigorous stirring on a magnetic stirring hot plate. Ten milliliters of 38.8 mM sodium citrate (Na₃C₃H₅O(COO)₃) was added to the solution all at once under vigorous stirring. The yellow solution turned clear, dark blue and then a deep red-burgundy color within a few minutes. Stirring and boiling was continued for 15 min after the burgundy color was observed. The solution was removed from heat and kept stirring until it was getting cold and then the volume was adjusted to 100 ml by adding water [10].

TiO₂ gel preparation

The TiO₂ gel was obtained by sol-gel method using titanium isopropoxide (TTIP), nitric acid (HNO₃), ethanol and water (H₂O) with 1/0.08/21/3.675 molar ratio. The gels were allowed to age for about 40 days. All of the gels were supercritical dried (T > 35⁰C and p > 1200 psi) using SAMRI-PVT 3D (Tousimis) equipment and liquid CO₂. The Au free TiO₂ aerogel was obtained for comparison purpose and it will be further denoted **C0**.

TiO₂-Au composites preparation

The TiO₂-Au composites were obtained by three different methods.

a) The TiO₂ aerogel was introduced in the colloidal solution where it was maintained for two days. Au-TiO₂ composite was separated by filtration and then dried in an oven at 100⁰C. This sample will be further denoted **C1**.

b) The TiO₂ gel was introduced in the colloidal solution where it was maintained for two days. The gels impregnated with colloidal nanoparticles were washed with plenty of alcohol and supercritical dried with liquid CO₂. This sample will be further denoted **C2**.

c) The nanocomposite was obtained by adding the gold colloidal solution in the synthesis mixture of the TiO₂ gel. The resulted gel was allowed to age and then dried under supercritical conditions. This sample will be further denoted **C3**.

All of the obtained samples were heat treated at 500⁰C for 2 hours.

2.2. Sample measurements

The surface area of the samples was determined by the Brunauer-Emmet-Teller (BET) method, in a partial pressure range of 0.05<P/Po<0.3. The nitrogen adsorption was carried out at 77 K.

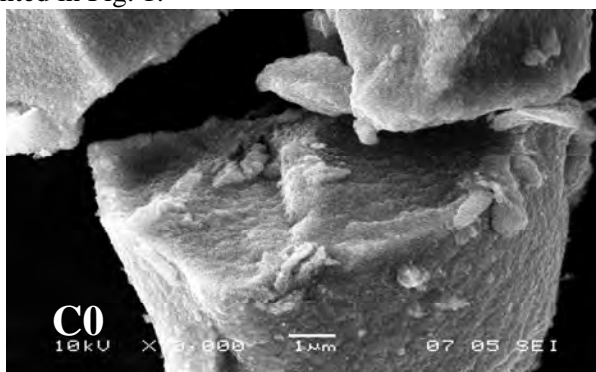
The SEM images were collected with a JEOL JSM 5510LV scanning electron microscope and the TEM images were obtained using a JEOL JEM 1010 transmission electron microscope.

The XRD patterns were obtained at room temperature using a Bruker D8 Advance diffractometer. The used source was CuK α with a power of 1600 W (40 kV and 40 mA)

The FT-Raman spectra were recorded using a Bruker Equinox 55 spectrometer with an integrated FRA 106 Raman module. The laser excitation beam came from an Nd-YAG laser of 1064 nm. The spectral resolution was of 1 cm⁻¹.

3. Results and discussion

The porous character of the prepared nanocomposites was observed by performing SEM measurements. A selection of SEM images of the heat treated samples is presented in Fig. 1.



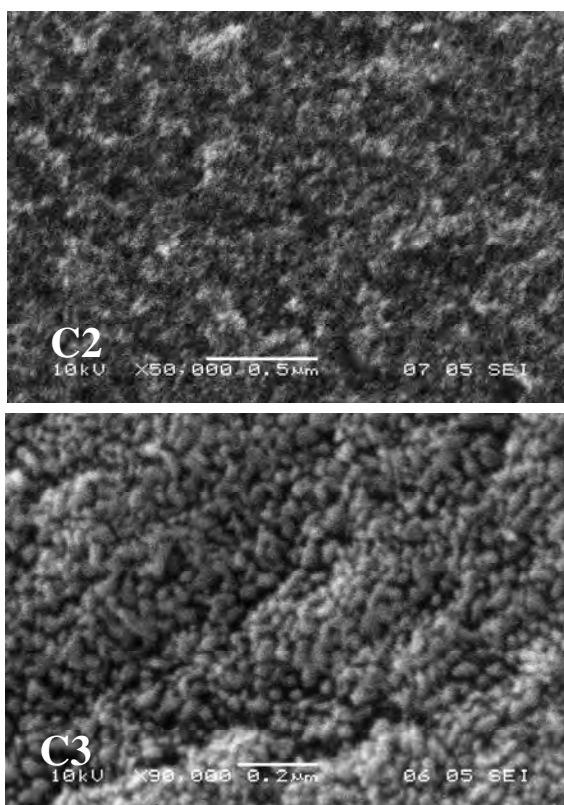


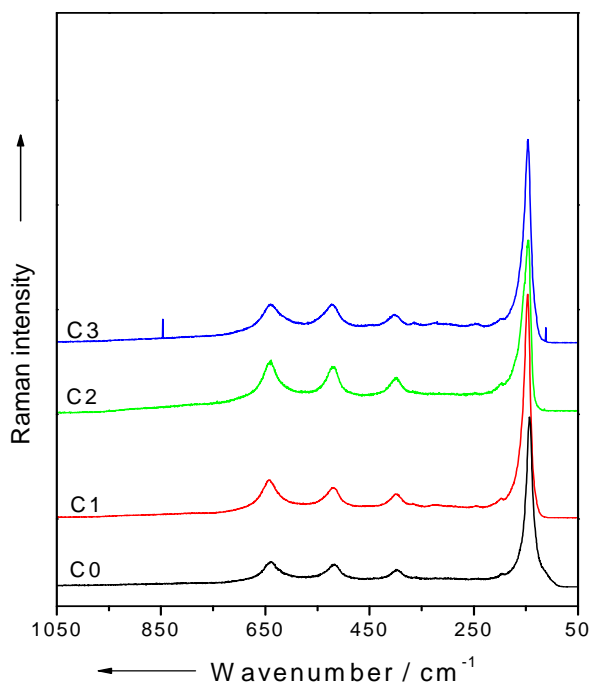
Figure 1. Selected SEM images obtained from the highly porous composites as indicated. Note that the bar scale for the presented images is different.

After analyzing the images it is clear that all the nanocomposites have a porous structure. By comparing the SEM images of the standard TiO_2 aerogel with the ones of the new nanocomposites **C2** and **C3** one can observe that the porosity is quite similar, however, a slow diminution of the porosity occurs for the composites in comparison with the unloaded TiO_2 aerogel, most probably as a cause of the gold nanoparticle presence.

In order to establish the potential of using these porous materials for water purifying processes such as photocatalysis, the specific surface area of the pores was determined. The results obtained from BET analysis are shown in Table 1. We can observe that only the value of the **C3** composite is similar to that obtained for the standard aerogel sample. The highest recorded value was for sample **C2** ($160 \text{ m}^2 \cdot \text{g}^{-1}$) and the lowest one for sample **C1** ($93 \text{ m}^2 \cdot \text{g}^{-1}$). What is remarkable is the fact that some of the peak values of the nanocomposites exceed the one of the standard TiO_2 aerogel, creating the perspectives for an improved photocatalytic response.

Table 1.BET specific surface areas of the standard TiO₂ aerogel and the ones of the composites.

Sample	Specific surface area (m ² ·g ⁻¹)
C0	121
C1	93
C2	160
C3	125

**Figure 2.** The Raman spectra of the highly porous composites as indicated.

For the purpose of analyzing these samples structurally, Raman spectroscopy was used. Raman spectra of the investigated samples are present in Fig. 2 and show well defined peaks around 144 (E_g), 197 (E_g), 399 (B_{1g}), 517 ($A_{1g} + B_{1g}$) and 639 cm^{-1} (E_g), which correspond to the vibrational modes of TiO₂ anatase phase [11]. To point out the possible structural modifications, which might occur due to the presence of the Au colloidal nanoparticles in the TiO₂ structures, a more precise analysis of the Raman spectra was performed, namely analyzing the spectral parameters *i.e.* the band position and its full width at half maximum (FWHM) for

the band located around 144 cm^{-1} , knowing the fact that this band is most sensitive to the structural changes that occur in the TiO_2 network, when nanocrystallites of several nanometers build up the structure [9,12-14].

By looking at the data presented in Table 2 one can observe that the FWHM of the band is a much more sensitive parameter than its position. One important aspect must be mentioned. Although these differences between the values of the Raman band widths are small, they are very meaningful because of the high spectral resolution used for recording these spectra (1 cm^{-1}).

Table 2.

Spectral parameters, FWHM and position of the Raman band located around 144 cm^{-1} .

Sample	FWHM [cm^{-1}]	Band position [cm^{-1}]	Mean crystallite size [nm]
C0	14.34	144.8	9.7
C1	12.85	144.1	11.7
C2	15.03	145.1	9.0
C3	16.39	145.7	8

The spectral changes can be discussed in terms of finite-size effect of nanocrystallinity [9,12-14]. For a nanocrystal of size L , the "infinite-crystal" k space selection rule is replaced by a relaxed version characterized by a k space uncertainty of order $(1/L)$, k representing the phonon wave vector. In this case, all of the phonon branch modes, from $k = 0$ to $k = (1/L)$ are Raman active. Having in view that the phonon dispersion curve $v(k)$ is not flat, the recorded band shifts and widths follow the next rule: the smaller L is, the larger the shift and the width of the band are. An experimental correlation between the crystallites size L , as determined by XRD, and the FWHM of the 144 cm^{-1} Raman band obtained from the composites is presented in Fig. 3. In order to avoid the eventual spectroscopic errors that could appear in the FWHM analysis procedure, repeated measurements of the samples have been performed. The theoretical expression that could be used to fit this experimental data is: $\text{FWHM} = \text{FWHM}_0 + k_1(1/L^\alpha)$, where FWHM is the width of the band under investigation, and $\text{FWHM}_0 = 7.80963 \pm 0.18605$ and $k_1 = 147.10595 \pm 3.29669$ are parameters resulting from the fit [12,13]. FWHM_0 is the intrinsic band width and $\alpha = 1.3716 \pm 0.0215$ is an empirical Raman-versus-size scaling exponent that was related to the network structure [12,13]. By taking into account the results obtained from the XRD and Raman data correlation, the finding of the crystallites mean size by simply measuring a Raman spectrum becomes achievable (see Fig. 3).

The X-ray diffractograms recorded on the prepared composites are presented in Fig. 4 and exhibit strong diffraction peaks at 25.16° , 37.56° , 47.92° , 54.8° and 62.44° that prove the formation of a TiO_2 anatase crystalline network. By looking at the shape of the peaks one can see that the presence of the Au nanoparticles inside the porous network influences the dimensions of the TiO_2

crystallites. For example, the peaks at 25° and 48°, from **C2** and **C3**, diffractograms are broader than those of **C0** and **C1**, meaning that the sizes of the crystallites from **C2** and **C3** are smaller.

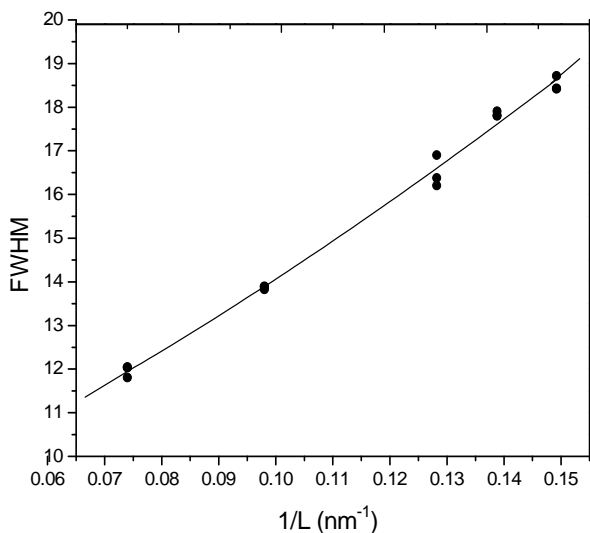


Figure 3. Correlations between the crystallite size (L) determined from the XRD and the FWHM of the 144 cm⁻¹ band (Γ) derived from the Raman spectra analysis of the composites.

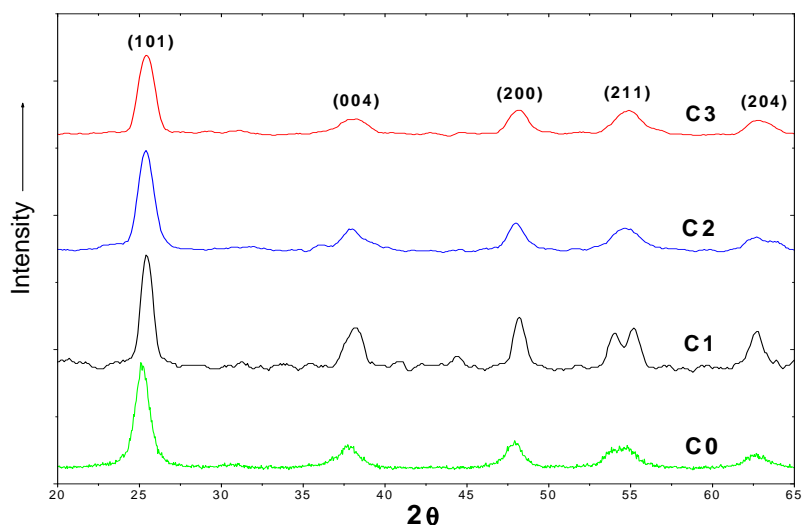


Figure 4. X-ray diffractograms of the highly porous composites as indicated.

To confirm the information obtained concerning the dimension of the crystallites forming the sample structures and to complete them with new data, a series of TEM images were obtained and are illustrated in Fig. 5. From the TEM images one could observe the presence of the Au nanoparticles (arrow **C3**). The size distributions of the TiO_2 particles from all samples are shown in Fig. 6. The maximum size value of the TiO_2 crystallites derived from TEM images is close to the one determined by Raman spectroscopy, approximately 10 nm. By comparing the size values of the crystallites of the TiO_2 standard aerogel, **C0**, with the ones of the nanocomposites one can see that for **C2** and **C3** they are barely smaller, while for **C1** a value almost similar was obtained (see Fig. 6). This comes to confirm the observations derived from the X-ray diffractogram analysis. The sizes of the TiO_2 nanocrystallites obtained by TEM analysis are promising if we take into consideration that the maximum photocatalytic response reported up to now for TiO_2 non-porous structures has been obtained for nanostructures of approximately 10 nm [15].

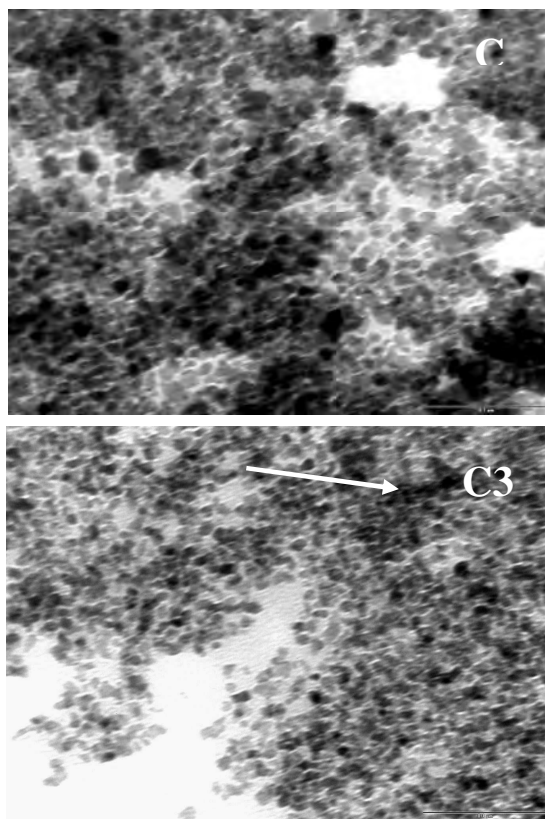


Figure 5. Selected TEM images of the highly porous composites as indicated.

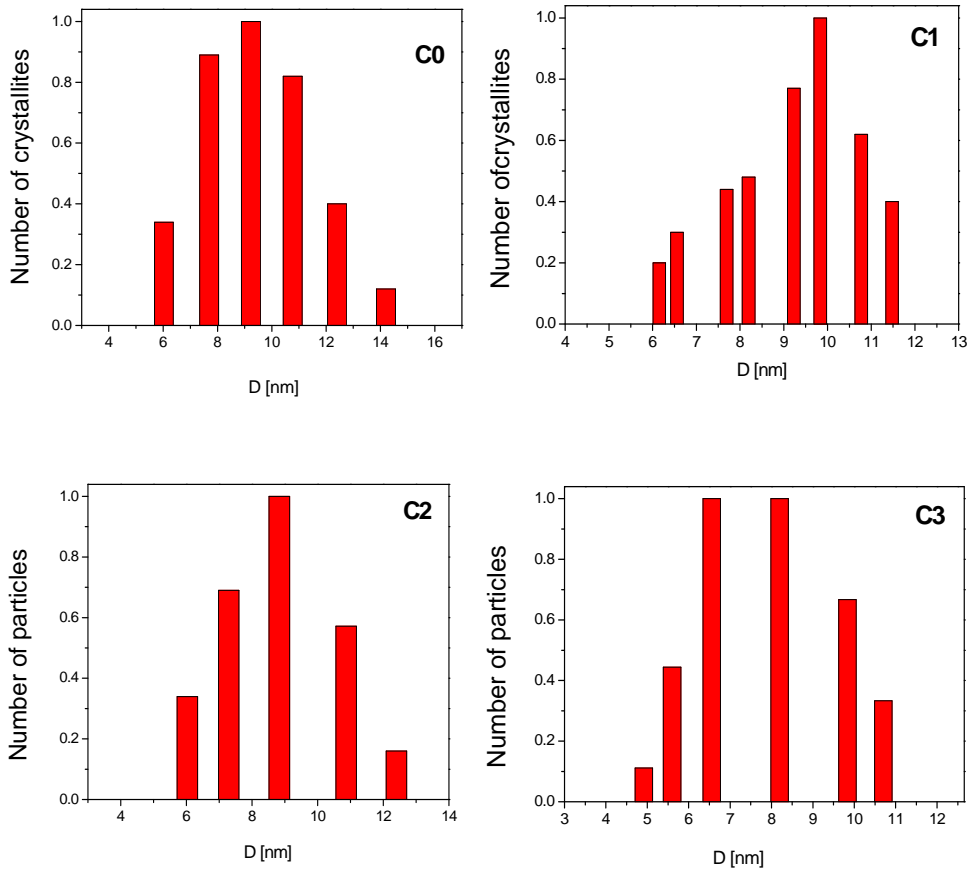


Figure 6. Size distributions of the TiO₂ anatase crystallites derived from TEM analysis of the highly porous composites as indicated

4. Conclusions

Alongside the TiO₂ aerogel with high porosity, there have been successfully obtained nanocomposites based on TiO₂ aerogel and Au colloidal nanoparticles through different synthesis methods. The samples have been heat treated at 500 °C for two hours in order to obtain the desired TiO₂ anatase phase and then, they were analyzed structurally and morphologically.

The porosity of all the nanocomposites has been observed by SEM and the quantitative values of the specific surface areas of the pores have been determined by N₂ adsorption method. The maximum specific surface area was obtained for nanocomposite **C2** (160 m²·g⁻¹). The values determined for this sample are higher

than that of the standard TiO₂ aerogel 121 (m²·g⁻¹). This result is very promising for photocatalytic testing knowing that the anatase crystalline phase, which builds up the structure of this sample, enhances the photocatalytic activity. The mean size of the anatase nanocrystals, approximately 10 nm, has been determined from the Raman-XRD data correlation for all of the investigated samples. The values were confirmed by TEM measurements, however one can see that for the nanocomposites **C2** and **C3** they are barely smaller, while for **C1** a value almost similar with that from **C0** was observed. These results confirm that the sizes of the TiO₂ crystallites have been influenced by the presence of the Au nanoparticles in the samples. Since the maximum photocatalytic activity related in the literature was determined for TiO₂ structures of approximately 10 nm, the synthesized composites could be considered as real candidates for obtaining efficient photocatalysis.

REFERENCES

1. N. Hüsing, U. Schubert, *Angew. Chem. Int. Ed.* **37** (1998) 22.
2. G. Dagan, M. Tomkiewicz, *J. Phys. Chem.* **97** (49) (1993) 12651.
3. M. Ciszowska, M. Tomkiewicz, *Curr. Top. Electrochem.* **8** (2001) 1.
4. W.Y. Lin, C. Wei, K. Rajiेशwar, *J. Electrochem. Soc.* **9** (1993) 2477.
5. S. Chen, R. S. Ingram, M. J. Hostetler, J. J. Pietron, R. W. Murray, T. G. Schaaff, J. T. Khoury, M. M. Alvarez, R. L. Whetten, *Science* **280** (1998) 2098.
6. A. Dawson, P. V. Kamat, *J. Phys. Chem. B* **105**, 2001, 960.
7. P. V. Kamat, *J. Phys. Chem. B* **106**(32) (2002) 7729.
8. V. Subramanian, E. E. Wolf, P. V. Kamat, *Langmuir* **19** (2003) 469.
9. L. Baia, A. Peter, V. Cosoveanu, E. Indrea, M. Baia, J. Popp, V. Danciu, *Thin Solid Films* **511-512** (2006) 512.
10. M. Baia, F. Toderas, L. Baia, S. Astilean, Book of Abstracts of the *International Conference EnvEdu 2006*, Brasov, pg. 57.
11. H. C. Choi, Y. M. Jung, S.B. Kim, *Vib. Spectrosc.* **37** (2005) 33.
12. S. Kelly, F. H. Pollak, M. Tomkiewicz, *J. Phys. Chem. B* **101** (1997) 2730.
13. C. J. Doss, R. Zallen, *Phys. Rev. B* **48** (1993) 15626.
14. L. Baia, M. Baia, A. Peter, V. Cosoveanu, V. Danciu, *J. Opto. & Adv. Mater.* **9** (2007) 668.
15. D. Beydoun, R. Amal, G. Low, S. McEvoy, *J. Nanopart. Res.* **1** (1999) 439.

EPR SPECTROSCOPY APPLIED TO THE STUDY OF ANCIENT CERAMICS: PRELIMINARY RESULTS FOR BRONZE AGE POTTERY FROM ILISUA

C. IONESCU¹, L. GHERGARI¹, V. SIMON²

ABSTRACT. Ceramic pottery fragments of Ilișua archaeological site were studied by Electron Paramagnetic Resonance (EPR). The Fe³⁺ EPR spectra evidence the disposal of ferric ions in different environments depending on their thermal history. The firing temperatures of the raw clays used in manufacturing of the investigated ceramic samples were compared based on the relative intensity of the resonance lines.

Keywords: *EPR; ancient ceramics.*

Introduction

Since 1960's, the Electron Paramagnetic Resonance (EPR) has been successfully applied for post-accident dose reconstruction in the environment [1], investigation of human tissues [2, 3] or other various substances including geological systems[4-8]. Apart of dating of stalactites [9], or sediments [10] a number of other geological materials, e.g. cherts [11], volcanics [12, 13], clays [14-16], travertines [17] and some minerals [18, 19] were also subjected to EPR studies.

Moreover, the EPR is widely used in archaeometry, for tooth enamel and bones dating [20-24], for the study of mosaic glasses [25], organic food remnants [26] and other compounds [27]. For ceramics, the EPR application regards mainly dating as well as information on firing temperature and atmosphere [28-31]. The ceramics is suited for EPR studies because it is made of natural clays containing iron. However, whether upon firing iron occurs as "free" oxides, ferric or ferrous ions trapped inside glass or crystalline firing phases, or adsorbed on the surface of phyllosilicates remains unknown.

The aim of this paper is to present preliminary EPR results on ceramic pottery fragments of Ilișua archaeological site and to compare with the previous results obtained by optical microscopy and Electron Microprobe analyses on same shards.

Samples and method

The Ilișua archaeological site is located in the northern part of the Transylvanian Basin, in Romania, on a high terrace of the Someșu Mare River near the confluence

¹ Department of Geology, „Babes-Bolyai” University, 1 Kogalniceanu Str., RO-400084 Cluj-Napoca, Romania

² Department of Physics & Institute of Interdisciplinary Research in Bio-Nano-Sciences, „Babes-Bolyai” University, 1 Kogalniceanu Str., RO-400084 Cluj-Napoca, Romania

with the Şieu River [32]. Beneath the remains of a Roman *castrum* [33], cremation tombs containing bronze artefacts and shards of ceramic bowls, cups, plates, small vessels were found. These were assigned to the so-called Late Bronze Age “Noua” Culture, dated between 1400-1200 B.C. [34].

Fragments of ceramic pottery, labelled B2, B4, B6, B7, B8 and B11, were provided by Bistrița-Năsăud County Museum (Romania) for mineralogical and physical studies. The ceramic samples show a brown to greyish-brown body-colour and a relatively homogeneous appearance, with visible pores and shrinkage cracks.

The EPR measurements were performed at room temperature on powdered samples of same mass, at room temperature, in X band (9.4 GHz), with 4 G modulation amplitude, on an ADANI spectrometer.

Results and discussion

The EPR spectra (Fig. 1) are dominated by a large, relatively symmetric resonance line with $g_{\text{eff}} \approx 2.1$. No narrow signal can be observed close to $g_{\text{eff}} = 2$, that usually arises in clays from paramagnetic centers due to the natural radiation which induces the formation of radicals of trapped electrons and holes [35]. Such irradiation induced defects disappear when the calcination temperature increases, i.e. they are thermally removed [36]. Their lacking in the EPR spectra suggests firing temperature above 800 °C for the ceramic sample [29, 31]. This is in good agreement with the Electron Microprobe data based on mineral chemistry, which assume a firing temperature between 850-950 °C for the Ilisua ceramic samples [32].

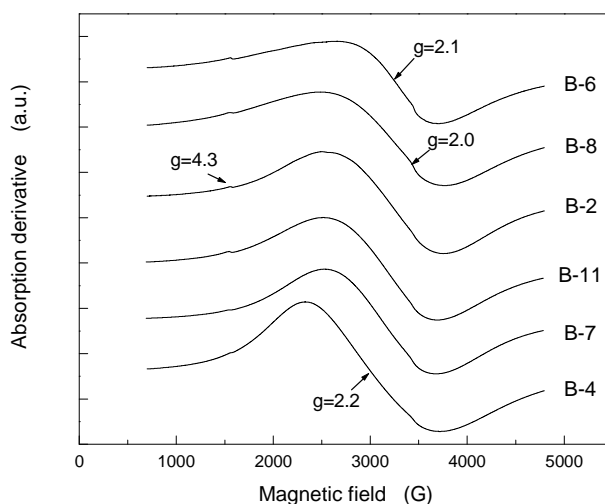


Fig. 1. The room temperature EPR spectra of ceramic samples.

A weak resonance signal occurs at $g_{\text{eff}} \approx 4.3$ and is assigned to Fe^{3+} ions in sites of tetrahedral or rhombohedral symmetry, characterized by high crystal fields. As this resonance line is typical for Fe^{3+} ions trapped in glasses [37], its intensity might be a rough measure of the quantity of the glass phase present in the ceramics and implicitly a qualitative estimation of the firing temperature. The intensity of this signal is better evidenced in Fig. 2. According to the intensity of these resonance signals, the highest firing temperature was applied to sample B6 and the lowest to samples B7 and B4.

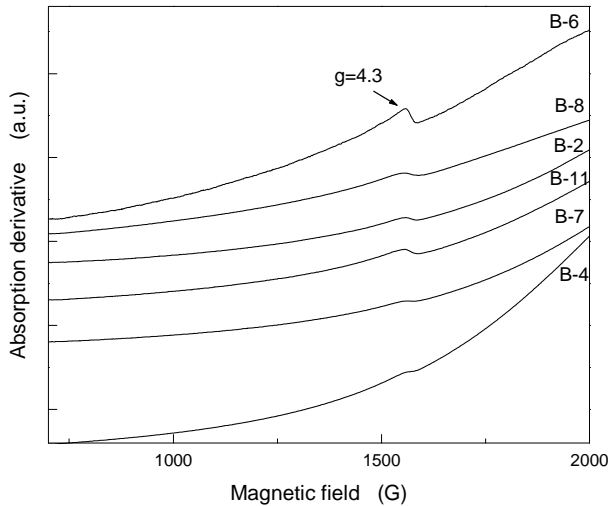


Fig. 2. Detailed EPR spectra of ceramic samples in the low magnetic field region.

The large and symmetric resonance line with $g_{\text{eff}} \approx 2.1$ is assigned to Fe^{3+} ions in sites of octahedral symmetry, with low crystal fields, and is specific to disordered oxide systems with high Fe_2O_3 content wherein most probably hematite and/or magnetite particles occur [38, 39]. In thin sections, hematite, Ti-magnetite and Fe_2O_3 -bearing ilmenite were identified [32]. The resonance line at $g_{\text{eff}} \approx 2.1$ is shifted to lower values of the magnetic field, up to $g_{\text{eff}} \approx 2.2$, in following order: B6, B8, B2, B11, B7 and B4 (Figs. 1 and 2). These results can be assigned to the development of ferromagnetic multi-domain particles in the ceramics samples. The width of $g_{\text{eff}} \approx 2.1$ line increases in the same order of samples and suggests a wide range of ferromagnetic particles size. Conversion of Fe^{3+} ions into Fe^{2+} ions could also contribute to the observed evolution of the Fe^{3+} EPR intensity. The lowest intensity of the EPR signal is recorded for the B6 sample, showing lowest Fe^{3+} content.

It has to be noticed that the EPR spectra of the samples B-6 and B-8 are quite similar and differ from the other ones. Whereas the EPR spectra for the latter are rather symmetric, those of the B6 and B8 samples are more asymmetric, indicating a shape of the magnetic domains far from ideal sphere. Even though at such Fe_3O_3 concentrations a line narrowing, due to super-exchange interactions, is expected, this narrowing is not observed. It might be presumed that any narrowing in some clusters is masked by the dipolar broadening or by the structural disorder in the iron rich phases.

Conversion of Fe^{3+} ions into Fe^{2+} ions could also contribute to the observed evolution of the Fe^{3+} EPR intensity, that can be exploited for the investigation of firing temperature. The lower intensity of the EPR signal recorded for the B-6 sample (Fig. 1) shows that the Fe^{3+} content in this ceramic is lower than in the other ones, probably due to higher firing temperature.

Conclusions

The EPR results on pottery fragments of Ilişua archaeological site show that the iron present in clays which are now thermally transformed is located in two types of sites. The resonance lines at $g_{\text{eff}} \approx 4.3$ and 2.1 might be assigned to the Fe^{3+} ions in sites of low symmetry characterized by high crystal fields, and to the Fe^{3+} ions in sites of octahedral symmetry, with low crystal fields, respectively. The relative firing temperature was comparatively estimated based on the relative intensity of the resonance absorption lines. These indicate the highest temperature for the sample labelled B-6. The lack from the RPR spectra of the radiation-induced defects suggests firing temperature above 800-850 °C for all investigated samples. This is consistent with the mineral chemistry based on electron microprobe data [32] which assumed a firing temperature between 850-950 °C for the Ilişua ceramic samples.

ACKNOWLEDGEMENTS

The study was financially supported by CNCSIS-UEFISCSU, PNII-IDEI-2241/2008 Project (Romania).

REFERENCES

1. W.L. McLaughlin, *Radiat. Prot. Dosim.* 47 (1993) 255.
2. D. Regulla, V. Deffner, *Appl. Radiat. Isotopes*, 33 (1982) 1101.
3. D. Regulla, *Appl. Radiat. Isotopes*, 52 (2000) 1023.
4. I. Ardelean, M. Peteanu, E. Burzo, F. Ciorcas, S. Filip, *Solid State Commun.*, 98 (1996) 351.
5. I. Ardelean, M. Peteanu, S. Filip, V. Simon, I. Todor, *Solid State Commun.*, 105 (1998) 339.

6. I. Taoufik, M. Haddad, A. Nadiri, R. Brochu, R. Berger, *J. Phy. Chem. Solids*, 60 (1999) 701.
7. T. Ehara, T. Ikoma, S. Tero-Kubota, *J. Non-Cryst. Solids* 266-269 (2000) 540.
8. B. Engin, H. Demirtaş, *Radiat. Phys. Chem.*, 71 (2004) 1113.
9. M. Ikeya, *Nature*, 255 (1975) 48-50.
10. D. Hoffmann, C. Woda, C. Strobl, A. Mangini, *Quaternary Sci. Rev.*, 20 (2001) 1009.
11. E.G. Garrison, R.W. Rowlett, D.L. Cowan, L.V. Holroyd, *Nature*, 290 (1981) 44.
12. M. Imai, K. Shimokawa, M. Hirota, *Nature*, 314 (1985) 81.
13. D. Miallier, J. Fain, S. Sanzelle, Th. Pilleyre, M. Montret, A. Soumana, C. Falguères, *Radiat. Meas.*, 23 (1994) 399.
14. A.M. Hirt, A. Banin, A.U. Gehring, *Geophys. J. Int.*, 93 (1993) 1161.
15. E. Balan, T. Allard, B. Boizot, G. Morin, J.-P. Muller, *Clay Clay Miner.*, 48 (2000) 439.
16. J. Babińska, K. Dyrek, P. Wyszomirski, *Miner. Polonica*, 38 (2007) 125.
17. B. Engin, O. Güven, F. Köksal, *Applied Radiat. Isotopes*, 51 (1999) 729.
18. R.G. Lyons, *Applied Radiat. Isotopes*, 47 (1996) 1385.
19. J.C.R. Mittani, S. Watanabe, J.F.D. Chubaci, M. Matsuoka, D.L. Baptista, F.C. Zawislak, *Nucl. Instrum. Meth. B*, 191 (2002) 281.
20. R. Grün, *Evol. Anthropol.*, 2 (1993) 172.
21. R. Debuyst, F. Callens, M. Frechen, F. Dejehet, *Appl. Radiat. Isotopes*, 52 (2000) 1327.
22. R.B. Hayes, E.H. Haskell, *Radiat. Meas.*, 32 (2000) 781.
23. A.R. Skinner, B.A.B. Blackwell, N.D. Chasteen, J. Shao, S.S. Min, *Appl. Radiat. Isotopes*, 52 (2000) 1337.
24. F. Callens, G. Vanhaelewyn, P. Matthys, *Spectrochim. Acta*, A 58 (2002) 1321.
25. C.B. Azzoni, D. Di Martino, C. Chiavari, M. Martini, E. Sibilina, M. Vandini, *Archaeometry*, 44 (2002) 543.
26. M.R. Schurr, R. Hayes, L.L. Bush, *Archaeometry*, 43 (2001) 407.
27. W.J. Rink, *Radiat. Meas.*, 27 (1997) 975.
28. Y. Matsuoka, M. Ikeya, *Jpn. J. Appl. Phys.*, 34 (1995) 6068.
29. G. Gualtieri, S. Del Monaco, *Res. Chem. Intermediat.*, 22 (1996) 435.
30. Y. Bensimon, B. Deroide, M. Martineau, J.V. Zanchetta, *C R Acad Sci IIC*, 2 (1999) 119.
31. Y. Bensimon, B. Deroide, J.V. Zanchetta, *J. Phys. Chem. Solids*, 60 (1999) 813.
32. C. Ionescu, V. Hoeck, L. Ghergari, *Appl. Clay Sci.*, Sp. Iss. *Clays in archaeology* (in press).
33. D. Protase, C. Gaiu, G. Marinescu, *Revista Bistriței*, X–XI (1997) 27.
34. C. Gaiu, *unpublished data*.
35. R. Allard, J.P. Muller, J.C. Dran, M.T. Menager, *Phys. Chem. Miner.*, 21 (1994) 85.
36. J.M. Gaite, P. Ermakoff, J.P. Muller, *Phys. Chem. Miner.*, 20 (1993) 242.
37. D.L. Griscom, Electron Spin resonance, in *Glass Science and Technology*. Pp. 151 in: *Advances in Structural Analysis* (D.R. Uhlman and N.J. Kreidl, editors), 4B, Academic Press, Inc., 1990.
38. D.L. Griscom, *J. Non-Cryst. Solids*, 67 (1984) 81.
39. R. Simon, R. Pop, V. Simon, M. Coldea, *J. Non-Cryst. Solids*, 331 (2003) 1.

DIRECT DETERMINATION OF NATURAL AND SYNTHETIC ANTIOXIDANTS IN COSMETIC CREAMS BY GAS CHROMATOGRAPHY

JUNCAN ANCA MARIA¹, LUNG CLAUDIU², HORGA CRISTINA ELENA³

ABSTRACT. A gas chromatographic method for the simultaneous determination of two additives in o/w cosmetic formulations was developed by using GC and FID detection. A simple dilution procedure of the sample was required. The separation obtained for the two antioxidants was good under the chromatographic conditions used. Their analysis was carried out in commercial samples, and satisfactory results were obtained for the recovery of this compounds.

Keywords: *cosmetic product, antioxidants, antiradical activity, chromatographic anlysis methods, gas chromatography.*

INTRODUCTION

Cosmetological research has increasingly focused on the processes leading to the formation of the anatomical-functional damage of the skin, identified with ageing. Great interest in this topic has been generated by the study of substances able to prevent cutaneous damage by free radicals: this substances are termed as antioxidants [1].

Cosmetics are commercially available products, that are used to improve the appearance of the skin. The consumer demand for more effective products, that substantively beautify the appearance of the skin, has resulted in increased science research and product development in the cosmetics industry [2]. There are considerable data to suggest the benefits of such ingredients in cosmetics [3]. In recent years, the cosmetics market has been enriched by numerous skin care products acompanied by advertising claims centred on their antioxidant activity. These products, containing substances with antiradical activity, were created mainly to satisfy expectations of treatment, and prevention of photo-aging [4].

Studies in this area, indicate a main association between a potential health hazard and ingestion, and the use of antioxidants in cosmetic products. That why, it is necessary to establish new efficient analysis methods, for monitoring the use of this

¹ “Babeş-Bolyai” University, Faculty of Chemistry and Chemical Engineering, Arany Janos Str. 11, 400028, Cluj-Napoca, Romania.

² “Babeş-Bolyai” University, Faculty of Physics, Mihail Kogalniceanu Str. 1, 400084, Cluj-Napoca, Romania.

³ Institute of Public Health, Louis Pasteur Str. 6, 400349, Cluj-Napoca, Romania.

controversal antioxidants in a adequate mode, and for the determination, and for the admissibility limit control of antioxidants permitted, and used in the cosmetic industry.

EXPERIMENTAL

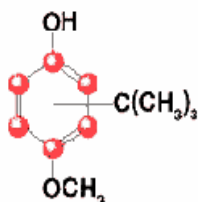
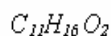
Standards and Reagents

All reagents used were of analytical grade and used without further purification. Commercially available antioxidants used in the study are listed in Table 1 [5]:

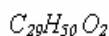
Table 1.

List of Antioxidants and Preservative Studied		
<i>Chemical Name</i>	<i>Abbreviation</i>	<i>Supplier</i>
3-tert-butyl-4-hydroxy anisole	BHA	JAN DEKKER Nederland B.V.
Tocopheryl Acetate	α -TA	BASF

Commercial cosmetics were purchased from a local cosmetic manufacturer. The chemical structure of the two antioxidants are given in Figure 1:



Butylated Hydroxyanisole (BHA)



Mixture of alpha, beta, gamma and delta tocopherol

Figure 1. Structure of BHA and α -TA

Multiple studies have been performed on both tocopherol and its acetyl ester derivate, tocopherol acetate. While tocopherol is the primary active form of vitamin E, the vitamin E esters have also been shown to penetrate the epidermis when applied topically [2]. The vitamin E isomers are usually esterified to acetates for use in commercial vitamins and topical formulations because the esters are far more stable [6].

GC Conditions

Chromatography was performed on a Shimadzu 2010 Model gas chromatograph equipped with a FID detector.

Fused silica capillary column DB-5, 30m x 0,25 mm ID, with a stationary phase thickness of 0,25 μm film thickness was used [7]. The oven temperature was held at 120°C for five minutes, then increased at a rate of 10°C/min to 310°C and held for 10 minutes. Detector conditions were 320 °C, N₂ 30 ml/min and H₂-40 ml/min flow-rate. The injection temperature was 280°C. 1 μl aliquots of the standard and sample solutions were analyzed under the operation conditions described above.

Calibration Standard Solutions

Stock solutions were prepared by dissolving the appropriate amounts of the standard antioxidants in a solvent consisting of acetonitrile and MeOH in the ratio 7:3. A set of working solutions was prepared by deluting aliquots of the stock solution to give concentrations ranging from 150 to 1000 $\mu\text{g}/\text{mL}$ for the studied compounds.

Sample Preparation

Three oil-rich products (Anti-Wrinkle Eye Contour Cream, Intensive Moisturizing Day Lift Cream and a Replenishing Night Lift Cream) were analyzed by the following procedure: about 0,5 g of each o/w emulsions was dissolved by sonication with 25 mL of a mixture of methanol:acetonitrile (1:1 v/v). After approx. 5 min. centrifugation, the supernatant was filtered through a 0,45 μm filter (Chromafil PET-45/25, 0,45 μm , Macherey-Nagel GmbH&CO. KG.).

RESULTS AND DISCUSSION

Three standard solutions of the two antioxidants were injected to determine the individual retention times of the synthetic and natural antioxidants.

Figure 2 shows the chromatogram of a standard solution of the two antioxidants studied at the concentration of 150 $\mu\text{g}/\text{mL}$ BHA and 250 $\mu\text{g}/\text{mL}$ α -TA respectively. BHA presented a retention time at 10.086 min. and α -TA at 26.020 min.

Figure 3 shows the chromatogram of a standard solution of the two antioxidants studied at the concentration of 250 $\mu\text{g}/\text{mL}$ BHA and 500 $\mu\text{g}/\text{mL}$ α -TA respectively. BHA presented a retention time at 10.100 min. and α -TA at 26.043 min.

Figure 4 shows the chromatogram of a standard solution of the two antioxidants studied at the concentration of 500 $\mu\text{g}/\text{mL}$ BHA and 1000 $\mu\text{g}/\text{mL}$ α -TA respectively. BHA presented a retention time at 10.118 min. and α -TA at 26.074 min.

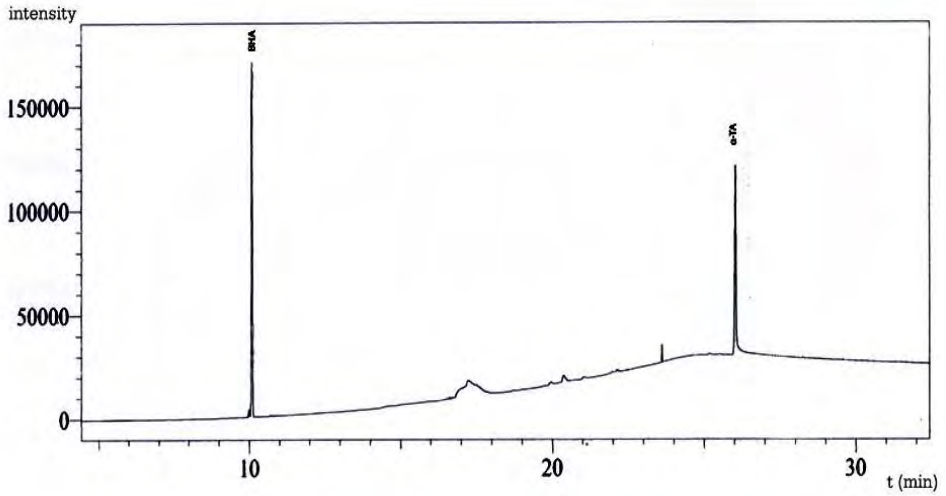


Figure 2. Chromatogram of a BHA (250 $\mu\text{g/mL}$) and α -TA (500 $\mu\text{g/mL}$) Standard

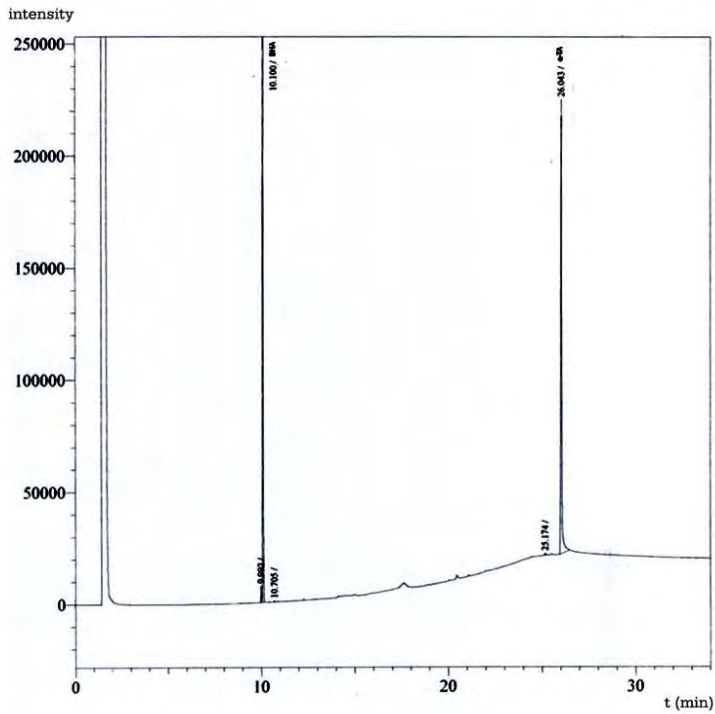


Figure 3. Chromatogram of a BHA (500 $\mu\text{g/mL}$) and α -TA (1000 $\mu\text{g/mL}$) Standard

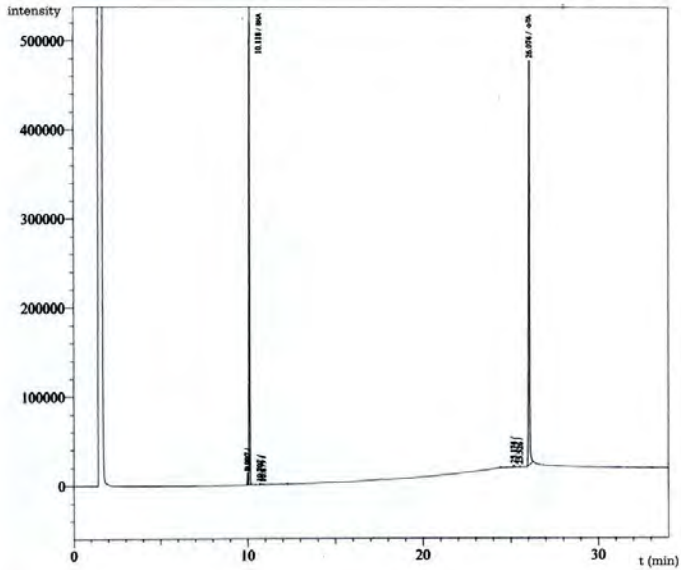


Figure 4. Chromatogram of a BHA (100 $\mu\text{g/mL}$) and α -TA (1000 $\mu\text{g/mL}$) Standard

The calibration graphs for BHA and α -TA were constructed over the covered range of concentration, as indicated in the experimental part and are presented in Figure 5.:

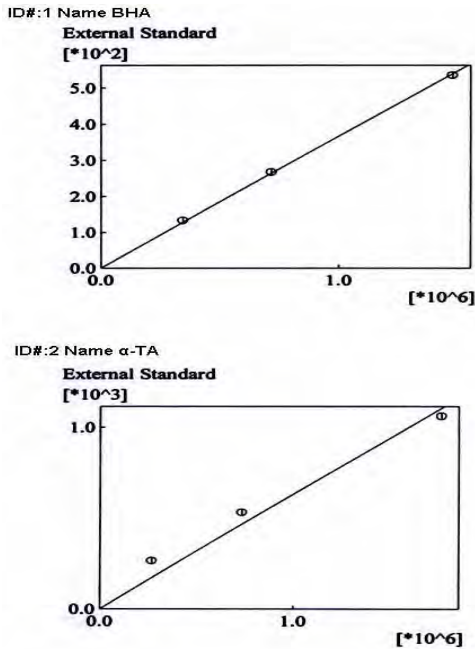


Figure 5. Calibration Graphs for BHA and α -TA

Three commercial samples that contained combinations of the antioxidants were identified by comparing the retention times of the peaks observed, with those obtained from the standard solutions.

The chromatograms of a Anti-Wrinkle Eye Contour Cream, a Intensive Moisturizing Day Lift Cream, and a Replenishing Night Lift Cream are presented in Figure 6, Figure 7, and respectively Figure 8.

The chosen elution conditions described below allowed a good separation of the two compounds taken into account. For the first commercial product that was analyzed by the purpose of the belowed described- a Anti-Wrinkle Eye Contour Cream- the obtained retention times of the two studied antioxidants were $T_{R \text{ BHA}} = 10.081$ min and $T_{R \alpha\text{-TA}} = 26,013$. For the second commercial product that was analyzed by the purpose of the belowed described- a Intensive Moisturizing Day Lift Cream- the obtained retention times of the two studied antioxidants were $T_{R \text{ BHA}} = 10.090$ min and $T_{R \alpha\text{-TA}} = 26,040$. For the third second commercial product that was analyzed by the purpose of the belowed described- a Replenishing Night Lift Cream- the obtained retention times of the two studied antioxidants were $T_{R \text{ BHA}} = 10.093$ min and $T_{R \alpha\text{-TA}} = 26,042$.

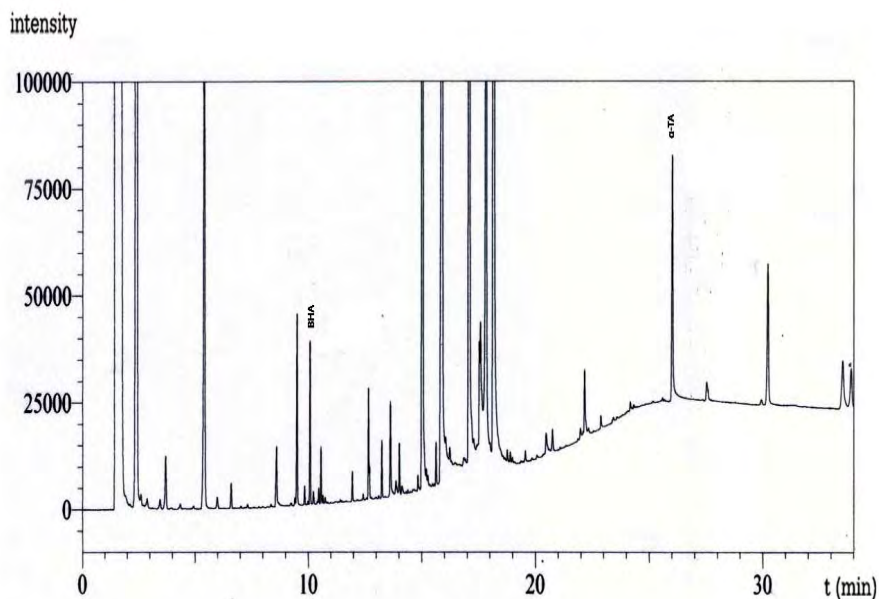


Figure 6. Chromatogram for Anti-Wrinkle Eye Contour Cream

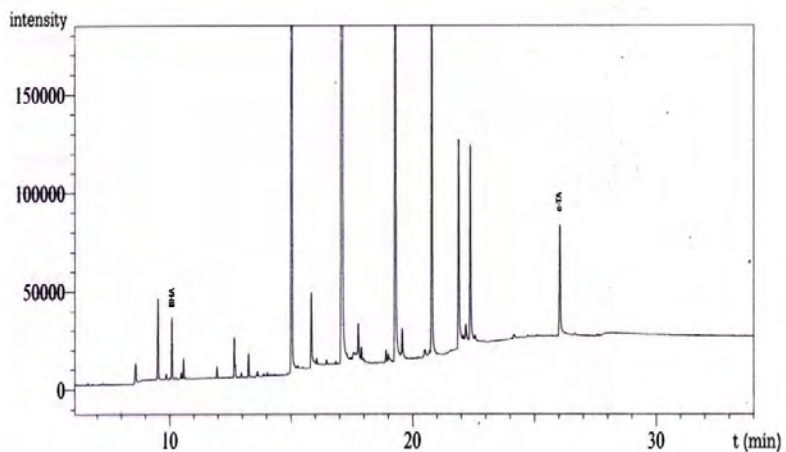


Figure 7. Chromatogram for Intensive Moisturizing Day Lift Cream

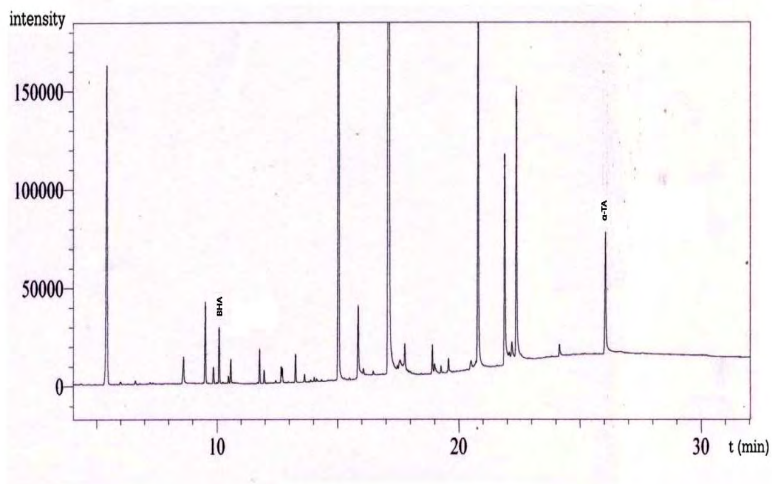


Figure 8. Chromatogram for a Replenishing Night Lift Cream

The centralized R_F values determined for the two analyzed antioxidants in three standard solutions and three cosmetic formulations are listed in Table 2.a, and Table 2.b respectively:

Table 2.a.

R_F values for BHA in the analyzed samples

Sample	R_F Value
Standard Slution	
<i>BHA (250 $\mu\text{g/mL}$) and α-TA (500 $\mu\text{g/mL}$) Standard</i>	10.086
<i>BHA (500 $\mu\text{g/mL}$) and α-TA (1000 $\mu\text{g/mL}$) Standard</i>	10.100
<i>BHA (100 $\mu\text{g/mL}$) and α-TA (1000 $\mu\text{g/mL}$) Standard</i>	10.118
Cosmetic Creams	
<i>Anti-Wrinkle Eye Contour Cream</i>	10.81
<i>Intensive Moisturizing Day Lift Cream</i>	10.09
<i>Replenishing Night Lift Cream</i>	10.093

Table 2.b.

R_F values for α -TA in the analyzed samples

Sample	R_F Value
Standard Slution	
<i>BHA (250 $\mu\text{g/mL}$) and α-TA (500 $\mu\text{g/mL}$) Standard</i>	26.020
<i>BHA (500 $\mu\text{g/mL}$) and α-TA (1000 $\mu\text{g/mL}$) Standard</i>	26.043
<i>BHA (100 $\mu\text{g/mL}$) and α-TA (1000 $\mu\text{g/mL}$) Standard</i>	26.074
Cosmetic Creams	
<i>Anti-Wrinkle Eye Contour Cream</i>	26.013
<i>Intensive Moisturizing Day Lift Cream</i>	26.04
<i>Replenishing Night Lift Cream</i>	26.042

It can be realized easily that the determined R_F values are similar in all samples, which demonstrates the determination of the synthetic and natural antioxidants and that the method described above can be successfully applied for the qualitative determination of this compound in cosmetic preparations.

CONCLUSIONS

Cosmetological research has increasingly focused on the processes leading to the formation of the anatomical-functional damage of the skin, identified as aging.

Great interest has been generated by the study of substances able to prevent cutaneous damage by free radicals: these are termed as antioxidants.

Antioxidants are substances, that are added in cosmetic and food products to retard the oxidative degradation processes- rancidity, of those products.

Today there are used more than 15 chemical substances as antioxidants: with a applicability established through normative acts.

Natural antioxidants, specially the *tocopherols* (α -, β -, γ -, δ -tocopherols) are recognized for their large application (by the reason of their antioxidative character and those one of vitamin- tocopherols are forms of vitamin E).

Usually, the most used antioxidants are the synthetic antioxidants, because of their stability, during preparation process.

New products launching for skin and body care at global level, (11.724 products), 11% (almost 1.290 cosmetic products) contain the most used antioxidant in cosmetic products: alpha tocopherol acetate.

Anti-aging products present a real interest, but there are few studies that can be found, regarding the analysis and monitoring methods of antioxidants in such products. That why, it is necessary to establish new efficient analysis methods, for monitoring the use of this controversial antioxidants in a adequate mode, and for the determination, and for the admissibility limit control of antioxidants permitted, and used in the cosmetic industry.

A gas chromatographic method following a simple, rapid dilution with a acetonitrile:methanol and SFE extraction with the same solvent mixture, was used for the determination of BHA and alpha tocopherol acetate in three oil-rich commercially available cosmetic products (Anti-Wrinkle Eye Contour Cream, Intensive Moisturizing Day Lift Cream and a Replenishing Night Lift Cream).

The presence of two antioxidants- synthetic and natural- under the study of three commercially available cosmetic products was determined by using gas chromatography coupled with FID detection. The method allowed a simultaneous, simple, rapid and accurate determination and confirmation of this BHA and α -TA in o/w emulsions, cosmetic products containing many ingredients. The obtained results demonstrate the suitability of the proposed method for analyzing antioxidants in cosmetics with high levels of interference. The simplicity of the procedure described below could make it highly desirable for quality control of antioxidants in cosmetic creams in the cosmetic industry.

The analytical results obtained lead to the conclusion that the developed method can be successfully adopted for an accurate determination of natural and synthetic antioxidants considered in o/w cosmetic formulation and pharmaceutical products.

REFERENCES

1. Tebbe B., *Skin Pharmacol. Appl. Skin Physiol.*, 14, **2001**, 296-302.
2. Lupo M. P., *Clinics in Dermatology*, 19, **2001**, 467-473.
3. Andreassi M., Andreassi L., *J. Cosmetic Dermatol.*, 2, **2004**, 153-160.
4. Cadenas E., Packer L., *Handbook of Antioxidants*, Marcel Dekker Inc., 2nd Edition, **2002**, 1-5.
5. Juncan A., Hodişan T., Horga C. E., Muntean N., Mitan M., *Rom. Soc. Cosmet. Chem.*, **2010**, 10, 2, 8-10 .
6. Burke K. E., *J. Cosm. Dermatol.*, 3, **2004**, 149-155.
7. Jeong H.-J., Lee M.-H., Ro K.-W., Hur C.-W., Kim J.-W., *Int. J. Cosmet. Sci.*, **1999**, 21, 42.

DYNAMICS OF THERMALLY DRIVEN SPRING-BLOCK SYSTEM ON INHOMOGENEOUS SURFACE

ZSOLT I. LÁZÁR¹

ABSTRACT. Using the simple model of two blocks sliding on a flat surface with friction and connected via a spring with stochastic tension, we study by computer simulation the conditions under which the system undergoes an overall drift. We claim that the model bears relevance to the dynamics of dissipative mesoscopic systems in contact with a heat bath with special regard to nanomotors. The study covers the dependence of this drift on parameters such as those describing the nature of the friction including spatial inhomogeneity or those characterizing the stochasticity in the spring force. The algorithm used for integrating the equations of motion is presented in detail together with the results of test setups.

Keywords: spring-block, friction, stochastic spring force, simulation, nanomotor.

1. Introduction

Nanomotors are microscopic (molecular) or mesoscopic systems of nanometer scale that can convert energy into directed motion. They promise breakthroughs in a number of fields including biotechnology and medicine [Khataee10]. Spring-block or stick-slip models are simple physical models with a wide range of applications. Systems described by such models are envisaged as blocks interconnected by springs and sliding with friction on a plane. The model was first used to explain the size distribution of earthquakes [Burridge67]. Since then it has been successfully applied in the study of pattern formation in drying granular materials, magnetization phenomena, self-organizing nanostructures, modelling of high-way traffic, etc. For a comprehensive review the reader may refer to [Néda09].

The general objective of this work is to study using the spring-block model the effect of thermal motion and inhomogeneous environment on the macroscopic scale behavior of simple mesoscopic systems. Under what conditions can one induce controlled behavior in a dissipative mesoscopic system with dynamics fueled exclusively by thermal energy absorbed from the environment? Present paper starts with the description of the model and the investigated features. The internals of the simulation are covered in detail including the validation of the employed algorithms allowing a straightforward reproduction of the reported results by third party researchers. The results are discussed in the last section of this paper.

¹ Chair of Theoretical and Computational Physics, Faculty of Physics, Babes-Bolyai University, Romania

2. The model

System: two point-like blocks with masses m_1 and m_2 are connected by an ideal spring of natural length l_0 and elasticity constant k (see figure 1). The dynamics is one dimensional such that the velocities of the blocks and the change in the length of the spring all occur along the same axis x . The amplitude of the oscillations is small enough so that neither “stiff” collisions nor crossings of the two blocks have to be considered. There is friction between the blocks and the “surface” they slide on.

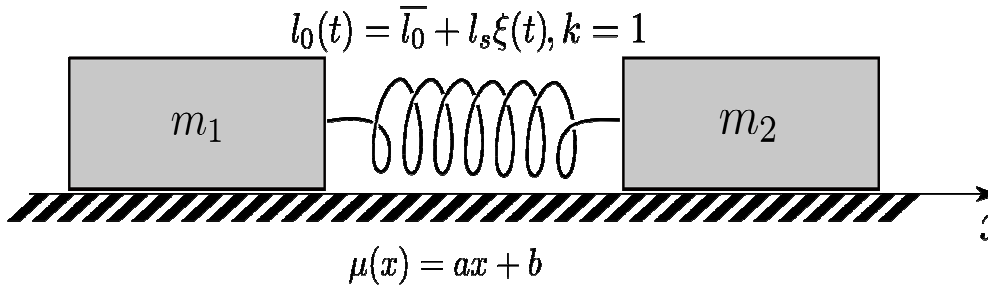


Figure 1. Sketch of the model. Two blocks connected by a spring that has a stochastically varying natural length. The blocks slide on a surface with friction that changes linearly with position. The random variable ξ follows an $N(0, 1)$ type of normal distribution.

Friction: the magnitude of the friction force is a μ value when the block is on the move. When standing it is of the same value as the external (spring-)force up to the same μ threshold value. During motion the direction of this force is opposite to that of the velocity and opposite to the external force when resting.

$$|F_f| = \begin{cases} \mu, & \text{if } |v| \neq 0, \\ \mu, & \text{if } |v| = 0 \text{ and } |f| \geq \mu, \\ |f|, & \text{if } |v| = 0 \text{ and } |f| < \mu \end{cases}, \quad \mu \geq 0.$$

The magnitude of the friction force depends on the position of the block through a $\mu(x)$ type of dependence henceforth referred to as *friction field*.

Thermal contact: for a sustained dynamics the effect of the dissipation has to be balanced by a continuous input of energy. Similarly to the Brownian motion, due to the mesoscopic size of the system any type of thermal contact with a constant temperature heat bath would maintain motion indefinitely. While the actual mechanism of the energy absorption process might be of importance, for this study, the procedure chosen for assuring the energy supply necessary for a sustained dynamics was an

intermittent and stochastic change in the natural length, l_0 , of the spring. The updates in l_0 occur at set time intervals, Δt . Between two updates l_0 is kept constant. The random series of the natural length follows a normal distribution of width l_s centered around \bar{l}_0 . As the distribution is unbounded in both directions the value of the width is limited to low values such that the probability of occurrence of negative l_0 to be negligible.

Studied features: The parameters appearing in the problem are the masses of the blocks, the spring constant k , the \bar{l}_0 and l_s parameters of the spring's natural length distribution, the update time interval Δt , and those characterizing the friction field $\mu(x)$. Since we are free to set the space, time and mass scale we shall consider the blocks having unity mass, while the time and space units will be fixed by setting $k = 1$ and $\bar{l}_0 = 1$.

We are interested in what happens if the blocks have equal masses but the surface they slide on is inhomogeneous, i.e., the friction force has a $\mu(x) = ax + b$ linear dependence on the position. Henceforth we shall refer to a as *friction gradient* and to b as *friction offset*. In addition to the above the integrator algorithm had to be validated by applying it to systems with known behavior.

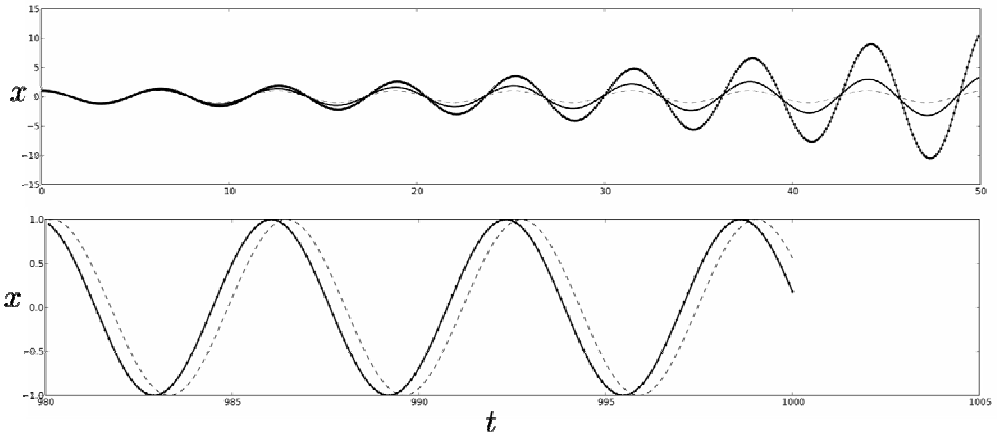


Figure 2. Comparison of different differential equation solvers applied on the harmonic oscillator with unity circular frequency. In the upper frame the dotted and the solid lines are the solutions obtained using the iterative formulas from (1) and (2), respectively. In the lower frame the effect of the Verlet-algorithm - defined by equation (3) - is shown zooming out the last section of a much longer run. The dashed lines represent the exact solutions. The timestep was 0.1 in all cases.

3. The simulation algorithm

The “stick-slip”-like discontinuity in the model of the friction force breaks down the differentiability properties that are prerequisites for a simple mathematical treatment of Newtonian dynamics. Since all mainstream numerical differential equation (DE) solvers are based on the assumption of proper differentiability, a special method was required that can handle these discontinuities. The very popular fourth order Runge-Kutta method was excluded because of the necessary intermediate steps that would make impossible handling the discontinuities occurring within a timestep.

Three simpler solvers were considered:

1. Euler's first order one-step DE solver uses the following iterative formulas:

$$\begin{cases} x_{n+1} = x_n + v_n h + O(h^2) \\ v_{n+1} = v_n + a_n h + O(h^2) \end{cases} \quad (1)$$

It proves not to be suitable for simulating oscillatory motion as the accumulation of overshoots at the turning points lead to an exponential increase in the amplitude of the oscillations. This effect is clearly visible in the upper frame of figure 2. There the solution of a $x'' + x = 0$ type of simple harmonic oscillator is represented using the different algorithms. The dotted thick line corresponding to the Euler solution exhibiting a tenfold increase over 100 time units for $h = 0.1$. The thin dashed line is the exact solution shown for comparison.

2. A modified version of this method is one order higher and defined by the iterative formula:

$$x_{n+1} = x_n + v_n h + \frac{1}{2} a_n h^2 + O(h^3) \quad (2)$$

However, the higher order only slows the divergence of the method otherwise exhibiting the same symptoms – thick line in the upper frame of figure 2.

3. The third order Verlet algorithm [Frenkel96] consists in the two-step iteration formula

$$x_{n+1} = 2x_n - x_{n-1} + a_n h^2 + O(h^4) \quad (3)$$

As shown in the lower frame of figure 2, it fully conserves energy even after 1000 time units and only exhibits a slight change in the period of the oscillations. The used timestep was again $h = 0.1$ and the dashed line represents the exact solution.

Therefore, at the basis of the solver eventually implemented there is the above Verlet-algorithm extended to handle the “stick-slip” events. The iteration formula was used whenever subsequent steps had non-vanishing velocities. At stopping, restarting and turning points the following procedure was followed:

Stopping: the event was detected by the change in sign between v_{n-1} and v_n . Since the simple Verlet algorithm described by (3) does not use velocity this had to be approximated. The approximation must be second order if to preserve the third order in the integration of the position. By using a third order Taylor expansion of the position around x_n , differentiating it with respect to time and expressing v_{n+1} as a function of the position and acceleration we get:

$$v_{n+1} = \frac{x_n - x_{n-1}}{h} + \frac{h}{6}(11a_n - 2a_{n-1}) + O(h^3).$$

Beside the positions x_n, x_{n-1} also the accelerations a_n, a_{n-1} are recorded. At the turning points there is a large change in the acceleration due to the flip in the direction of the friction force. Therefore, we make the block stop for one time step. In order to find the position where the block stops we have to first estimate the time necessary for the motion to cease. This time has to be a fraction $0 < z < 1$ of h calculated in a similar fashion as the velocity, using the Taylor-series expansion of the position up to third order yielding four coefficients to be determined. These can be found from $x_n, x_{n-1}, a_n, a_{n-1}$ subsequent to two differentiations with respect to time. In the formula for the velocity the timestep zh could be calculated by setting $v(zh) = 0$ and solving the emerging second order algebraic equation. Unfortunately, the abrupt changes in the natural length of the spring, i.e., of the accelerations sometimes coincide with these turning points producing z values that don't respect the $0 < z < 1$ requirement. In such cases the solution with lower absolute value is used. This is an obvious flaw of the algorithm. Nevertheless, test shows that the number of such events are rare – up to a couple of dozens per 100.000 full period oscillations -- and produce no visible change in any of the quantities of interest. In all cases, unless stated otherwise, the timestep is $h = 0.001$.

Starting: A block can start because one of two reasons: i.) it passed a turning point ii.) it starts slipping after a 'stick' period. In the former case the position is refreshed as $x_{n+1} = x_n + \frac{a_n h^2}{2}$, $v_n = a_n h$. The second case is detected by finding that the increasing free force – due to the spring – acting on the block exceeds that from friction: $f_n > \mu$. The two step history of the iteration is broken. First we have to estimate what percentage $0 < \delta < 1$ of the previous step was spent still resting and then integrate the kinetic equation of motion for the remaining $(2 - \delta)h$ to obtain x_{n+1} and v_{n+1} . Assuming a linear increase in the force δ can be approximated as:

$$\delta = \frac{\mu - f_{n-1}}{f_n - f_{n-1}},$$

and the velocity and position becomes:

$$v_{n+1} = \frac{1}{2} a_n h \frac{(2 - \delta)^2}{1 - \delta}, \quad x_{n+1} = x_{n-1} + \frac{1}{6} a_n h^2 \frac{(2 - \delta)^3}{1 - \delta}.$$

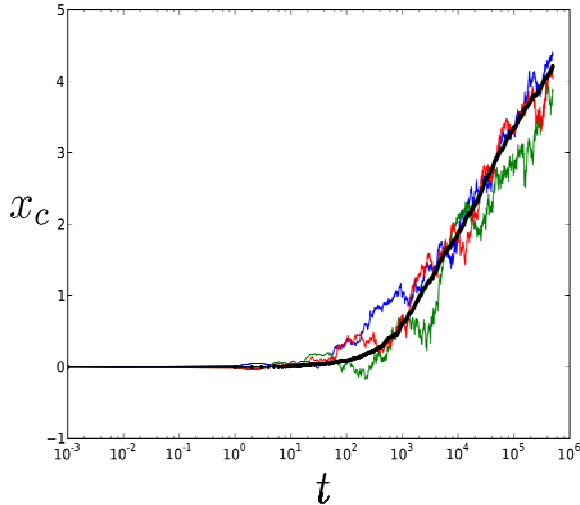


Figure 3. Evolution of the center of mass for $a=0.05$, $b=0.07$, $\Delta t=1.0$, $l_s=0.1$ and $h=0.001$. Thin lines represent three samples of the statistical ensemble, while the thick line is the ensemble average of 74 runs. Note the semilogarithmic representation. Note the logarithmic scale on the horizontal axis.

By studying experimentally the dependence of the final position on the timestep one could conclude that the algorithm as a whole is first order. The details of this study are not presented in this report. This finding allows for the speculation that using an energy conserving second order DE solver method instead of the third order Verlet scheme would have been sufficient. On the other hand, a series of test have been performed to check for the correctness of the algorithm. These include the study of energy and momentum conservation in case of no friction, the exact harmonic solution when one of the blocks was subject to a friction force that prevented its motion, etc.

4. Results

As stated in section 2, the primary object of the study is the dependence of the drift of the two block system on the different parameters. The two blocks were considered identical and of unity mass. These parameters are: the a gradient and b offset in the $\mu(x) = ax + b$ spatial dependence of the friction; the l_s width of the spring's l_0 natural length distribution; and finally the time interval Δt characterizing the rate of change in l_0 , in other words the inverse of the update frequency.

In the case of no gradient in the friction field the center of mass exhibits no drift as expected. For non-vanishing gradients a drift sets in exhibiting an asymptotic behavior at larger x .

On figure 3 one can identify three stages in the time dependence of the center of mass. The initial rather flat region is a transient spanning only a few time units and of little interest for this study. The subsequent curved and linear regions at a closer look reveal very distinctive features. Figure 4 is a zoom in to the these two regions. The two segments of length 550 time units have been shifted along both the time and position axes so that they could be viewed side by side. Therefore the values on the axes are only included for setting the scale of the $x(t)$ dependences. The lower curve is a sample from the earlier stages of the evolution, starting from 10.000, with relatively low friction values and corresponding to the upward bending section of the curve in figure 3. The upper curve is a “snapshot” of

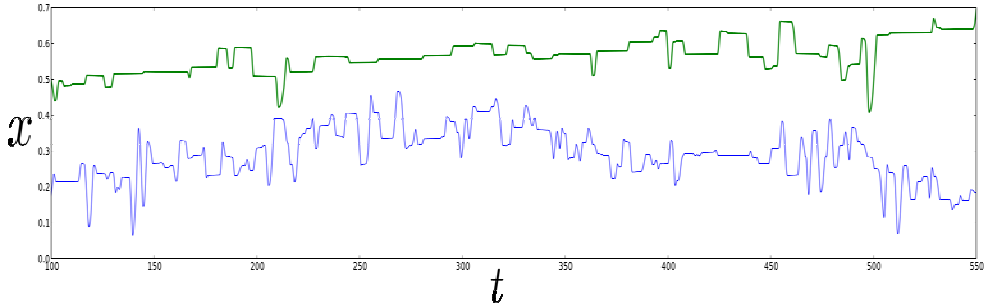


Figure 4. Zoom in to two different stages of the temporal evolution of the left block's position. The lower curve is a sample from the upward bending section of the curve in figure 3 starting from time 10.000. Above there is a similar snapshot from the linear section of figure 3, starting from time 1.010.000. The samples have been shifted in space and time so that they could be viewed next to

each other. The used parameters were $a=0.04$, $b=0.1$, $\Delta t=1.0$, $l_s=0.1$ and $h=0.001$.

the same length taken at times starting from 1.010.000. There is an apparent difference between the two behaviors which needs explanation. However, present study does not cover this aspect and henceforth we shall focus exclusively on the

linear section. In the limit of large times the dependence of the center of mass on time is:

$$x(t) = \alpha \log(t) + x_0$$

From the above formula we can deduce for the time and space dependence of the velocity that:

$$v(t) = \frac{\alpha}{t}, \quad v(x) = \alpha e^{-\frac{x-x_0}{\alpha}}$$

In the following we shall be interested in the slope parameter α which we shall refer to as *asymptotic drift slope* or simply *drift slope* while to x_0 as *drift shift*.

Figure 5. shows the obtained drift slope values for a number of different friction field gradients. The existence of a maximum is not surprising as for vanishing gradients the symmetry of the system prevents drift in any given direction while large gradients cause a quick rise in the friction force therefore slowing down drift.

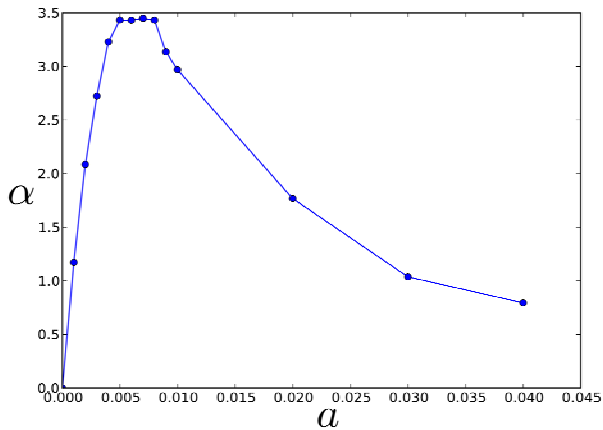


Figure 5. Dependence of the asymptotic drift slope on the gradient of the friction field. The used parameters were $b=0.04$, $\Delta t=1.0$, $l_s=0.1$ and $h=0.001$

In this model, the element that best accounts for the thermal coupling between the system and the environment is the intermittent change in the natural length $l_0(t)$ of the spring providing extra energy when the system comes to rest. The “amplitude” of this fluctuation, i.e., the width of the distribution, is directly

related to the temperature. As such higher temperature is expected to yield more vivid motion and as a consequence the slope of the drift must be a monotonously increasing function of the distribution width l_s . Beside confirming these expectations the simulations reveal a simple linear dependence as shown in figure 6.

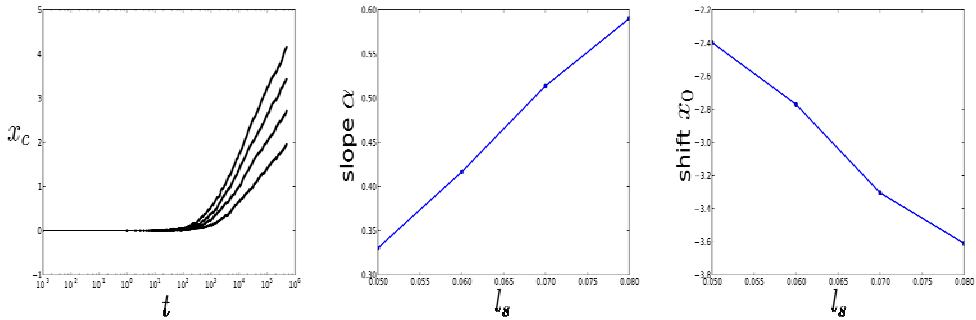


Figure 6. Dependence of the asymptotic drift slope on the spring's natural length distribution width. The used parameters were $a=0.04$, $b=0.05$, $\Delta t=1$ and $h=0.001$. Note the logarithmic scale on the first frame's horizontal axis.

Using various Δt update times for the natural length of the spring influences the results somewhat similar to the variance of the spring's natural length. Figure 7. shows the results of two runs with different update times set. The used parameters were $a=0.05$, $b=0.07$, $l_s=0.1$ and $h=0.001$.

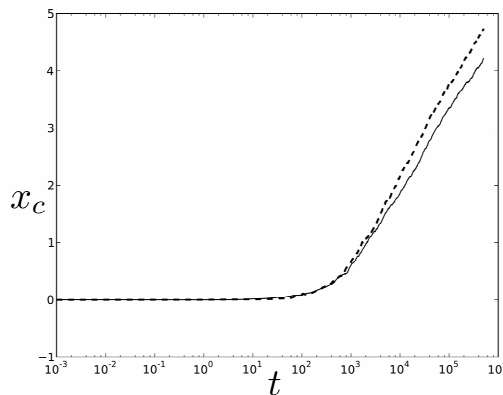


Figure 7. Influence of the update time in the natural length of the spring on the evolution of the drift. Thick solid line stands for $\Delta t = 1$ while the dashed line for $\Delta t = 2$. Note the logarithmic scale on the horizontal axis.

5. Discussion

The general behavior of the system is strongly influenced by the gradient of the friction field, the width of the spring's natural length distribution and to less extent by the update time interval of the spring.

It is to note that this four dimensional $(a, b, l_s, \Delta t)$ parameter space is rather narrow. An order of magnitude change in any of the parameters will either ruin the simulation, e.g., produces negative friction or negative natural spring length, or leads to time scales that could not be covered by computer simulation with the resources available for this study.

Since this study was meant to be a preliminary one there is room for a variety of improvements and further investigations. We might check whether we could improve the order of accuracy of our simulator. If not, it might be worthwhile replacing the two step, third order Verlet integrator with a one step, second order method to get a simpler and more efficient solver. As a monotonous space dependence of the friction force is difficult if not impossible to realize experimentally, studying a periodic friction space, e.g., saw-tooth profile, might be more relevant from the perspective of applicability. Extending the model to a larger number of blocks stringed together and to higher spatial dimensions yields to a rich set of friction space and initial condition configurations with possible exotic behavior. In order to avoid the anomalies appearing due to coincidences between the turning points and change in the spring's natural length, a smoothly but still randomly varying natural length could be used. Alternatively, the algorithm could be endowed with a simple protection so that the change in the natural length is conditioned by the lack of turning points.

ACKNOWLEDGEMENTS

This study was sponsored by the romanian IDEI/PN2 nr. 2369 research grant. The research idea was proposed by Zoltán Néda. Both his and Iosif Lázár's input is gratefully acknowledged.

REFERENCES

1. [Burrige67] R. Burrige and L. Knopoff, Model and theoretical seismicity, Bull. Seism. Soc. Am, Vol. **57**, pp. 341-371 (1967)
2. [Frenkel96] D. Frenkel and B. Smit, Understanding Molecular Simulation: From Algorithms to Applications, Academic Press (1996)
3. [Khataee10] A. R. Khataee and H. R. Khataee, Mechanical and Dynamical Principles of Protein Nanomotors: The Key to Nano-Engineering Applications, Nova Science Pub Inc. (2010)
4. [Néda09] Z. Néda, F. Járαι-Szabó, E. Káptalan and R. Mahnke, Spring-block models and highway traffic, Contr. Eng. and App. Inf., Vol.**11**, No.4, pp. 3-10 (2009)

RADIATION PROTECTION IN DIAGNOSIS AND TREATMENT PROCEDURES WITH ¹³¹I

C. MOISESCU¹, D. PICIU¹, V. SIMON²

ABSTRACT. Dosimetry calculation was carried out for each individual patient in order to evaluate the optimal dose of radioisotopes and radiation compliance for the patient and for personnel handling radioactive sources. The data are obtained from a group of patients receiving radioiodine to ablate the thyroid after surgery and from another group receiving subsequent treatments for residual or recurrent disease. Related to the first group, the cumulative dose to nursing staff for the week after treatment was estimated at 0.08 mSv for a self-caring patient to 6.3 mSv for a totally helpless patient, while corresponding doses to nurses looking after patients receiving subsequent treatments for residual or recurrent disease were 0.18-12.3 mSv.

Keywords: *radioiodine, thyroid carcinoma, radiotherapy, radiation protection*

Introduction

Nuclear medicine is a branch of medicine that uses radiation to provide information about the functioning of a person's specific organs or to treat disease. In most cases, the information is used by physicians to make a quick, accurate diagnosis of the patient's illness. The thyroid, bones, heart, liver and many other organs can be easily imaged, and disorders in their function revealed. In some cases radiation can be used to treat diseased organs, or tumours.

The main advantage of radioactive iodine-131 (¹³¹I) isotope consists in the fact that it is strictly for cell tropism of thyroid. This is the reason of radioiodine use with great success in thyroid diseases, especially in the treatment of thyroid cancer. ¹³¹I has been largely used in the last decades to treat thyroid pathology because it is clinically effective, safe, and low priced in comparison with the therapeutic alternatives [1, 2].

Since there has already been experience with the therapeutic application of ¹³¹I in the treatment of thyroid cancer, this isotope was one of the first tested for radioimmunotherapy. It emits both β and γ rays. The latter property can be useful for imaging or dosimetry calculation. Its beta component is of relatively low energy, hence of a relatively short path length of 0.8 mm. Iodine is released in tissues at a variable rate through dehalogenation or as a result of the immunoglobulin break

¹ Ion Chiricuta Oncological Institute, Department of Nuclear Medicine, 400015 Cluj-Napoca, Romania

² Babes-Bolyai University, Faculty of Physics, 400084 Cluj-Napoca, Romania

down in the form of iodinated tyrosine residues which are renally cleared. The avid uptake of ^{131}I by the thyroid gland mandates the use of saturated potassium iodine solution to prevent thyroid irradiation. The biological half-life of ^{131}I varies widely and unpredictably among patients and only partially depends on renal clearance. These issues obligate the use of dosimetry in clinical practice[3].

Despite its wide use, there remain many controversies surrounding ^{131}I use, including how clinicians should determine the optimal dose. Patients treated with radioiodine present a radiation hazard and precautions are necessary to limit the radiation dose to family members, nursing staff and general population. The precautions advised are usually based on instantaneous dose rates or iodine retention and do not take into account the time spent in close proximity with a patient.

The main purpose of this study is the radiation protection required immediately in the post administration period, and forecasts regarding patient progress and subsequent therapeutic management.

Experimental

After I-131 oral administration the gamma radiation from patients was detected using a radioiodine uptake (Ric) station anterior or linear scintigraph. A relative new method for thyroid cancer investigation, based on whole body scan scintigraphy after I-131 administration, was applied. The scan is performed with collimated gamma camera with high energy, and highlights residues of thyroid tissue, cervical metastasis and slight metastasis of thyroid cancer.

We have combined whole-body dose rate measurements taken from 132 thyroid cancer patients after radioiodine administration with known data on nursing and social contact times to calculate the cumulative dose that may be received by an individual in contact with a patient. These estimated doses have been used to calculate restrictions to patients' behaviour to limit received doses to less than 1 mSv. We have also measured urinary iodide excretion of patients to estimate the potential risk from the discharge of radioiodide into the domestic drainage system.

Dosimetry calculation was carried out for each individual patient in order to evaluate the optimal dose of radioisotopes and radiation compliance for the patient and for personnel handling radioactive sources. The data are obtained from a group of patients receiving radioiodine to ablate the thyroid after surgery (the ablation group, A) and from another group receiving subsequent treatments for residual or recurrent disease (the follow-up group, FU).

Results and discussion

Ric values recorded at 24 hours on the thyroid and at thigh indicates the charging level and the presence of the radioisotopes in the bloodstream (Table 1).

Table 1.

Data on patients, ¹³¹I dose, radioiodine uptake and dose debit.

Patient code	Patient age (yrs)	Patient weight (kg)	Administrated dose (mCi)	Ric after 24 hrs thyroid /thigh (counts)	Dose debit after 24 hrs (mR/h)
1	47	70	38,85	1712386/ 98365	18,3
2	50	88	90,65	1899346/ 101560	19,7
3	61	61	38,85	1654320/ 89936	20,6
4	61	77	90,65	1883591/ 101236	23,4
5	34	80	50	1553736/ 753011	21,05
6	56	63	70	1882928/ 814154	14,08
7	52	72	70	1842474/ 713210	13,25
8	64	58	70	920530/ 88321	11,5
9	60	60	50	1001235/ 90654	12,8
10	38	95	70	3182844/ 186945	11,4

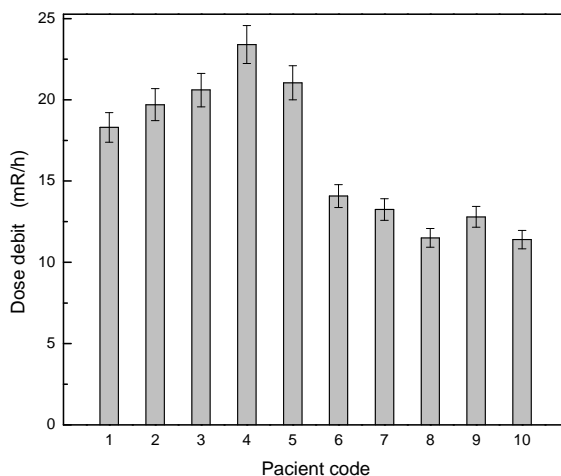


Fig. 1. Dose debit 24 hours after dose administration.

The wide and unpredictable variation in the radiation emitted by different patients can be observed in Fig. 1, for ten subjects, 24 hours after ^{131}I administration. Doses of 38.85, 50, 70 or 90.65 mCi were used for patients aged between 34 and 64 years. It is difficult to apprehend a certain dependence on either weight (Fig. 2) or age. Very close values of dose debit are recorded from two patients which are 34 and 61 years old. On the other hand, considering the 70 mCi therapy (Fig. 3), an expected increase of dose debit with dose/weight ratio is noticed, with a surprising exception. By comparison, a very low dose debit is measured for the highest ratio of administrated dose / patient weight, and this was the case of the oldest patient. These data are in agreement with other results reported on the kinetics of ^{131}I used in radioimmunotherapy [3-12]

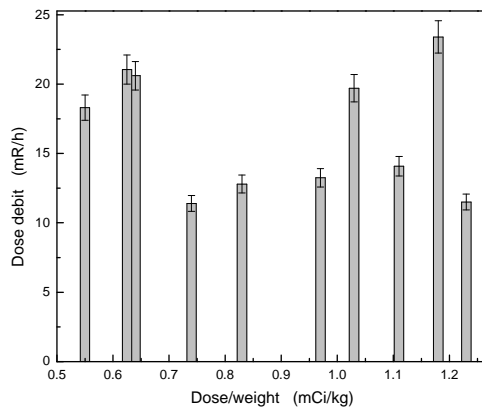


Fig. 2. Dependence of dose debit 24 hours after dose administration on dose / patient weight ratio.

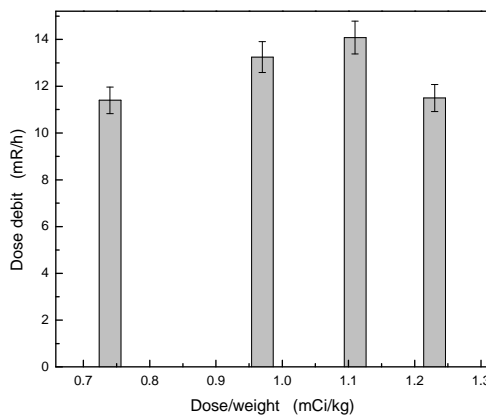


Fig. 3. Dependence of dose debit 24 hours after 70 mCi ^{131}I administration on dose / patient weight ratio.

Recent research [13] reports on the role of radio-guided surgery with iodine-131 using the steps which we further mention as an example. First the patients are hospitalized and receive a therapeutic 3.7 GBq (100 mCi) dose of I-131 after thyroid hormone therapy withdrawal in condition of overt hypothyroidism. After three days a whole body scan following the therapeutic I-131 dose administration is acquired. After five days neck surgery is performed through a wide bilateral neck exploration using a 15-mm collimated gamma probe, measuring the absolute intra-operative counts and calculating the lesion to background ratio. After seven days post-surgery is performed using the remaining radioactivity to evaluate the completeness of tumoral lesions extirpation.

The dose rate decay was biexponential for patients receiving radioiodine to ablate the thyroid after surgery (the ablation group, A) and monoexponential for these receiving subsequent treatments for residual or recurrent disease (the followup group, FU). These values are important because they depend on the future in terms of patients radiation and their family. Advice given to patients receiving radioiodine therapy is based on retained activity or instantaneous dose rate measurement and takes little or no account of patient behaviour. The doses received by staff, members of the public and family will be influenced by the patients' retained activity and the length and proximity of contact with those individuals.

The rapid clearance of radioiodine in patients treated on one or more than one occasion means that therapy could be administered at home to selected patients with suitable domestic circumstances. In most cases the restriction times, despite the high administered activities, are less than those for patients treated for thyrotoxicosis. The concentration of radioiodide in domestic drainage systems should not pose a significant risk.

The faster clearance in the follow-up patients generally resulted in less stringent restrictions than those advised for ablation patients. For typical activities of 1850 MBq for the ablation patients and 3700 MBq for the follow-up patients, the following restrictions were advised. Patients could travel in a private car for up to 8 h on the day of treatment (for an administered activity of 1850 MBq in group A) or 4 h (for activities of 3700 in group FU) respectively. Patients should remain off work for 3 days (1850 MBq/group A) or 2 days (up to 3700 MBq/group FU). Partners should avoid close contact and sleep apart for 16 days (1850 MBq/group A) or 4-5 days (3700 MBq/group FU). Contact with children should be restricted according to their age, ranging from 16 days (1850 MBq/group A) or 4-5 days (3700 MBq in group FU) for younger children, down to 10 days (1850 MBq/group A) or 4 days (up to 3700 MBq/group FU) for older children.

Conclusions

Wide and unpredictable variation in the ^{131}I radiation emitted by different patients was observed. Sensible guidelines can be derived to limit the dose received by

members of the public and staff who may come into contact with cancer patient treated with radioiodine to less than 1 mSv. The cumulative dose to nursing staff for the week after treatment was dependent on patient mobility and was estimated at 0.08 mSv for a self-caring patient to 6.3 mSv for a totally helpless patient (1840 MBq/group A). Corresponding doses to nurses looking after patients in group FU were 0.18-12.3 mSv (3700 MBq).

REFERENCES

1. M. Hirota, T. Saze and K. Nishizawa, *Radiat. Prot. Dosim.*, 101 (2002) 457.
2. M. Jang, H. K. Kim, C. W. Choi, C. S. Kang, *Radiat. Prot. Dosim.*, 130 (2008) 499.
3. P.C. Emmanouilides, *Rev. Esp. Med. Nucl.* 25 (2006) 42.
4. K. Koizumi, G.L. DeNardo, S.J. DeNardo, M.T. Hays, H.H. Hines, P.O. Scheibe, J.S. Peng, D.J. Macey, N. Tonami, K. Hisada, *J. Nucl. Med.*, 27 (1986) 1243.
5. M.S. Kaminski, L.M. Fig, K.R. Zasadny, K.F. Koral, R.B. DelRosario, I.R. Francis, C.A. Hanson, D.P. Normolle, E. Mudgett, C.P. Liu, S. Moon, P. Scott, R.A. Miller, R.L. Wahl, *Clin. Oncol.*, 10 (1992) 1696.
6. R. Schnell, M. Dietlein, O. Staak, V. Diehl, A.N. Engert, *Blood*, 100 (2002) 100a.
7. M.S. Kaminski, J. Estes, K.R. Zasadny, I.R. Francis, C.W. Ross, M. Tuck, D. Regan, S. Fisher, J. Gutierrez, S. Kroll, R. Stagg, G. Tidmarsh, R.L. Wahl, *Blood*, 96 (2000) 1259.
8. J.M. Vose, R.L. Wahl, M. Saleh, A.Z. Rohatiner, S.J. Knox, J.A. Radford, A.D. Zelenetz, G.F. Tidmarsh, R.J. Stagg, M.S. Kaminski, *J. Clin. Oncol.*, 18 (2000) 1316.
9. S. Horning, A. Younes, J. Lucas, V. Jain, *Blood*, 100 (2002) 357a.
10. O.W. Press, J.F. Eary, T. Gooley, A.K. Gopal, S. Liu, J.G. Rajendran, D.G. Maloney, S. Petersdorf, S.A. Bush, L.D. Durack, P.J. Martin, D.R. Fisher, B. Wood, J.W. Borrow, B. Porter, J.P. Smith, D.C. Matthews, F.R. Appelbaum, I.D. Bernstein, *Blood*, 96 (2000) 2934.
11. M.S. Kaminski, A.D. Zelenetz, O.W. Press, M. Saleh, J. Leonard, L. Fehrenbacher, T.A. Lister, R.J. Stagg, G.F. Tidmarsh, S. Kroll, R.L. Wahl, S.J. Knox, J.M. Vose, *J. Clin. Oncol.*, 19 (2001) 3918.
12. V.L. Gates, J.E. Carey, J.A. Siegel, M.S. Kaminski, R.L. Wahl, *J. Nucl. Med.*, 39 (1998) 1230.
13. D. Rubello, M. Salvatori, G. Ardito, G. Mariani, A. Al-Nahhas, M.D. Gross, P.C. Muzzio, M.R. Pelizzo, *Biomed. Pharmacother.*, 61 (2007) 477.

ELECTRONIC PROPERTIES OF MnCo SYSTEM ALLOYS

A. NEDELICU¹, V. CRISAN

ABSTRACT. The Magnetic properties of MnCo alloys were computed by using the KKR-CPA-MS method in the high concentration of Mn limit. It was found that the magnetic coupling between Co and Mn atoms strongly depend on the atomic volumes, i.e. the lattice parameter. The magnetovolume effect was found to be the effect of both the Mn atoms magnetic moment variation with the atomic volume in pure Mn as well as the anisotropic exchange interactions.

Keywords: *band structure, KKR, magnetovolume instability.*

Introduction

The Mn and Co magnetic coupling was a subject of controversy in the last decades. The MnCo magnetic moment coupling becomes even more complicated when the Mn atoms are deposited as a thin layer on the fcc Co(001). The coupling between Mn deposited in ultrathin overlayer on Co was of ferromagnetic(F) type, but rather than MnCo alloying a nonideal Mn overlayer(s) was suggested to grow at the Mn-Co interface. It was shown that the MnCo deposited on the fcc Co(001) shows a chemical [1,2] ordering with antiferromagnetic(AF) coupling between atoms. For the specific case of Mn_{0.5}Co_{0.5}/Co(001) the ordered surface alloy is more stable than the Mn monolayer on Co(001). The F coupling between Mn and Co has been obtained as well but this configuration is unstable as compared to the solution with AF coupling.

Computational method.

The MnCo alloys system has a fcc structure for the whole range of concentration. In order to allow the spin to have different values in the unit cell (see Figure 1) we used the multiple sublattice KKR-CPA.

The lattice is split in two sublattices denoted by I and II, (see Fig. 1). The atoms are statistically distributed in both sublattices subject of only the concentration constraint on site and on the unit cell. Also we considered that all the atoms located on the faces (sublattice II) have the same properties. This way the tendency for the L10 ordering, seen in most of the 3d transition metal alloys, is taken into account [3]. The calculations were done in the LSDA while for exchange and correlation the parametrisation given by Moruzzi, Yanak and Williams[4] was used. The screening was not taken into consideration.

¹ Faculty of Physics, Babes-Bolyai University Cluj-Napoca.

Because the chemical ordering is not present in bulk MnCo alloys the chemical composition in both sublattices were considered to be the same.

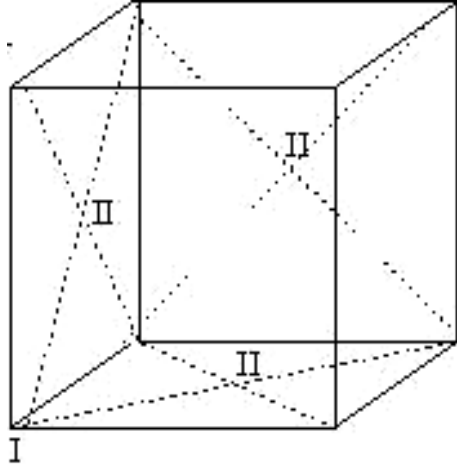


Figure 1. The FCC unit cell of MnCo alloys was split in two sublattices denoted by I and II in order to allow a different behaviour of the alloy atoms.

Results and discussions.

The magnetic moment calculations were done for $\text{Mn}_{0.95}\text{Co}_{0.05}$ by using the fcc unit cell described as a cubic structure with two sublattices I and II, as seen in Figure 1. The total and atomic magnetic moments are shown in Figure 2. As was expected, due to the large Mn concentration, a large magnetovolume effect is observed. However, the effect is produced not only by the decreases of the Mn magnetic moment but the change in the spin orientations mainly for the Mn atoms. While the Mn atoms located in sublattice II remaine parallel with the Co atomic moments, the Mn atoms from the sublattice I flip and the Mn and Co atoms are coupled AF.

The conclusion is that the magnetic coupling between the Mn and Co in bulk MnCo alloys is strongly related on the atomic volume and because of the statistical distribution of the atoms in alloys on the nearest neighboring atoms.

A strong volume dependence of the Mn atoms was calculated [5] as were obtained experimentaly [6]. It is worth mentioning that the pure Mn show an instability region with a discontinuous change from a low-spin state to a high-spin state with increasing lattice constant as was already shown in Fe alloys[3].

Due to the large Mn content in the alloy it is obvious that the transition from high spin state (HS) to low spin (LS) state observed in ref.5 is responsible for HS to LS transition in MnCo alloys. The small Co content seems do not disturbed the pure Mn behavior.

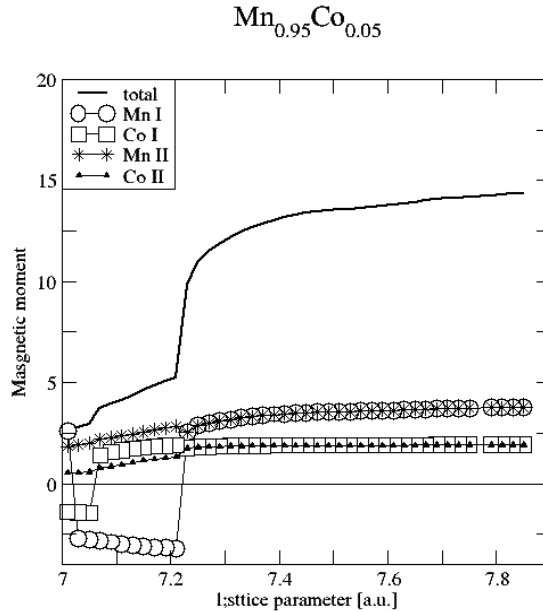


Figure 2. Total and atomic magnetic moment (in Bohr magnetons) as function of lattice parameter. Full curve represent the total magnetic moment, circle (\circ) the Mn I, star ($*$) Mn II atomic moments while open square (\square) and triangle up (Δ) the CoI and CoII atomic magnetic moments in $\text{Mn}_{0.95}\text{Co}_{0.05}$

Working in the CPA the spin configuration cannot be specified, the only result is that for lattice parameter less than 7.2 a.u. the Mn atoms as well as the Mn and Co atoms could be coupled AF. Closer to 7a.u. the Co atoms from the sublattice I have the tendency of AF ordering with the sublattice II atoms.

REFERENCES

1. W. L. O'Brien, B. P. Tonner, Phys.Rev. B58, 3191 (1998).
2. B.-Ch. Choi, J. P. Bode, J. A. C. Bland, Phys. Rev. B58, 5166 (1998).
3. V.Crisan, P. Entel, H. Ebert, H.Akai, D. D. Johnson, J.B.Stunton, Phys.Rev., B66, 014416 (2002).
4. L. Moruzzi, J.F. Janak, A. R. Williams, *Calculated Electronic Properties of Metals* (Pergamon, New York, 1978).
5. N.E. Brener, G. Fuster, J. Callaway, J.L. Fryand and Y.Z.
6. Zhao, J. Appl. Phys. 63 4057, (1988).
7. J.W. Cable, Y. Tsunoda Journal of Magnetism and Magnetic Materials 140 93 (1995).

ESR AND RAMAN STUDY OF $V_2O_5 - P_2O_5 - Bi_2O_3$ GLASS SYSTEM

R. STĂNESCU¹, N. VEDEANU², L. TIBRE¹ AND I. ARDELEAN¹

ABSTRACT. $xV_2O_5(1-x)$ [0,8 P_2O_5 , 0,2 Bi_2O_3] glass system, with $0 \leq x \leq 50\%$ mol, was prepared and investigated by ESR and Raman methods. For low content of V_2O_5 all the ESR spectra present a hyperfine structure typical for isolated V^{4+} ions. With the increasing of V_2O_5 content, ESR absorption signal showing hyperfine structure is covered by a broad line without hyperfine structure characteristic for clustered ions. At high V_2O_5 content, the vanadium hyperfine structure disappears and only the broad line can be observed in the spectra.

The changes observed in the Raman spectra at low concentration of V_2O_5 content ($x < 10$ mol %) show that vanadium oxide acts as a network modifier of the glass matrix, the bands belonging to the phosphate groups being strongly reduced. At high content of vanadium ($x > 20$ mol %), the vibrations characteristic for V-O-P groups appear in the spectra and the V_2O_5 oxide acts as a network former.

Keywords: $V_2O_5 - P_2O_5 - Bi_2O_3$ glasses, ESR.

1. Introduction

Glasses containing transitional metal (TM) ions have been studied mainly because of their interesting optical, thermal and magnetic properties and potential applications. The technological importance of these glasses requires a detailed understanding of the molecular and structural chemistry in order to help the determination of relationships between physical properties and their structural units [1-2].

Phosphate glasses are of large interest for a variety of technological applications due to several unique properties, such as high thermal expansion coefficient, low viscosity, UV transmission or electrical conduction [3].

The addition of transitional metal oxides, such as V_2O_5 in the phosphate glasses, was investigated by several researchers [4-7]. The vanadyl ion VO^{2+} incorporated in glasses, as spectroscopic probe, is useful to characterize the glass local structure. The VO^{2+} ion, like other transitional metals, provide information about many specific aspects as a geometry of structural units of the glass network, the character of chemical bonds in glasses as well as the coordination polyhedra (local symmetry) of transitional metal ions [5,6].

¹ Babes-Bolyai University, Faculty of Physics, RO-400028 Cluj-Napoca, Romania

² Iuliu Hatieganu University of Medicine and Pharmacy, RO-400023 Cluj-Napoca, Romania

In fact, a very recent problematic related to phosphate glasses doped with TM ions regards the dual role as network former and modifier that some TM oxides may have. It was demonstrated by means of Raman spectroscopy that some ions (tungsten, iron or vanadium) act as network modifiers but also as network formers depending by their concentration in the glass matrix [8-10].

The structure of bismuthate oxide glasses has been studied by Raman spectroscopy and it was evidenced that the binary and multicomponent bismuthate glasses contain two types of structural units, pyramidal BiO_3 and octahedral BiO_6 units in variable proportions [11-14].

In this paper, $xV_2O_5(1-x)[0.8P_2O_5 \cdot 0.2Bi_2O_3]$ glass system with $0 \leq x \leq 50$ mol% mol was prepared and investigated by ESR and Raman spectroscopy, in order to obtain further information about the local symmetry, interactions and structural changes induced by the increasing of V_2O_5 content in the glass matrix.

2. Experimental

In order to obtain the $xV_2O_5(1-x)[0.8P_2O_5 \cdot 0.2Bi_2O_3]$ glass system ($0 \leq x \leq 50$ mol %) was first prepared the matrix $[0.8P_2O_5 \cdot 0.2Bi_2O_3]$ by mixing $(NH_4)_2HPO_4$ with Bi_2O_3 and melting these admixtures at $1250^\circ C$ for 5 minutes in a sintered corundum crucible using a technique previously reported. The matrix was crushed and the resulting powder was mixed with appropriate amounts of V_2O_5 before final melting at $1250^\circ C$. The melted glasses were under cooling at room temperature by quickly pouring onto stainless steel plates.

The ESR spectra were obtained at room temperature, using an ADANI Portable PS8400 spectrometer in X-frequency band (9.4 GHz) and a field modulation of 100 KHz. For these measurements, equal quantity of powders from the investigated samples, closed in glass tubes, were used.

Raman spectra were recorded with a Portable Raman System 3000 with a spectral resolution of $\sim 4 \text{ cm}^{-1}$ using an excitation laser wavelength of 785 nm with a maximum power of 250 mW and a line width less than 0.5 nm. The detector was thermoelectrically cooled.

3. Results and discussion

a) ESR spectra

ESR spectra for $xV_2O_5(1-x)[0.8P_2O_5 \cdot 0.2Bi_2O_3]$ glass system with $0 \leq x \leq 50$ mol % are given in Fig. 1.

The ESR spectra obtained for the studied glasses with a small content of V_2O_5 ($x \leq 10$ mol%) show a well-resolved hyperfine structure (hfs) typical for isolated vanadium ions in a C_{4v} symmetry, present as vanadyl ions.

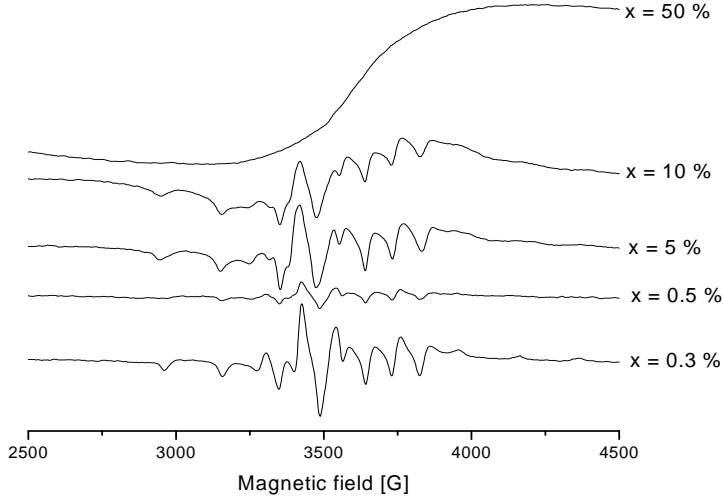


Fig. 1. ESR spectra of $xV_2O_5(1-x)[0.8 P_2O_5 \cdot 0.2 Bi_2O_3]$ glass system

The appropriate spin Hamiltonian for these spectra is:

$$H_s = \beta_0 g_{\parallel} B_z S_z + \beta_0 g_{\perp} (B_x S_x + B_y S_y) + A_{\parallel} S_z I_z + A_{\perp} (S_x I_x + S_y I_y) \quad (1)$$

where β_0 – Bohr magneton, g_{\parallel} and g_{\perp} – components of g tensor, B_x, B_y, B_z – components of the magnetic field, S_x, S_y, S_z – components of the electron spin operator, I_x, I_y, I_z – components of the nucleus spin operator, A_{\parallel} and A_{\perp} – principal components of the hyperfine coupling tensor.

The values of the magnetic field for the hfs peaks from the parallel and perpendicular absorption bands are given by the following eqs [15] :

$$B_{\parallel}(m) = B_{\parallel}(0) - mA_{\parallel} \left[\left(\frac{63}{4} \right) - m^2 \right] \cdot \frac{A_{\perp}^2}{2B_{\parallel}(0)} \quad (2)$$

$$B_{\perp}(m) = B_{\perp}(0) - mA_{\perp} \left[\left(\frac{63}{4} \right) - m^2 \right] \cdot \frac{(A_{\parallel}^2 + A_{\perp}^2)}{4B_{\perp}(0)} \quad (3)$$

where m – magnetic nuclear quantum number for vanadium nucleus having the following values: $\pm 7/2, \pm 5/2, \pm 3/2$ and $\pm 1/2$.

$$B_{\parallel}(0) = \frac{h\nu}{g_{\parallel}\beta_o} \quad (4)$$

$$B_{\perp}(0) = \frac{h\nu}{g_{\perp}\beta_o} \quad (5)$$

where ν is the microwave frequency.

ESR parameters for vanadium ions in the studied glasses are given in Table 1. The values obtained by us are in good agreement with other results reported in literature [9, 10, 15, 16].

Table 1.

ESR parameters for V⁴⁺ ions in xV₂O₅(1-x)[0.8P₂O₅ 0.2Bi₂O₃] glass system

x mol%	g _∥	A _∥ 10 ⁻⁴ cm ⁻¹	g _⊥	A _⊥ 10 ⁻⁴ cm ⁻¹	K	P	β ₂ ²	ε _π ²
0.3	1.92	197	1.99	77.30	0.84	139.65	1.04	0.91
3	1.92	199	2.00	77.28	0.83	142.00	1.16	0.90
5	1.93	198	2.00	77.28	0.83	140.84	1.08	0.94
10	1.92	195	2.00	77.28	0.85	137.34	1.10	0.92

The values of these parameters confirm that the vanadium ions exist in the studied glasses as VO²⁺ ions in octahedral coordination with a tetragonal compression, particularly of C_{4v} symmetry. The vanadyl oxygen is attached axially above the V⁴⁺ site along the z-axis (V=O bond), while the sixth oxygen forming the O - VO₄ - O unit lies axially below the V⁴⁺ site in opposition with “yl” oxygen. The predominant axial distortion of the VO²⁺ octahedral oxygen complex along V=O direction may be the reason for nearly equal g and A values for all glass samples [17, 18].

Fermi contact interaction term K, dipolar hyperfine coupling parameter P and MO coefficients are evaluated by using the expressions developed by Kivelson and Lee [19]:

$$K = \frac{2}{7} \frac{A_{\parallel} + 2A_{\perp}}{A_{\parallel} - A_{\perp}} \quad (6)$$

$$P = \frac{A_{\parallel} + 2A_{\perp}}{3K} \quad (7)$$

$$\beta_2^2 = \frac{7}{6} \left[\left(\frac{A_{\parallel} - A_{\perp}}{P} \right) - (g_e - g_{\parallel}) + \frac{5}{14} (g_e - g_{\perp}) \right] \quad (8)$$

$$\varepsilon_{\pi}^2 = \frac{\Delta_{\perp}(g_e - g_{\perp})}{2\lambda\beta_2^2} \quad (9)$$

where $\Delta_{\parallel} = 17400 \text{ cm}^{-1}$, $\Delta_{\perp} = 15100 \text{ cm}^{-1}$, $\lambda = 170 \text{ cm}^{-1}$ and $g_e = 2.0023$.

The value estimated for K (~ 0.84) indicates a poor contribution of the vanadium 4s orbital to the vanadyl bond in these glasses.

The shape of the spectra is modified with the increasing of vanadium ions content. This modification consists in the partial disappearance of the vanadyl hfs and in the appearance of a broad line due to the clustered ions coupled by dipole-dipole interaction.

For high content of vanadium oxide ($x \geq 10 \text{ mol } \%$), the ESR spectra may be regarded as a superposition of two ESR signals, one with a well-resolved hfs typical for isolated VO^{2+} ions and another one consisting in a broad line typical for associated $\text{V}^{4+}\text{-V}^{4+}$ ions. The number associated ions increases with the increasing of V_2O_5 content. The formation of associated V^{4+} ions in the composition range of $x < 10 \text{ mol}\%$ is due to the dipole-dipole interaction between vanadium ions.

b) Raman spectra

The Raman spectra of $x\text{V}_2\text{O}_5(1-x)[0.8\text{P}_2\text{O}_5 \cdot 0.2\text{Bi}_2\text{O}_3]$ glass matrix is presented in Fig.2. For the studied $x\text{V}_2\text{O}_5(1-x)[0.8\text{P}_2\text{O}_5 \cdot 0.2\text{Bi}_2\text{O}_3]$ glasses with $0 \leq x \leq 50 \text{ mol}\%$, the assignments of the detected absorption bands are summarized in Table 2.

Table 2.

Frequencies and their assignments for Raman absorption bands of $x\text{V}_2\text{O}_5(1-x)[0.8 \text{ P}_2\text{O}_5 \cdot 0.2 \text{ Bi}_2\text{O}_3]$ glasses

Wavenumber (cm^{-1})	Raman assignment
~235	Bi – O bond vibrations in BiO_3 and BiO_6 groups
~300	Bi – O – Bi stretching vibrations in distorted BiO_6 octahedral units
~495	vibrations of the P – O – P bonds
~740	symmetric stretching vibration of P – O – P bonds
~900	V = O vibrations in the tetragonal pyramid of V_2O_5
~1050	vibrations in PO_2^- and PO_3^- groups
~1235	vibration of the P = O bonds

The following bands are present in the glass matrix spectrum: $\sim 255 \text{ cm}^{-1}$, $\sim 325 \text{ cm}^{-1}$, $\sim 495 \text{ cm}^{-1}$, $\sim 740 \text{ cm}^{-1}$, $\sim 1050 \text{ cm}^{-1}$ and $\sim 1235 \text{ cm}^{-1}$.

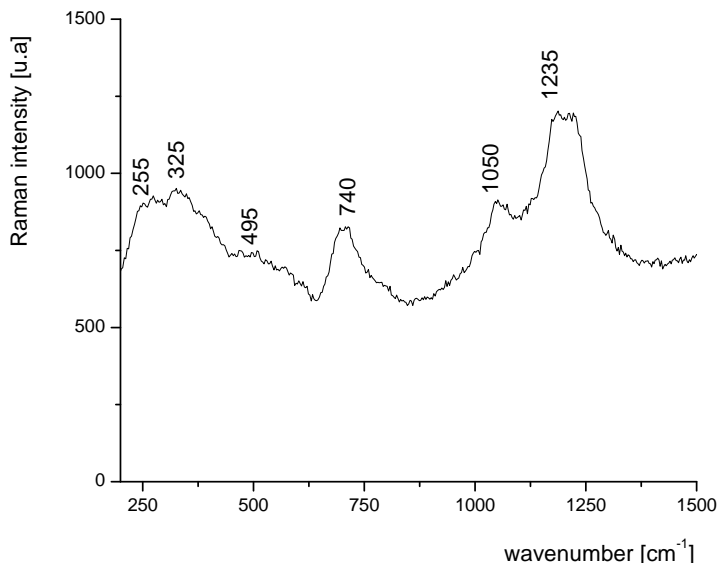


Fig. 2. Raman spectra of $xV_2O_5(1-x)[0.8 P_2O_5 \cdot 0.2 Bi_2O_3]$ glass matrix

The band at $\sim 235 \text{ cm}^{-1}$ indicates the presence of Bi-O bonds vibrations in BiO_3 and distorted BiO_6 units in the glass matrix [20]. The band appearing at 325 cm^{-1} is attributed to Bi-O-Bi stretching vibrations in the distorted BiO_6 units. This band is increasing gradually with the increasing of vanadium concentration but for samples with $x > 10 \text{ mol } \%$ decreases. A weak band centered at $\sim 495 \text{ cm}^{-1}$ is attributed to vibrations of the P-O-P bonds in PO_4 polyhedra, specific for all phosphate glasses. The strong band centered at $\sim 740 \text{ cm}^{-1}$ is characteristic to symmetric stretching vibration of P-O-P bonds [20-24]. The intensity of this band increases until 1 mol% and for samples with $x = 50 \text{ mol } \%$ disappears. The band centered at $\sim 1050 \text{ cm}^{-1}$ appears to the glass matrix and is assigned to vibrations in PO_2^- and PO_3^- groups [20-26]. At $\sim 1235 \text{ cm}^{-1}$, the spectra present a band assigned to the vibration of the P=O bonds [20-22].

For low V_2O_5 concentration, the shape of the spectrum is not significantly modified.

For high V_2O_5 concentration ($x > 20 \text{ mol } \%$), the shape of the spectrum is changed. Important band specific for the structural changes of the phosphate network occur in the spectra for $x = 50 \text{ mol } \%$ (Fig.3).

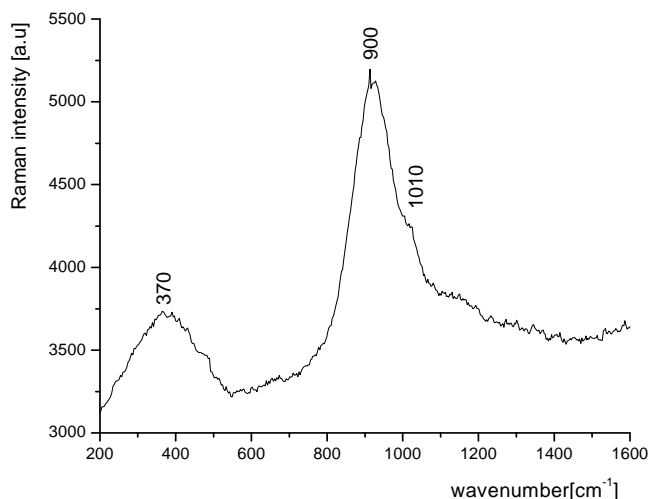


Fig. 3. Raman spectra of $x\text{V}_2\text{O}_5(1-x)[0.8\text{P}_2\text{O}_5\ 0.2\text{Bi}_2\text{O}_3]$ glasses with $x = 50$ mol %

A band at $\sim 370\text{ cm}^{-1}$ attributed to Bi – O – Bi stretching vibrations in distorted BiO_6 octahedral units increases in intensity in the spectrum [24-26]. The band at $\sim 740\text{ cm}^{-1}$ disappears, showing that the initial P – O – P bonds are now broken. A new band at $\sim 900\text{ cm}^{-1}$ appears assigned to V = O vibrations in the tetragonal pyramid of V_2O_5 . The band at $\sim 1235\text{ cm}^{-1}$ disappears also, because of the formation of V – O – P bonds, which makes weaker the initial P = O bond up to breaking it totally for $x = 50$ mol%. There is a reduction of the bonding force between P and O atoms that leads to the appearance of more non-bridging oxygen ions which are involved in the new TM-oxygen bonds.

Although previous papers [8,10] have shown that vanadium have a dual role, as glass network modifier for low concentration of ions and as network former for high content. A similar behavior of V_2O_5 in the studied $x\text{V}_2\text{O}_5(1-x)[0.8\text{P}_2\text{O}_5 \cdot 0.2\text{Bi}_2\text{O}_3]$ glass system was established too.

4. Conclusions

ESR spectra of studied glasses are considered a superposition of a well-resolved superhyperfine structure typical for isolated vanadium ions and a broad line characteristic for associated ions. The dipole-dipole interactions exist between paramagnetic ions until $x = 10$ mol % and the superexchange interactions prevail at high V_2O_5 content ($x > 20$ mol %).

Complementary to ESR measurements, Raman spectra show that the addition of TM oxides leads to the depolymerization of the phosphate network; in consequence V_2O_5 acts as network modifier at low concentration ($x < 10$ mol %). The appearance of V-O-P bonds at high content ($x > 20$ mol %) of V_2O_5 oxide proves that it acts as a network former in this case.

REFERENCES

1. A.Chahine, M. Et.-Tabirou, *Ann. Chim. Sci. Mat.* 28, 25 (2003)
2. R.K. Brow, *J. Non-Cryst. Solids* 263, 1 (2000)
3. B.C. Sales, *Mater. Res. Soc. Bull.* 12, 32 (1987)
4. I. Ardelean, O. Cozar, Gh. Ilonca, V. Simon, V. Mih, C. Craciun, S. Simon, *J. Mater. Sci.* 11, 401 (2000)
5. O. Cozar, I. Ardelean, V. Simon, L. David, V. Mih, N. Vedeanu, *Appl. Magn. Reson.* 16, 529 (1999)
6. O. Cozar, I. Ardelean, Gh. Ilonca, *Mater. Chem.* 7, 755 (1982)
7. J.E. Garbarczyk, M. Wasiucioneck, P. Jozwiak, L. Tykarski, J.L. Nowinski, *Solid State Ionics* 154-155, 367 (2002)
8. D.A. Magdas, O. Cozar, V. Chis, I. Ardelean, N. Vedeanu, *Vibrational Spectroscopy* 48, 251 (2008)
9. O. Cozar, D.A. Magdas, L. Nasdala, I. Ardelean, G. Damian, *J. Non-Cryst. Solids* 352, 3121 (2006)
10. N. Vedeanu, O. Cozar, I. Ardelean, S. Filip, *J. Optoelectron. Adv. Mater.* 8/3, 1135 (2006)
11. J. E. Canale, R. D. Condrate, J. K. Nassau, B. C. Cornilsen, *J. Canad. Ceram. Soc.* 55, 50 (1986)
12. V. Dimitrov, Y. Dimitriev, A. Montenero, *J. Non-Cryst. Solids* 180, 51 (1994)
13. P. Lottici, A. Antonioli, C. Razzetti, A. Montenero, *The Physics of Non-cryst. Solids*, Ed. L. D. Pye et. al., Taylor and Francis, London, 1992
14. P. Lottici, I. Manzini, A. Antonioli, G. Gnappi, A. Montenero, *J. Non-Cryst. Solids* 159, 173 (1993)
15. V. R. Kumar, R.P.S. Chakradhar, A. Murali, N.O. Gopal, J.L. Rao, *Int. J. Modern Phys. B* 17, 3003 (2003)
16. R.V.S.S.N. Ravikumar, V. Rajagopal Reddy, A.V. Chandrasekhar, B.J. Reddy, Y.P. Reddy, P.S. Rao, *J. All. Com.* 337, 272 (2002)
17. I. Ardelean, O. Cozar, N. Vedeanu, D. Rusu, C. Andronache, *J. Mater. Sci: Mater. Electron* 18, 963 (2007)
18. N. Vedeanu, O. Cozar, I. Ardelean, *J. Optoelectron. Adv. Mater.* 9/3, 698 (2007)
19. D. Kivelson, S. K. Lee, *J. Chem. Phys.* 41/7, 1896 (1964)
20. A.A. Kharlamov, R.M. Almeida, J. Heo, *J. Non.-Cryst. Solids* 202, 233 (1996)
21. J.E. Pemberton, L. Latifzadeh, J. Fletcher, S.H. Risbud, *Chem. Mater.* 3, 195 (1991)
22. J.E. Garbarczyk, P. Machowski, M. wasiucioneck, L. Tykarski, R. Bacewicz, A. Aleksiejuk, *Sol. State Ionics* 136, 1077 (2000)
23. M.A. Karakassides, A. Saranti, I. Koutselas, *J. Non-Cryst. Solids* 347, 69 (2004)
24. J. Koo, B.S. Bae, H.K. Na, *J. Non-Cryst. Solids* 212, 173 (1997)
25. I. Ardelean, S. Cora, V. Ioncu, *J. Optoelectron. Adv. Mater.* 8/5, 1843 (2006)
26. I. Ardelean, S. Cora, *J. Optoelectron. Adv. Mater.* 12/2, 239 (2010)

OBSERVATION OF THE EFFECTS OF UV EXPOSURE OF SOME SAMPLES CONTAINING TACROLIMUS

LUCIANA UDRESCU¹, MIHAELA POP¹, VASILE BALC¹ AND
M. TODICA^{1,*}

ABSTRACT. The effect of UV exposure on the tacrolimus was observed by UV VIS and NMR spectroscopy. After few hours of moderate UV exposure, the absorption coefficient is modified. Modifications can be also observed on the relaxation of the transverse magnetization of the protons contained in the molecule of tacrolimus. The absorption property of tacrolimus was enhanced by addition of TiO₂.

Keywords: *tacrolimus, UV VIS spectroscopy, TiO₂*

Introduction

Some medical substances, especially those used in dermatology, are designed for direct application on the skin on thin layers, without any protection. In these circumstances the product is permanently submitted to the mechanical stress, the action of air or UV radiation, or other external aggressive factors^[1,2]. The long time action of these factors facilitates the degradation of the chemical bonds or the oxidation of the components of the pharmaceutical product. The interest for medical applications is to keep unaffected, as long as possible, the properties of the active medical substance and to protect the skin against the aggressive actions. Tacrolimus is one of the most efficient medical substance used for the treatment of atopic dermatitis^[3,4]. It is designed for direct application on the surface of the skin, and offer only a weak protection against UV radiation in the domain 291 nm. In many situation the UV absorption coefficient is enhanced by adding small quantities of inorganic compounds, like TiO₂, or ZnO₂, which are well tolerated by the biological tissues,^[5,6].

In our work we observed the behavior of this medical substance submitted to UV exposure during many hours, and the possibility to enhance the UV absorption property by addition of TiO₂. The investigations were done by UV VIS and NMR spectroscopy.

Experimental

For ours studies we used the commercial form of tacrolimuls, known under the appellation Protopic. Each gram of Protopic ointment contains either 0.1% or 0.03% (w/w) of tacrolimus in a base of mineral oil, paraffin, propylene carbonate, white

¹ "Babes-Bolyai" University, Faculty of Physics, M. Kogalniceanu No 1,400084 Cluj-Napoca, Romania

* e mail: mihai.todica@phys.ubbcluj.ro

petrolatum and white wax. We named these samples S1, and S2. These samples were analyzed in their original state and after UV irradiation. The UV irradiation was realized with VL 215 G lamp, at wavelength 254 nm and intensity 76 mW/cm². The absorption capacity of samples was increased by addition of TiO₂. The samples containing TiO₂ were obtained by mixing the tacrolimus and TiO₂ many hours. The samples were deposited on thin films on microscope glasses. The UV VIS investigation we used Jasco V-670 system with scan speed 200 nm/min, UV VIS bandwidth 2 nm, and NIR bandwidth 8 nm. The NMR measurements were realized with Bruker Minispec at 40 MHz. The relaxation of transverse magnetization was measured using Carr-Purcell sequence.

Results and discussions

Situated in the upper part of the visible spectrum, the UV radiations are characterized by high energy and high interaction with the electronic structure of the atoms contained in the complex biological molecules. A rough classification, often used in medicine, can be realized in function of wavelength and energy.

Abbreviation	Wavelength (nm)	Energy (eV)
UVA	400 – 315	3.10–3.94
NUV	400 – 300	3.10–4.13
UVB	315 – 280	3.94–4.43
MUV	300 – 200	4.13–6.20
UVC	280 – 100	4.43–12.4

When interact with the biological tissues they can have both benefit and undesired effects. So, moderate UVB exposure induces the production of vitamin D in the skin. This vitamin has regulatory roles in calcium metabolism, immunity, cell proliferation, insulin secretion, and blood pressure ^[7].

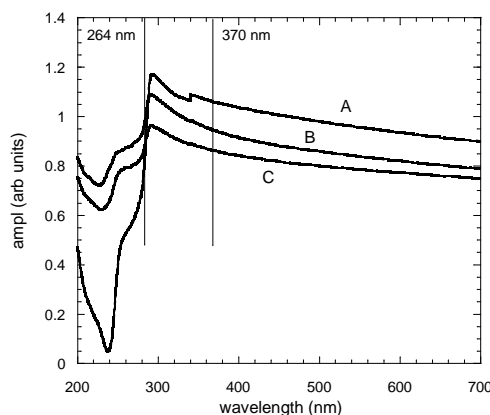


Fig. 1. The UV-VIS absorption spectra of sample S1 in initial state and after different time intervals of UV irradiation. A the sample in initial state; B after 2 hours irradiation; C after 4 hours irradiation

Exposure to UVB light, in particular, the 310 nm narrowband UVB range, is an effective long-term treatment for many skin conditions like psoriasis, vitiligo, eczema, and others^[8]. UVB phototherapy does not require additional medications or topical.

At high exposure, UVA, UVB, and UVC can damage the collagen fibers and, therefore, accelerate aging of the skin. Both UVA and UVB destroy vitamin A in skin, which may cause further damage^[9]. UVB light can cause direct DNA damage. The radiation excites DNA molecules in skin cells, causing aberrant covalent bonds to form between adjacent cytosine bases, producing a dimer. UVA does not damage DNA directly like UVB and UVC, but it can generate highly reactive chemical intermediates, such as hydroxyl and oxygen radicals, which in turn can damage DNA. These are some reasons that justify the interest for the study of the absorption properties of the product designed for the skin care. The absorption is determined by the transition between the electronic levels of the atom but the behavior under UV exposure depends on the nature of each substance. Solutions of transition metal ions absorb UV radiation because *d* electrons. Organic compounds, especially those with a high degree of conjugation, can absorb in UV or visible regions of the electromagnetic spectrum. Organic solvents may have significant UV absorption. Ethanol absorbs very weakly at most wavelengths. Solvent polarity and pH can affect the absorption spectrum of an organic compound. Tyrosine, for example, increases in absorption maxima and molar extinction coefficient when pH increases from 6 to 13 or when solvent polarity decreases.

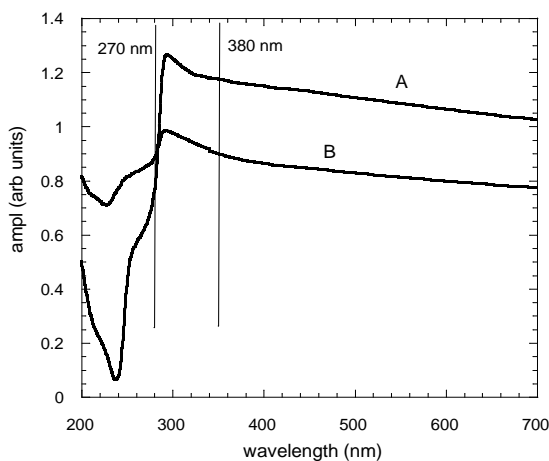


Fig. 2. The UV-VIS absorption spectra of sample S2: A after 4 hours UV irradiation; B in initial state

When light passes through the compound, energy from the light is used to promote an electron from a bonding or non-bonding orbital into one of the empty anti-bonding orbitals. In each possible case, an electron is excited from a full orbital into an empty anti-bonding orbital. Each jump takes energy from the light, and the jump is possible only if the quanta of light match the energy difference between the two

bonding state. The important jumps are: from π bonding orbitals to π anti-bonding orbitals; from non-bonding orbitals to π anti-bonding orbitals; from non-bonding orbitals to σ anti-bonding orbitals. Absorption in the region from 200 - 800 nm is possible only if the molecule contain either π bonds or atoms with non-bonding orbitals. In the ideal case of a single atom the transition take place for a well defined frequency, corresponding to the difference between the electronic levels, and the absorption spectrum is a delta function. For a system of molecules the absorption is observed over a whole range of wavelengths suggesting a whole range of energy jumps. This problem arises because rotations and vibrations in the molecule are continually changing the energies of the orbitals, and that, means that the gaps between them are continually changing as well. The result is that the absorption takes place over a range of wavelengths rather than at one fixed one. The spectrum is described by a distribution function, often Gaussian or Lorentzian, with a maximum corresponding to most probable transition. The area under the graph of the function is proportional with the concentration of absorbents. Quantitative description of the absorption is given by

the Beer-Lambert law: $A = \log_{10} \frac{I_0}{I} = \varepsilon \cdot L \cdot c$ where A is the measured absorbance,

I_0 is the intensity of the incident light at a given wavelength, I is the transmitted intensity, L the path length through the sample, and c the concentration of the absorbing species. For each species and wavelength, ε is a constant known as the molar absorptivity or extinction coefficient. This constant is a fundamental molecular property in a given solvent, at a particular temperature and pressure.

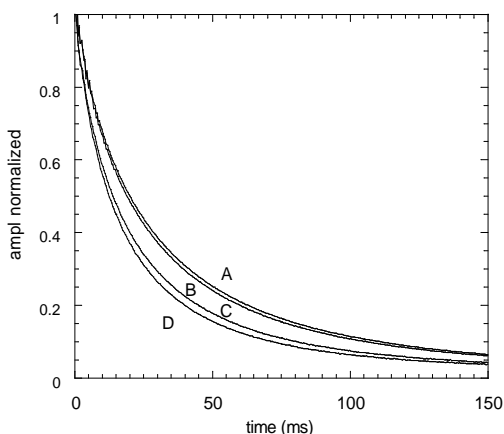


Fig. 3. The relaxation of transverse magnetization of the protons of tacrolimus in initial state and after different time interval of UV irradiation: A after 3 hours irradiation; B after 2 hours irradiation; C after 1 hour irradiation; D the sample in initial state;

The main effect of long time UV exposure, under normal conditions (1 atm pressure and room temperature), can be the destruction of some chemical bonds of the absorbent molecules. The diminution of the number of absorbent molecules results from the reduction of the area of the UV absorption spectra. This effect can be observed for our samples, (Fig.1). In the initial state, (non irradiated), the sample S1 is characterized by a large spectrum with an important absorption coefficient in the domain 264-370 nm. The width of the spectrum designates a large distribution of the energetic states of absorbent molecules, determined by rotation and vibration. A high absorption peak at 293 nm is observed and the spectrum is characterized by a large area. After a few hours of UV exposure, the amplitude of the peak diminishes, as well as the area under the graph. This behavior can be correlated with a reduction of the number of absorbent molecules. We suppose that a large number of molecules are subject to chemical degradation, (possible oxidation), after long time UV irradiation. This effect is more evident when the time of exposure increases, i. e. after 4 hours exposure. Similar behavior was observed for the sample S2, (Fig. 2). For this sample the shape of the absorption spectrum is very similar to that of sample S1. Only a weak broadening of the spectrum is observed from 270 to 380 nm, but the maximum of the absorption remains at the same wavelength, 293 nm. This similitude of the spectra is not surprising because both the samples contain the same compounds; only the concentration of tacrolimus is different.

In order to observe possible modifications of the behavior on a molecular scale we performed NMR relaxation measurements. The relaxation of transverse magnetization of the protons is determined by the dipolar interaction between the nuclear spins. This interaction is strongly influenced by the dynamics of the protons as well as by the modification of the chemical bond involving these atoms. High mobility of the nuclear spins reduces dramatically the dipolar interaction, having as an effect a long spin-spin relaxation time. This situation is characteristic for liquids or other systems with small molecules and high molecular dynamics. For systems with low spin dynamics, the dipolar interaction is strong, the local magnetic field felt by every nuclear spin differs from one spin to another, the precession frequency is very different from one spin to another one, having as a result a rapid phase loss of Larmor frequencies of nuclear spins. The result is a shortening of the spin-spin relaxation time. This behavior is characteristic for solids or systems with low molecular mobility. Modification of the relaxation time is associated with the modification of molecular dynamics. This effect can be observed for our samples. In the initial state, (before UV irradiation), the relaxation of transverse magnetization is characterized by a given time. After UV exposure the relaxation is longer, like for liquids, (Fig. 3). This fact indicates an increasing of local mobility of molecules. We can correlate this behavior with the destruction of some molecular bonds caused by UV exposure.

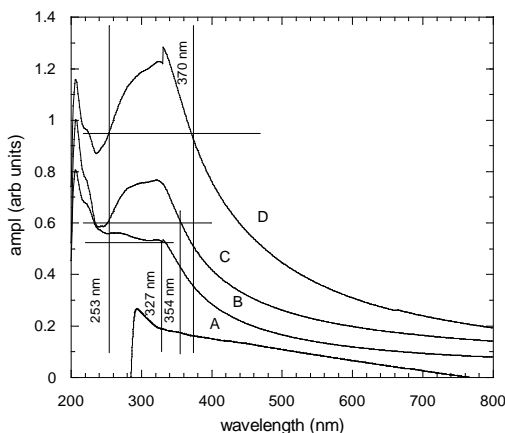


Fig. 4. The UV-VIS absorption spectra of samples: the tacrolimus in initial state (curve A), the tacrolimus with 3% of TiO_2 (curve B), the tacrolimus with 5% of TiO_2 (curve C) and the tacrolimus with 10% of TiO_2 (curve D)

Enhancement of the protection against UV radiation is one of the requirements imposed frequently to the products designed for skin care. Usually this effect is obtained by addition of different inert compounds to the pharmaceutical product. TiO_2 is known as one of the substances characterized by very good absorbance in the UV domain and also for its compatibility with biological tissues^[10]. One of the aims of our study was the observation of the behavior of tacrolimus after addition of TiO_2 . These observations were done by UV absorption. Addition of TiO_2 modifies the absorbance in the domain 250-350 nm (Fig. 4)^[11]. At 3% TiO_2 we can observe a well defined plateau of the absorption spectrum, between 253 and 327 nm. The absorption decreases after 350 nm but it remains greater than the absorption of the sample without TiO_2 . This behavior is most pronounced when the concentration of TiO_2 increases. At 5% we can observe a small broadening of the absorption domain, from 253 to 354 nm with a maximum at 325 nm. At 10% the width of the spectrum is 253 to 370 nm with a maximum at 330 nm. The increase of the absorbance in the domain 250-370 nm clearly demonstrates the effect of TiO_2 on the absorption properties. However the similitude with the spectrum of tacrolimus indicates no molecular induced by TiO_2 .

Conclusions

The effect of moderate UV exposure on the properties of tacrolimus was observed by UV spectroscopy. The absorption property of tacrolimus diminishes after UV exposure. This effect indicates a reduction of concentration of absorbent molecules. Modifications of the physical properties of samples after UV exposure

are revealed also by NMR measurements. The relaxation of transverse magnetization is longer for samples exposed many hours to UV radiation, indicating an increase of local molecular mobility. This effect can be associated with the destruction of some chemical bonds of some tacrolimus molecules. The absorption property can be modified by inclusion of TiO₂ in the sample. No chemical interaction between tacrolimus and TiO₂ is observed, but the UV absorption property of the system is enhanced.

REFERENCES

1. Clegg D W, Collyer A A *Irradiation effects on polymers* 1991 Springer 79-157.
2. Hane K, Fujioka M, Namiki Y, Kitagawa T, Kihara N, Shimatani K, Yasuda T 1992 *Iyakuhin Kenkyu* **23** 33-43.
3. Russell J J 2002 *American Family Physician* **15**.
4. Pascual C, Fleischer A B 2004 *Skin Therapy Letter* **9**.
5. Ruixia Hou, Leigang Wu, Jin Wang, Nan Huang 2010 *Applied Surface Science* **256** 5000-5005.
6. Thilo Gambichler, Nordwig S Tomi, Georg Moussa, Julia Huyn, Heinrich Dickel, Peter Altmeyer, Alexander Kreuter 2006 *Journal of the American Academy of Dermatology* **55** 5 882-885.
7. Jane Higdon 2004 Linus Pauling Institute, Oregon State University.
8. Dawe R S et al 2003 *British Journal of Dermatology* (London: British Association of Dermatologists) **148** (6): 1194-1204.
9. Torma H, Berne B, Vahlquist A 1988 *Acta Derm. Venereol.* **68** (4): 291-299.
10. Rie Yanagisawa, Hirohisa Takano, Ken-ichiro Inoue, Eiko Koike, Tomoko Kamachi, Kaori Sadakane, Takamichi Ichinose 2009 *Experimental Biology and Medicine* **234** 314-322.
11. ing Zhang, Meijun Li, Zhaochi Feng, Jun Chen, Can Li 2006 *J. Phys. Chem. B* **110** 927-935.

AFM INVESTIGATION OF $\text{SiO}_2\text{-ZnO-P}_2\text{O}_5$ THIN FILMS

R. VERES^{1,2}, M. TĂMĂȘAN¹, C. CIUCE², V. SIMON¹

ABSTRACT. $\text{SiO}_2\text{-ZnO-P}_2\text{O}_5$ thin films were obtained by spin-coating of a sol-gel bioglass precursor. The Si:Zn:P ratio of 4:1:8 in the sol-gel precursor is related to a bioglass composition which has not been investigated before. Considering that the topography and morphology of the surfaces are of primary interest in the applications of biomaterials, structural and surface properties of the prepared films were investigated using the Atomic Force Microscopy (AFM), as well as thermal and X-ray Diffraction (XRD) analyses. XRD results showed that the film sample have a prevalent amorphous character. AFM analysis indicated a rough, inhomogeneous surface of the prepared films.

Keywords: *biomaterials; sol-gel; thin film; AFM, XRD, TGA/DTA.*

1. Introduction

Since the discovery of bioglass by Hench et al. [1] in the early 1970s, various types of glasses, ceramics and glass-ceramics have been proposed and used mainly as bone replacement biomaterials [2-4]. Specifically, these biomaterials have found clinical applications as coating for prostheses, bone filler, vertebral substitution and, in a porous form, they are considered for tissue regeneration [5-9]. Different bioactive glasses and glass-ceramics have been synthesized in order to get desired properties conferred by required microstructure. The properties that are of interest in the characterization of biomaterial surfaces include the chemical composition, the hydrophilicity or hydrophobicity, the presence of ionic groups, the morphology (i.e. the domain structure), and the topography (i.e. the surface roughness, planarity, and feature dimensions) [10-13]. Common components used for synthesis of 45S5 and S53P4 registered bioglasses are Na_2O , CaO , P_2O_5 , SiO_2 . In addition to these are often added K_2O , MgO , B_2O_3 . There are some other glasses and glass-ceramics which also include ZnO , Ag_2O and Al_2O_3 [14]. According to our best knowledge, the $\text{SiO}_2\text{-ZnO-P}_2\text{O}_5$ system was not studied as far.

The atomic force microscopy (AFM) allows exploring the topography for almost any type of surface including metals, polymers, glasses, ceramics, composites, thin films, synthetic and biological membranes. Different analyzing modes are available

¹ Babeș-Bolyai University, Faculty of Physics & Institute of Interdisciplinary Research in Bio-Nano-Sciences, 400084 Cluj-Napoca, Romania

² Iuliu Hatieganu University of Medicine and Pharmacy, Faculty of Medicine, 400012 Cluj-Napoca, Romania

when using the AFM. The most common techniques are: contact mode, non-contact mode and tapping mode. When the AFM works in tapping mode, phase imaging is enabled simply by displaying a second image. Phase Imaging is a powerful extension of Tapping Mode AFM that provides nanometer-scale information about surface structure often not revealed by other scanning probe microscopy techniques [15]. Phase Imaging can also act as a real-time contrast enhancement technique. Because phase imaging highlights edges and is not affected by large-scale height differences, it provides for clearer observation of fine features, such as grain edges, which can be obscured by rough topography. Phase imaging is a tool for mapping variations in sample properties at very high resolution. This allows determining whether the surface is homogeneous. Also, AFM tapping-mode allows grain analysis - is meant to analyze sample of a flat horizontal surface with locally positioned particles or pores type. This mode involves a secant plane $Z=\text{const}$, drawn in parallel and at a fixed distance to the base plane ($Z=0$). Each object on the surface, crossed by this secant plane, with the section in the form of a simply connected domain is interpreted as a separate grain. The main geometric parameters are found and calculated for each separate grain.

The aim of this paper was to obtain thin films by spin-coating of a sol-gel with new bioglass composition, and to characterize the film structure and surface using primary AFM, as well as TGA/DTA and XRD techniques.

2. Experimental

The new 44.5SiO₂-11ZnO-44.5P₂O₅ (mol %) bioglass system was prepared following the sol-gel route. The precursors used were TEOS (Si(OC₂H₅)₄), zinc nitrate hexahydrate (Zn(NO₃)₂·6H₂O) and dibasic ammonium phosphate ((NH₄)₂HPO₄). The catalyst used was HNO₃. All the precursors were stirred separately with distilled water for 1/2 h. Then both solutions were added to TEOS solution under continuous stirring. Solution was left overnight for gelation at the room temperature.

A part of the gel was used to obtain thin films (a volume of 125 μl /layer) with a Single Wafer Spin Processor (WS-400B-6NPP/LITE) on a quartz substrate and it was rotate at 1500 rot/min. Other part of gel was dried for 24 hr at 100° C. Differential thermal analysis (DTA) and thermogravimetric analysis (TGA) were performed on Shimadzu type derivatograph DTG-GOH with a heating rates of 5°C/min using alumina open crucibles, in order to investigate the thermal behavior of the dried sample. The structure of the thin films and the dried sample were examined using a X-ray Shimadzu XRD 6000 with a Ni – filter, using CuK_α radiation (λ = 1.5418Å). The operation voltage and current were 40 kV and 30 mA. The measurements were performed at a scan speed of 1°/min in a 2θ scan range from 10° to 80°.

The average crystallite size was estimated based on the Scherrer equation:

$$D = \frac{k\lambda}{\beta \cos \theta}$$

where D is the crystallite size of the synthesized sample, in \AA , λ of 1.5418 \AA is the wavelength of $\text{CuK}\alpha$, k is the shape factor equal to 0.9, θ – is the diffraction angle, $\beta = \sqrt{B^2 - b^2}$, B – is defined as the full width at half maximum intensity and b is the resolution function of the diffractometer (in our case 0.12 calculated for the quartz calibration sample).

Topographic study of thin films for $\text{SiO}_2\text{-ZnO-P}_2\text{O}_5$ system obtained by spin-coating technique was performed with an NT-MDT Ntegra Vita atomic force microscope in tapping-mode at a line scanning frequency of 0.59 Hz. Bidimensional topographic images with $15\mu\text{m} \times 15\mu\text{m}$ area were obtained and these images were three-dimensionally analysed with a resolution of 256 pixels.

3. Results and discussion

The surface of the film obtained by spin-coating technique looked to be homogeneous and smooth. The TGA/DTA curves of 100°C dried sample are shown in Fig. 1. The TGA curve presents four regions of weight loss. The first weight loss occurs in the range of $35\text{-}123^\circ\text{C}$ (17.03%) and coincides with an endothermic peak in DTA that can be associated with the remove of free water molecules. The range of $123\text{-}203^\circ$ where the weight loss is about 11% presents two endothermic peaks and it can be related to the remove of water molecules physically adsorbed onto sample surface. A third weight loss (33%) can be observed in the range of $203\text{-}297^\circ\text{C}$ with a large corresponding endothermic peak in the DTA curve. This loss can be associated with the elimination of water caged in the pores. In the fourth range ($330\text{-}500^\circ\text{C}$) it is a small weight loss (3%) and the DTA signal is diminished constantly than can correspond to the elimination of the nitrates from precursors.

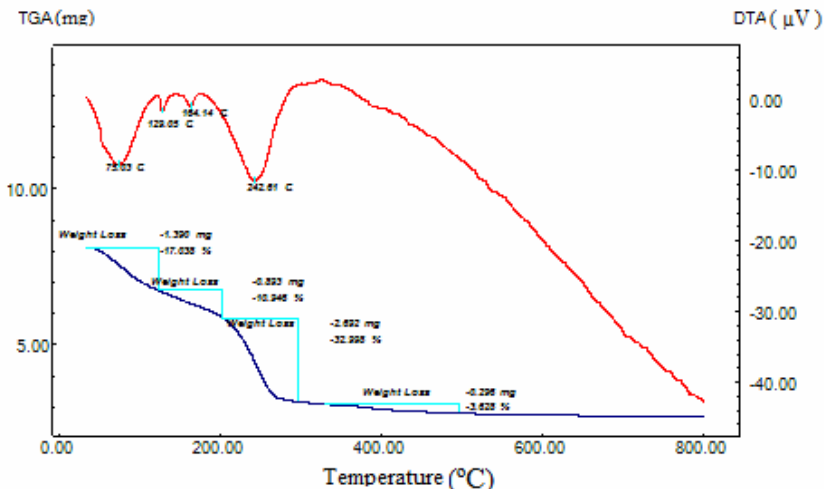


Fig. 1. DTA and TGA runs of so-gel derived $\text{SiO}_2\text{-ZnO-P}_2\text{O}_5$ bioglass.

The XRD patterns of the thin film and 100 °C dried bioglass sample are illustrated in Fig.2. The thin film XRD pattern shows a good agreement with the treated sample pattern (Bragg angle, 2θ of the peaks are similar for the two patterns with a little difference in intensity). A prevalent amorphous state of both samples can be observed. Beside the large diffraction peak that dominates the XRD pattern, there are peaks recorded at $2\theta = 16, 18, 22.5, 29, 31, 32, 37.5$ and 40° indicating the presence of a minor crystalline structure, that could be assigned primary to residual nitrate or phosphate crystals [16, 17]. On the other hand, it is to mention that crystallites of $ZnSiO_3$, Zn_2SiO_4 and $Zn_2P_2O_7$ type have not to be completely excluded, because they could contribute to reflections very close to the same diffraction angles [18-21]. Using the Scherrer equation, the crystallites size was estimated at 32.65 nm.

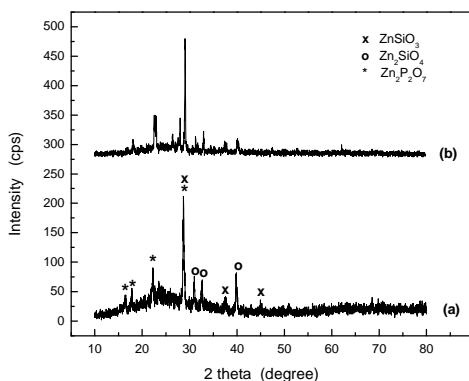


Fig. 2. XRD pattern of SiO_2 - ZnO - P_2O_5 thin film (a) and 100°C dried sol-gel sample (b).

Surface morphology is well revealed in AFM images. The two-dimensional (2D) and three-dimensional (3D) views of the surface morphology of thin film (scale of $15\mu m \times 15\mu m$) are shown in Fig.3a and Fig.4. Their analysis denotes a rough surface that is preferred for the attachment of bio-molecules [22].

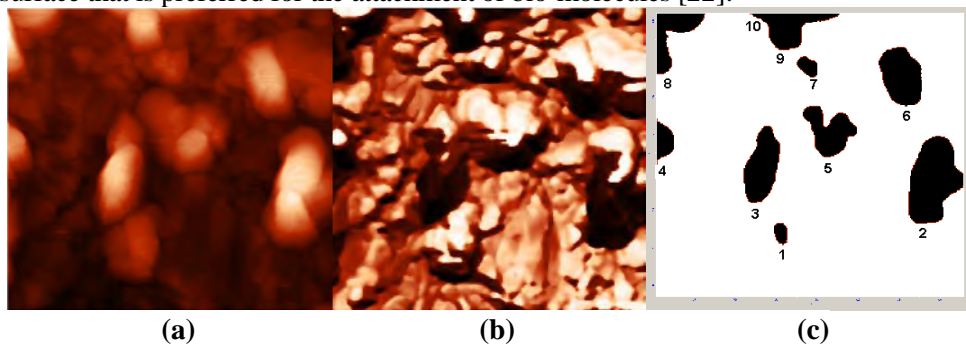


Fig. 3. AFM tapping mode 2D-image (a), phase image (b), and the corresponding grains collected (c) of thin film sample.

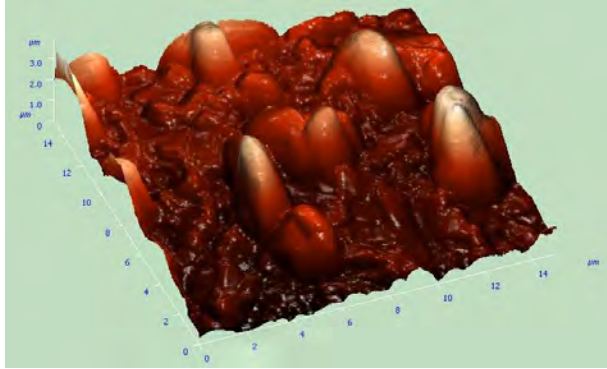


Fig. 4. AFM tapping mode 3D-image.

AFM tapping mode allows displaying also the phase image (Fig. 3b) and graining identification (Fig. 3c). Due to its very high resolution, the phase image permits to observe fine variations in sample properties. Combining the 2D image with the phase image, it can be evidenced the features of similar chemical composition. For the identification of the grains, in the 2D image (Fig. 3a) each roughness on the surface is crossed by a secant plane, with the section in the form of a simply connected domain and is interpreted as a separate entity (Fig. 3c). The main geometric parameters are calculated for each separate roughness.

Some characteristics of the grains were obtained using the software of the atomic force microscope. The parameters including the grain area, equal to the section area, the grain volume and maximal size, the maximal and average heights, the perimeter, along with major geometric characteristics for each grain are summarized in Table 1, where each line corresponds to a certain roughness with the values of its geometric parameters. The first column indicates the grain numbers, and each subsequent column corresponds to certain parameters. The average value of the parameters is given in the first line, and in the second line there are given their standard deviations, SD. The standard deviations were fairly large for half of the evaluated grains. Fig. 5 shows the histogram of the grain area distribution density. The area of half of the gains is between 3 and $4.5 \mu\text{m}^2$.

Table 1.

The parameters of the grains depicted in Fig. 3c.

	Area, μm^2	Volume μm^3	Z Range, μm	Max Z, μm	Mean Z, μm	Perimetr μm	Diameter μm	Length, μm	Mean width, μm	X Size, μm	Y Size, μm
Mean	3.253	7.056	0.787	2.458	2.023	8.176	1.824	3.176	0.824	1.882	2.471
SD	2.502	0.011	0.548	2.042	2.102	4.412	0.882	1.588	0.412	1.176	1.294
1	0.578	0.986	0.073	1.744	1.707	3.118	0.882	1.294	0.471	0.647	1.118
2	8.630	20.35	1.468	3.139	2.359	13.64	3.294	5.353	1.588	2.706	4.647
3	4.792	10.56	1.162	2.833	2.205	11.05	2.471	4.412	1.059	1.765	4.059

4	1.408	2.957	0.785	2.456	2.100	5.471	1.353	2.706	0.529	0.882	2.529
5	4.000	7.541	0.567	2.237	1.885	11.11	2.235	3.765	1.059	2.647	2.706
6	4.917	10.55	0.883	2.554	2.147	9.647	2.529	3.765	1.294	2.118	3.118
7	0.754	1.309	0.136	1.806	1.735	3.647	1.000	1.471	0.529	1.000	1.118
8	3.516	7.650	1.671	3.342	2.176	11.64	2.118	4.059	0.882	2.412	3.235
9	3.945	8.630	1.072	2.743	2.188	12.29	2.235	4.765	0.824	4.353	1.941
10	0.003	0.006	0.054	1.725	1.725	0.059	0.059	0.059	0.059	0.059	0.059

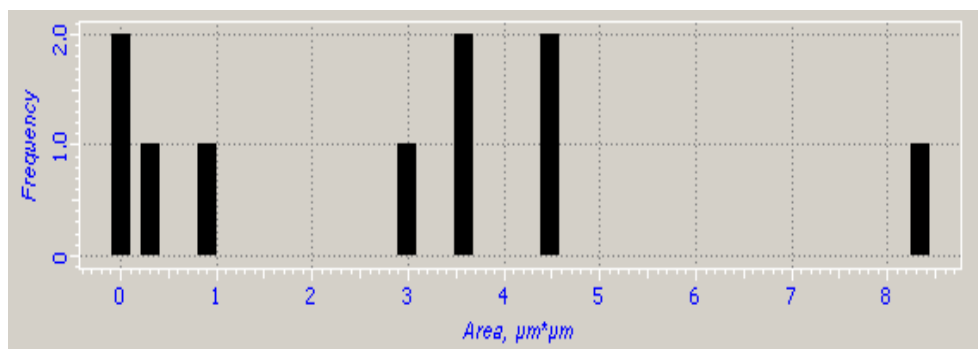


Fig. 5. Histogram of the scanned area.

4. Conclusions

Thin films were obtained by spin-coating technique of the sol-gel new bioglass composition 44.5SiO₂-11ZnO-44.5P₂O₅ (mol %). Both in film and 100°C dried bioglass, the XRD results indicate an amorphous phase and nanometric crystals of residual synthesis reagents and/or of new zinc silicate and phosphate formed during sample synthesis. The large mass loss recorded in 203-297 °C temperature range from the dried bioglass sample is related to removal of water molecules retained in cavities, which suggest certain porosity, also expected for film samples. AFM analysis of the thin films points out a rough, inhomogeneous surface with roughness heights around 3 μm and areas up to 8.63 μm^2 , convenient for the biomolecules attachment.

Acknowledgements

R.V. author wishes to thank for the financial support provided from programs co-financed by The Sectoral Operational Programme Human Resources Development, Contract POSDRU 88/1.5/S/56949 – „Doctoral and postdoctoral programs to support research”.

REFERENCES

1. L. L. Hench, R. J. Splinter, W. C. Allen, T. K. Greenlee, *J. Biomed. Mater. Res.* 2 (1971) 117.
2. H. Oonishi, L. L. Hench, J. Wilson, F. Sugihara, E. Tsuji, M. Matsuura, S. Kin, T. Yamamuro, S. Mizokawa, *J. Biomed. Mater. Res.* 51 (2000) 37.
3. P. Ducheyne, J. M. Cuckler, *Rev. Clin. Ortho. Rel. Res.* 277 (1992) 102.
4. M. Vallet-Regi, *J. Chem. Soc. Dalton Trans.* 5 (2001) 97.
5. E. Verne, M. Bosetti, C. Vitale-Brovarone, C. Moiescu, F. Lupo, S. Spriano, M. Cannas, *Biomaterials* 23 (2002) 3395.
6. E. Verne, R. Defilippi, G. Carl, C. Vitale-Brovarone, P. Appendino, *J. Eur. Cer. Soc.* 23 (2003) 675.
7. C. Vitale-Brovarone, S. Di Nunzio, O. Bretcanu, E. Verne, *J. Mat. Sci. Mater. Med.* 15(2004) 209.
8. E. Verne, F. Valles, C. Vitale-Brovarone, S. Spriano, C. Moiescu, *J. Eur. Cer. Soc.* 24 (2004) 2699.
9. C. Vitale-Brovarone, E. Verne, *J. Mat. Sci. Mat. Med.* 16 (2005) 863.
10. J. E. Gough, J. R. Jones, L. L. Hench, *Biomaterials* 25 (2004) 2039.
11. I. Jun, Y. Koh, H. Kim, *J. Am. Cer. Soc.* 89 (2006) 391.
12. M. M. Pereira, J. R. Jones, L. L. Hench, *Adv. Appl. Ceram.* 104 (2004) 35.
13. J. D. Andrade (Ed.), *Surface and Interfacial Aspects of Biomedical Polymers I: Surface Chemistry And Physics*. Plenum Press, New York (1985).
14. T. Cunningham, F. M. Serry, L. M. Ge, D. Gotthard, D. J. Dawson, *Surf. Eng.* 16, 295 (2000).
15. D. Klee And H. Hocker, *Advances In Polymer Science* 149, 1 (2000).
16. A. Ferrari, A. Braibanti, A.M.M. Lanfredi, A.Tiripicchio, *Acta Crystallogr.*, 22 (1967) 240.
17. A.A. Khan, J.P. Roux, W.J. James, *Acta Crystallogr. B*, 28 (1972) 2065.
18. R.T. Downs, The RRUFF Project: an integrated study of the chemistry, crystallography, Raman and infrared spectroscopy of minerals, Program and Abstract of the 19th General Meeting of the International Mineralogical Association in Kobe, Japan. O 03-13, 2006.
19. N. Morimoto, Y. Nakajima, Y. Syono, S. Akimoto, Y. Matsui, *Acta Crystallogr. B* 31 (1975) 1041.
20. M.A. Simonov, P.A. Sandomirskii, Yu.K. Egorov-Tismenko, N.V. Belov, *Dokl. Akad. Nauk*, 237 (1977) 581.
21. T. Bataille, P. Benard-Rocherulle, D. Louer, *J. Solid State Chem.*, 140 (1998) 62.
22. B.J. Larson, J.M. Helgren, S.O. Manolache, A.Y. Lau, M.G. Lagally, F.S. Denes, *Biosens. Bioelectron.* 21 (2005) 796.

BOOK REVIEW

Roman Baican, Renewable energies, Grinta, Cluj-Napoca, 2010, ISBN 978-973-126-191-1

Nowadays, the humanity finds itself in a crucial evolution stage regarding the energy consumption, environmental protection and possible changes of the global climate. Although the use of fossil energy leads to a huge amount of greenhouse gases and other nocive particles and gases and the proved reservs are limited, they continue to be used at large scales as the forecasts indicate. In order to overcome these problems the humanity should turn its attention on the renewable energy resources. Renewable energy is the energy that comes from natural resources such as sunlight, wind, rain, tides, geothermal heat, and, biomass, which are renewable, naturally replenished.

Renewable energies is the title of the book that author is dr. Roman Baican. He studied physics at the Faculty of Physics of the Babes-Bolyai University in Cluj-Napoca, Romania, and received his PhD degree in 1973 from the same university. After 10 years of academic career in Cluj-Napoca he continued his activity as a researcher at the Institute of Atomic Physics in Bucharest. In 1974 he obtained the Price *C. Miculescu* of the Romanian Academy. From 1982 he worked in Germany, at the J. M. von Goethe University of Frankfurt/Main, Standard Elektrik Lorentz and Adam Opel AG. In 2008 he became Honorary Professor of the Transilvania University of Brasov, Romania. He authored and co-authored over 80 peer-reviewed research papers, 10 patents and 6 books.

The present book consists of 14 chapters. The first one presents the state of the art of the renewable energies all around the world. The next chapters provide basic information about sun, the main energy resource for other renewable energies, and the solar energy that is directly employed for electricity production or heating.

The wind energy is the subject of another chapter. There are given basic information about wind and the wind speed distribution, the physics of wind energy, and details about wind turbines and wind farms used for electricity generation.

The water energy, including marine energy (tides, waves, salinity or osmotic power), hydropower and geothermal energy, is described in the next chapter. Plenty of details about thermal energy pumps and how plants based on osmosis work are also given.

Biomass and biofuels, including BtL (Biomass to Liquid), bioethanol, biogas and biofuels derived from vegetable oils, are discussed in the next five chapters. Information about the technical procedure of biofuels obtaining from different raw materials and, the corresponding advantages and disadvantages, are also provided. Finally, the fuel cells and the hydrogen energy as the energy sources with zero pollution are discussed.

Although the nuclear energy is not a renewable energy it is also presented in a separate chapter because it is widely used around the world and is less pollutant as compared to the fossil energy.

The book ends with a chapter revealing recent general data regarding the energy: consumption, reserves, consequences and alternatives. It also provides information about the Kyoto protocol and the available mechanisms of fighting against global warming. The book addresses to the students, engineers and all the peoples, who are energy consumers and care about global warming and the future of our planet.

MONICA BAI

*Associate Professor, Babes-Bolyai University,
Faculty of Physics, Molecular Spectroscopy Dept.,
M. Kogalniceanu 1, 400084 Cluj-Napoca, Romania*